Landslide stability analysis using UAV remote sensing and in situ observations

A case study for the Charonnier Landslide, Haute Alps in France

Job de Vries (5600944)
Utrecht University

Under supervision from:
Prof. dr. S.M. de Jong
Dr. R. van Beek

May – 2016
Utrecht, the Netherlands

Utrecht University

Abstract

An approach consisting of different methods is applied to determine the geometry, relevant processes and failure mechanism that resulted in the failure of the Charonnier landslide in 1994. Due to their hazardous nature landslides have been a relevant research topic for decades. Despite that individual landslide events are not as hazardous or catastrophic as for example earthquakes, floods or volcanic eruptions, they occur more frequent and are more widespread (Varnes, 1984). Also in the geological formations of the Terres Noires, in south-east France, it is not necessarily the magnitude of events, rather their frequency of occurrence that makes mass movements hazardous. An extremely wet period, between September 1993 and January 1994, caused a hillslope in the Haute-Alps district to fail. Highly susceptible Terres Noires deposit near Charonnier River failed into a rotational landslide, moving an estimated 107,000 m^3 material downslope. Precipitation figures between 1985 and 2015 show a clear pattern of intense rainstorms and huge amounts of precipitation in antecedent rainfall. This suggests that the extreme event on January 6 with 65 mm of rain after the wet months of September, October and December caused the sliding surface to fail. A total of 36 soil samples and 22 saturated conductivity measurements show a decreasing permeability with depth and the presence of macro-pores in the topsoil, supplying lateral flow in extreme rainfall events and infiltration with antecedent rainfall periods.

Conventional remote sensing observations (e.g. satellite or Aerial), with centimeter resolution, over this relatively vegetated landslide remain challenging due to its relative small size. Therefore, an UAV platform with a compact camera was used to capture the current elevation, structure and geomorphological characteristics at the Charonnier landslide with a 6-centimeter resolution elevation model. Multi View workflow and the Structure from Motion process were used to derive a digital surface model from images, with an accuracy of 10 cm in the vertical direction and 8 cm in the horizontal. Making it an easy and affordable to use remote sensing approach with accuracy and resolution comparable to other remote sensing approaches. The results gave insight in the current stability of the Charonnier landslide and can in the future be used to assess its dynamics. Vegetation remains a challenge for many remote sensing techniques, by excluding vegetation points from the texture generation phase in Agisoft a representation of the terrain was created, used to estimate the rupture surface. Due to bias in the control points the overall model quality couldn't be fully assessed, but the results suggest that the tested approach can be an alternative to for example LIDAR techniques.

A total of 29 shear strength tests were performed to capture the materials' in situ shear strength properties. A friction angle of 30.2° and 33.1 combined with an effective cohesion of 7.6 and 6.0 kPa for parent for parent and slump material respectively suggest that slump material has higher shear strength. Combining all these observations with the best estimate rupture surface, the slip4ex analytical model allowed the assessment of the stability and rupture surface, suggesting a current stable situation at the Charonnier landslide. Using one homogeneous layer and a water table depending on the monthly precipitation it was possible to derive the critical water depth at the estimated location of the sliding surface. Precipitation events with higher return periods than recorded in the past 30 years would be required to reactivate the landslide in its current shape because of a rising groundwater table. Creep and erosion by the Charonnier River are altering the slope stability at an unknown rate as we speak, suggesting that the stability will change in the near future. All together the use of UAV remote sensing combined with more conventional research methods allowed for the complex stability analysis of the Charonnier landslide in relation to precipitation and sub-surface hydrology.

* Cover image: Charonnier landslide on the third of June 2017, aerial photograph taken by Henk Markies.

Acknowledgements

Starting with the thesis I aimed to combine several research techniques that were central during my Bachelor Earth and Economics at the Vrije University and Master Earth Surface and Water at Utrecht University. The combination of fieldwork, shear testing in the lab, remote sensing with drones, image processing and putting it all together in 2D stability analysis made it the most complete experience for me so far. This would have not been possible without the enthusiasm of Prof. Dr. Steven de Jong and the patience of explaining all my questions from Dr. Rens van Beek. However, I would especially like to thank the technical staff from Utrecht University for their support, especially Henk Markies for flying during the field campaign.

Table of contents

Abbreviation

DEM	Digital Elevation Model
DGPS	Differential GPS
DSM	Digital Surface Model
DTM	Digital Terrain Model
GCP	Ground Control Point
GPS	Global positioning system
LIDAR	Light Detection and Ranging
MVS	Multi-View Stereo Photogrammetry
SfM	Structure from Motion
SIFT	Scale Invariant Feature Transformations
SWRC	Soil water retention curve
TIN	Triangular Irregular Network
UAV	Unmanned Aerial Vehicle
UV	Ultra - violet

List of symbols

Notation	Factor	Unit
σ	Normal Stress	[N * m^{2}]
σ'	Effective stress	[N * m^{2}]
τ	Shear stress	[N * m^{2}]
τ_f	Shear stress at failure	[N * m^{2}]
F	Force	[N, kg*m^{-1}*s^{2}]
FoS	Factor of safety	[dimensionless]
ϵ	Strain	[dimensionless]
y	Shear strain	[N * m^{2}]
z_0	Original length	[mm]
c'	Effective Cohesion	[kN * m^{2}]
ϕ'	Angle of internal fraction	[°]
δh	deformation	[mm]
u	Pore pressure	[kN * m^{2}]
f	Infiltration capacity	[-]
f_c	Constant infiltration capacity	[-]
f_0	Infiltration capacity at time = 0	[-]
Q	Water flow	[m^{3}/s]
K	Hydraulic conductivity	[m^{-1} * d^{-1}]
A	Cross sectional area	[m^{2}]
$\Delta\Psi$	the matric potential (soil water potential)	[Pa]
ΔZ	Distance	[mm]
T	Recurrence time	[years]
i	Rank	[dimensionless]
p	Precipitation	[mm]
N	Yearly maximum rainfall event	[dimensionless]
r	Radius	[m]
h	Height water column	[cm]
V	Sample volume	[m^{3}]
M_s	Dry weight soil sample	[g]
w	Water content	[g * g^{-1}]
P_b	Dry Bulk density	[g * cm^{3}]
P_w	Density of water	[g * cm^{3}]
Θ_m	Gravimetric soil moisture content	[g *g^{-1}]
Θ_V	Volumetric water content	[dimensionless]
Por	Porosity	[dimensionless]
ɣ	Bulk unit weight	[kN * m^{3}]
N'	Effective normal stress	[N * m^{2}]
W	Weight of soil in slice	[kN]
L	Length slope	[m]
H_1	Upslope vertical water table	[m]
H_0	Downslope vertical water table	[m]
B	Slope angle	[°]

1. Introduction

Due to the hazardous and unpredictable nature of mass wasting processes, the need rose already in the 17th century, to fully understand their wide range of triggering factors, spatial- and temporal dynamics and potential solutions (Selby, 1993). Although the gravitational forces are primary drivers of mass movement, there exist a wide range of other factors that affect the stability of hillslopes. In general, one trigger initiates a mass movement after (sub) surface characteristics are altered, making the slope susceptible for failure (van Beek, 2003; van Beek & van Asch, 2003). This often results in complex mass movement with multiple indirect causes (Terlien, 1998).

Due to the diversity in causes and resulting movements, the risks of mass wasting vary significantly. In general, the mass wasting risk represent a threat in the range of minor disruptions to social and economic catastrophes and even the loss of life. An inverse and exponential relation between magnitude and frequency of occurrence exist, where large and catastrophic events happen less frequent. Globally the impact from landslides is estimated at a total of US$20 billion damage annually, estimated at 17% of the total of all natural hazards between 1980 and 2013 (Klose et al., 2016). Between 2004 and 2010, 2620 deadly landslide events where reported in a earth surface area covering 3.7 x 10^6 km^2, causing 32.322 fatalities (Haque et al., 2016). But the mass wasting hazard is not a uniform process in space and time; it fully depends on the amount of available energy and the resisting forces now, and in the future. Global or regional indications are therefore poor reflectors of the financial burdens and vulnerability to landslide hazards on a local scale (Klose et al., 2016).

Increasing tourism in mountainous areas, climate change and the ever-increasing demand for cultivated lands make it increasingly important to study (complex) mass wasting processes. Despite individual landslides not necessarily being more hazardous than other natural disasters, over multiple years or for large regions, they cause more (indirect) damage due to their frequency of occurrence (Varnes, 1984; Scaioni et al., 2014; Malamud et al., 2003). This is also the case for the Hautes Alps, a relative small mountainous province in the south east of France (6925 km2). Despite being relatively sparsely populated with 144.950 inhabitants (Insee, 2015) the high landslide frequency poses a risk for inhabitants, their infrastructure and agricultural activity. During the wet months between September 1993 and October 1994 several hillslopes failed, resulting in a wide range mass wasting processes (Pech & Sevestere, 1994); again stressing the relevance of the hazard in the area. In nearby catchments for example, a significant number of landslides have been recorded since 1850. In the Barcelonnette basin (80km) 132 records and for the Vars basin (100km) a total of 377 mass wasting activities (Flageollet et al., 1999). Numerous landslide researches have already been conducted in the nearby area (e.g. Malet, et al., 2005; Antoine et al., 1995; Caris & Van Asch, 1991; Van Asch et al., 1996; Maquaire et al., 2003). This makes that the mass wasting processes in the area are understood very well: it is often related to the presence of Marl deposits from the Jura and early cretaceous time, its Mediterranean climate affected by steep slopes in the Alps and more recently by the influence from human activity (Descroix & Gautier, 2002).

After heavy rainfall over a long period between September and December 1993 in the Haute-Alps region of Southern France, another multiple day rain event in the first days of January 1994 caused several slopes to fail, one near the Charonnier River a tributary to the Drouzet River (Pech & Sevestre, 1994). On the 7th of January 1994 in the early morning, a body of mass moved downslope near the Charonnier River and the road that connects Veynes with Barcillonette and Tallard, making it a very accessible mass movement.

Due to the complexity of mass wasting processes, spatial- and their temporal coverage, the scales at which landslide research is conducted can cover a wide range of temporal and spatial resolutions (Scaioni et al., 2014). Classical small scale research often has a strong focus on a single mass wasting events or an instable slope, which is monitored for its stability over time (e.g. van Beek

& van Asch, 2003). They therefore require relative large resources and time to analyse the relevant characteristics at the best temporal resolution possible. Regional landslide assessments on the other hand, often have a focus on landslide susceptibility, hazard zonation for multiple landslides or (potential) instable slopes (Moine et al., 2009). Such research often has a focus on the spatial distribution in the area, not necessarily the circumstances that govern mass wasting (Scaioni et al., 2014). Landslide hazard maps often only indicate where landslides may or have occurred; thereby excluding the required triggers or thresholds under which slope failure may occur. But these triggering thresholds separate combinations of characteristics that cause landslides from those combinations that don't (Terlien, 1998). Statistical analyses are therefore often used to determine relations between these hillslope characteristics and their occurrence (Terlien, 1998). Other approaches that can be applied to mass wasting processes are models that can capture mass wasting process over time (Mallet et al., 2005).

Recent development in scientific research tools changed the way these mass movements have been studied in the Hautes-Alps, and the rest of the world. Especially the development of remote sensing tools resulted in a change of focus from classic analytical research to mass movement inventories (Mantovani et al., 1996). These inventories can give insight into locations, topology and geomorphological characteristics, state of activity and frequency of occurrence (Razak et al. 2011). Different sensors, attached to different platforms, are often used for the analyses in mass wasting processes and events: optical, thermal, microwave and laser remote sensing are common examples (Scaioni et al., 2014). One of the most recently introduced remote sensing platforms, which also has been applied in the field of mass wasting analysis, is the unmanned aerial vehicle (UAV) (Pajares, 2015; Lucieer, de Jong & Turner, 2013; Niethammer et al., 2012). The UAV allows the relative easy acquisition of high resolution and low-altitude spectral information. As opposed to many conventional remote sensing techniques the UAV can be equipped with, for example, an inexpensive and user friendly optical, digital camera. The well understood photogrammetry principle, in combination with image algorithms, then allows processing the resulting overlapping images in accurate representations of the terrain surface, such as a Digital Elevation Model (DEM) and Orthomosaic (Smith et al., 2015).

Besides the monitoring of mass wasting processes with remote sensing, understanding their behaviour trying to link spatial and temporal variations to the occurrence of mass wasting and ultimately predicting mass wasting hazard, has been a major research focus (van Beek & van Asch, 2003). The ability to forecast landslide occurrence with sufficient precision thus far remains limited to likelihood and probability indications on the local scale. Global and even regional studies often simply indicate the susceptibility, often based on the presence of previous landslide events (Crozier & Glade, 2005). Especially on the scale of single events, the need for high resolution and accurate data has therefore increased to capture the conditions that cause the slope to become unstable and the processes that triggered the movement. This extensive interest in mass wasting processes has resulted in a vast and knowledgeable research field that is able to determine risk areas and analyse individual mass movements. With this, a wide variety of research methods, classifications and approaches have been explored that help determine causes and relevant processes. For example, topographic surveys conducted with time-consuming and costly techniques, such as total stations, different types of laser scanners and satellite systems (Clapuyt et al., 2016). In this research, a combination between topographic survey with an UAV remote sensing platform, in situ observations and stability analysis is therefore proposed to analyse a mass movement in the Hautes Alps, to improve the reliability of the final stability results, and thus a step towards accurate hazard mapping of spatial- and temporal probabilities of individual landslides in the region.

This research aims to use the UAV as a remote sensing platform and combine the resulting digital surface model (DSM) and orthomosaic with more conventional research methods that capture the stability of the Charonnier landslide. Combining these methods, it is possible to understand complexity around the causes and triggering mechanism that ultimately resulted in the failure of the Charonnier landslide, without extensive time and financial resources at the researchers' disposal. The aim is to answer the following research questions in this report:

1. Can a high-resolution DSM and orthomosaic be constructed with the help of UAV remote sensing campaign for the Charonnier landslide?
2. What is the spatial accuracy (in x, y, and z direction) of derived surface model and orthomosaic compared to high resolution GPS measurements?
3. Can this representation of the surface (DSM), be used to model the (past and future) dynamics and estimate the volume displacement of the Charonnier landslide in the French Alps?
4. Can the failure plane of the landslide be reconstructed in a 2D model, from a combination of soils samples and UAV remote sensing observations?
5. Can measured slope stability factors for the Charonnier landslide, such as effective cohesion and internal fraction, be determined by direct shear testing?
6. Are daily precipitation observations and extreme event analysis sufficient to reconstruct the relevant physical soil processes that lead to the failure of the rupture surface of the Charonnier landslide?

To obtain the necessary in situ observations, a 3-week field trip was organized in June 2016 to collect UAV imagery and soil samples. It is expected that this research will contribute to the research in the UAV remote sensing possibilities for individual landslide monitoring. Especially the straight forward applicability, within a short timeframe, will support conventional research methods due to relative high resolution of the output. The integration between the remote sensing products and the in-situ observations should allow a more accurate stability analysis of Charonnier landslide, which has never been the subject of an extensive research before.

In chapter two the different types of mass movements will be discussed in relation to relevant causes and triggering mechanisms. Chapter three has a focus on the local environmental conditions near the landslide were as chapter four gives a detailed overview of the applied methods. The results are summarized in chapter five and discussed in chapter six. The conclusion in relation to the proposed research questions is in chapter seven.

2. Theoretical background mass movements

Mass movements are an expression of landscape adapting to a stable state. Affected by internal and external factors, the slope stability changes over time, resulting in a constantly changing stress distribution above a failure plane or slip surface (van Beek, 2003). The variation in the stability factors may be slow, such as weathering, or rapid due to, for example, seismic activity (Dikau, 1996). Landslide activity characterised as inactive, dormant, stabilized or relict and may also extend over long time periods because of uplift or over relative short timeframes as consequence of precipitation events. Therefore, it is insightful in any small-scale mass wasting research to distinguish type, parent material, activity and causes. Due to the diversity and complexity of controls on mass movement, a variety in shapes, behaviour, volume, and speed that are involved, exist (Dikau, 1996; Parise, 2003). It is therefore necessary to consider all these, and other relevant, characteristics that cause changes in the stability of the slope to fully understand the landslide hazard and related risk. Where the risk is the likelihood and related consequence for exposed assets if a slope fails and a hazard is the adverse physical process of a slope failure (Crozier & Glade, 2005).

2.1. Types of mass movement

In literature, different terms are used to describe the down- and outward movement of a mass down a hillslope. Although landslide is a popular term, this does not capture the range of slope movements that can be distinguished. Being focused on a landslide, this paper also acknowledges different types of relevant mass movements that can be distinguished, based on causes, movement- and material types. An overview is presented in this chapter, based on the EPOCH (1991 – 1993) project, as explained by Dikau (1996). The EPOCH project recognized several types of mass movement: falls, topples, rotational slides, translational slides, planar, lateral spreading, flow and complex movements, which consist of a combination of movement types (figure 2.1). Each type can also have distinctive variations in material type, recognisable features, slope stability, hydrology and vegetation. Each of these factors relevant for the Charonnier landslide will be discussed.

2.1.1 Fall

When a material, such as rocks, debris or soil particles, moves freely from a steep hillslope it is considered as a fall (Dikau, 1996). Although several types of materials can be involved, the initiation process is similar. A fall originates in material that was already (partially) segregated from the parent material or bedrock. This can be caused by triggering events, slow natural processes such as weathering, but often a combination of both. In both cases the segregation results in instable slopes, when the natural slope exceeds the balance limits. When the segregation leads to a free fall without interruption literature speaks of a primary fall (Dikau, 1996; Selby, 1993), any interruption with the surface makes it a secondary fall. The deformation, as result of the interruptions, involves break-up, bouncing, sliding and rolling on impact. The direction, speed, run out distance and other movement characteristics all depend on the orientation, shape and angle of the slope.

2.1.2 Topple

A mass of material tilting around a fixed pivot point on a slope is called toppling. This type of failure generally consists of a bulk of coherent material that got separated from the parent material on a slope, due to weathering, swelling and shrinking or other physical processes that result in joints or cracks in the material (Dikau, 1996). These separation processes result in the supporting base of the load to become narrower, ultimately resulting in a failure.

2.1.3 Rotational slide

For a rotational slide the shear surface of the sliding is curved concavely upward and the movement of the slide is parallel to the slope and outward across the slide. Another distinctive characteristic is the absence of internal deformation of the moving mass, due to the low movement speed (± 5 mm $* S^{-1}$) observed in the major movement phase (Dikau, 1996; Embleton & Thornes, 1979). Often, this dominant movement phase is followed by a creep movement, especially in the tow of the slide; again distortions of the material remain limited. The body of the landslide is exposed to shear stress; the head may show signs of cracking under tension stresses.

Lastly another subdivision can be made based on the amount of sliding units. When multiple mass units start moving along surface of the sliding, also called failure plane, the movement is a multiple rotational slide or a successive slide. When a common failure surface is intersected by two or more moving units the movement is considered a multiple slide. When a series of slides moves above each other it’s characterized as a successive slide (Dikau, 1996).

2.1.4 Translational slide

When a slide has a non-circular and planar sliding surface, the mass movement is characterized as a translational slide. The failure is generated by surface weaknesses (joint surfaces, faults, and increased pore-pressure and shear strength variations) within the parent material (rock, debris or soil). Depending on these different weaknesses and parent materials, the translational slides show different characteristics in the field. For example, a rockslide consists of a single unit or several units of the same material that move down slope, also known as a graben. But other types of slides are more related to the thickness, moisture content or material type, such as debris, soil or rock (Dikau, 1996).

2.1.5 Lateral Spreading

Lateral spreading is a distinctive mass wasting process on very gentle or even flat slopes. The mass laterally extends over a softer and underlying material. The failure is caused by viscos-plastic deformations, known as liquefaction or failure in the underlying softer material. This results in slumping and lateral spreading of overlying layers or rock (Dikau, 1996; Selby 1993). The deformations can result in failure or fracturing of the overlying slab of rock. At the edges of the original extent of the overlying rock, deformations can result in other types of mass wasting processes due to local weakening of the rock.

2.1.6 Flows

Closely related to slides are the different types of flow that can be distinguished. Major difference with slides is that the particles travel separately within the moving mass. The flows consist of what material is available on the slope and can therefore contain rock, debris or different types of soil. Rock flows are characterized by a relative small displacement compared to the large volumes involved. In the case of debris flows, a distinctive source area fails due to excessive precipitation. Soil flows are caused by strong liquefaction or complete saturation (Dikau, 1996; Selby, 1993).

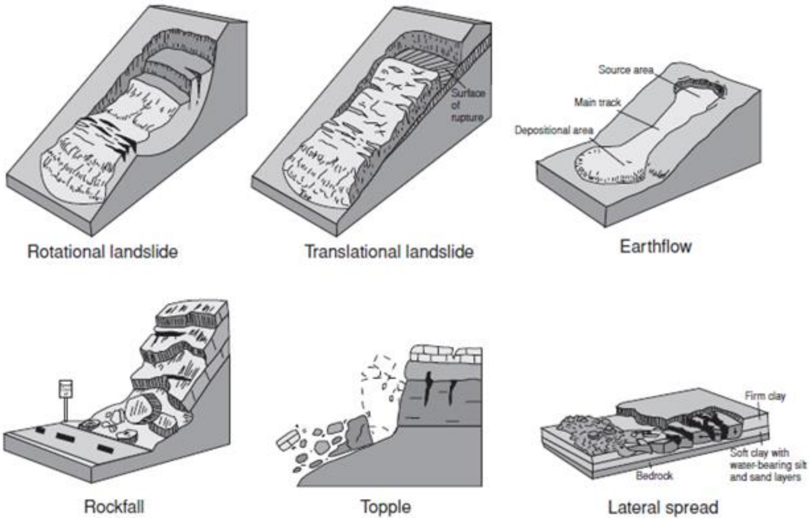

Figure 2.1. Various types of mass movement (Varnes 1984).

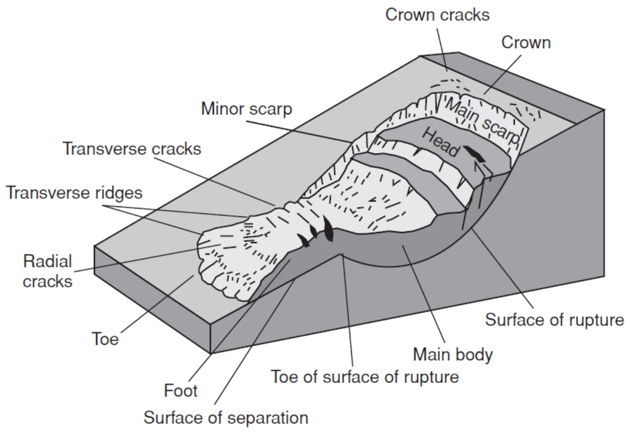

Figure 2.2. Rotational landslide elements after Varnes (1984)

While studying landslides, several typical elements of a landslide body can be distinguished (figure 2.2). For example, the boundary between the mass movement and the undisturbed soils: the failure surface. The location of this surface is in general determined by the geotechnical soil characteristics related to the slope angle (Terlien, 1998). The main scarp exposes underlying parent material and separates the crown of the landslide with the head of the mass movement. The main scarp is often an indicator for the shape and location of the surface sliding. Another indicator can be the location of the end of the failure surface, in figure 2.2 indicated as the toe of the failure surface. Other morphological features such as the toe, cracks and fissures are related to the deformation processes in the body of the landslide and can provide information about flow rates, velocity and activity (Metternicht, Hurni & Gogu, 2005).

2.2. Causes

As explained in section 2.1, a variety of mass movement types and related magnitudes exist. All of them depend on different processes, some being quasi static while others are more dynamic causes (Varnes, 1984). The quasi static variables, such as geology, elevation and other (soil) mechanical aspects tend to determine the susceptibility to mass movement of a certain area. The dynamic variables, related to hydrology, climatic properties and vegetation characteristics tend to induce mass movements (Wu & Sidle, 1995).

2.2.1.Quasi-static causes

To determine susceptibility for failure of slopes or the stability of the slope, including the basic mechanics of soils and slopes is crucial. Under gravitational forces slopes flatten out, if it was not for the cohesive and frictional forces. Especially the stress and strain behaviour of soils should be related in a direction to relevant forces in opposite directions (Wu & Sidle, 1995).

Stress is the force intensity per average unit area upon (N/m^2) which it acts, such as pulling or pushing. So, when a force is applied to a body of mass, internal forces are activated, causing the material to be in a state of balanced stress:

$$\sigma = \frac{\mathrm{F}}{A} \tag{2.1}$$

Where σ is *normal stress*: a stress component perpendicular to the cross section of the material (figure 2.3.), *F* the applied *force* and *A* the cross-sectional area. Processes such as rapid seismologic movements and geometry changes, have a potential to affect the stress conditions on slopes (Varnes, 1984; Selby, 1993).

When a load *Fn* is applied parallel to a material it results in *shear stress* (N/m^2):

$$\tau = \frac{\mathrm{Fs}}{A} \tag{2.2}$$

Where τ is the *shear stress*: a stress component down the shear plane (figure 2.3.) because of load *Fn* applied to the cross-sectional area *A*. This can be either a compressing or stretching stress. The effective stress is often used in geomorphological studies, such as mass wasting, because it is relevant for long term slope conditions (Embleton & Thornes, 1979). *Shear stresses* are also related to the steepness of the slope and the weight of the material. Steeper slopes and regolith with more mass contribute to the total stresses on a failure plane, as will be explained in the coming sections.

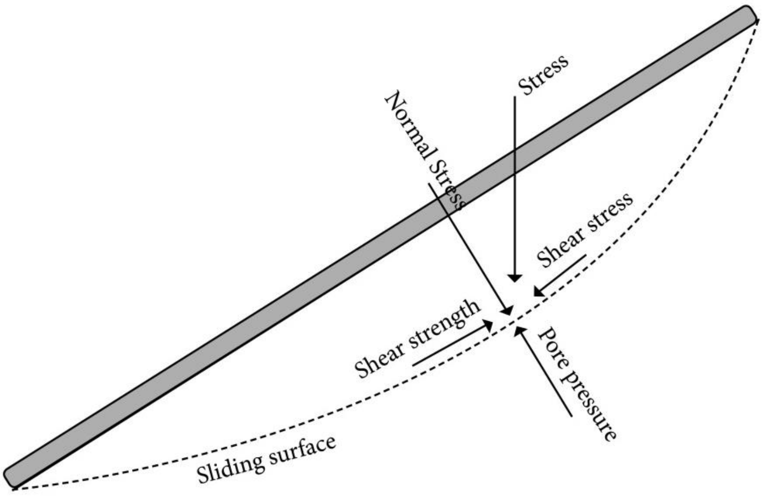

Figure 2.3. Forces acting on a failure surface (after Hoek & Bray, 1981)

Strain (ε) is a measure for deformation, measured as the amount of volume changed due to the stress imposed on a body of mass (Selby, 1993; Embleton & Thornes, 1979). It is generally defined as the change in length (*δz*) divided by the initial length (z_0):

$$\varepsilon = \frac{\delta \mathrm{z}}{Z_o} \tag{2.3}$$

The amount of deformation associated with several layers sliding over each other, is referred to as *shear strain (γ)*:

$$\gamma = \frac{\delta \mathrm{h}}{Z_o} \tag{2.4}$$

Where *δh* is the deformation perpendicular to the failure surface and z_0 is its original length.

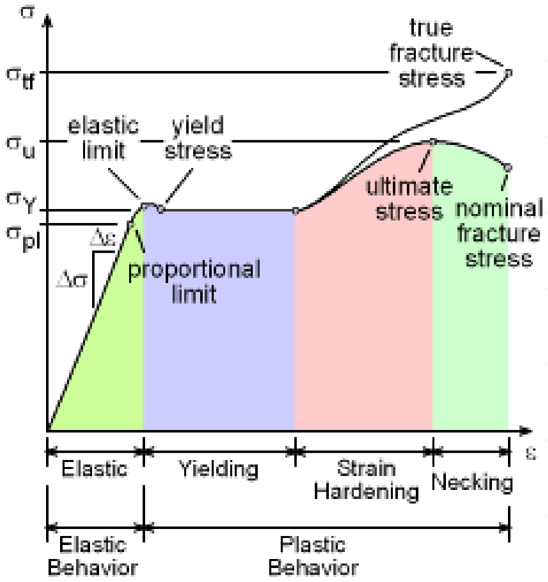

Figure 2.4 Stress – strain relation. With on the X-axis the strain and Y-axis the stress (Embleton & Thornes 1979)

The linear relationship between *stress* and *strain* can be related to each other and be expressed in the stiffness of a material. This relation states that stress is proportional to strain of a material. But due to ongoing deformation, materials can be strained permanently, making the relation no longer linear. The stress-strain curve shows this behaviour when a material is subjected to an evenly spread and increasing load (figure 2.4). This applied normal load results in a resisting *shear force,* eventually causing the material to fail. The maximum of the mobilised shear strength force defines the soil *strength*. Strength is therefore an important and relevant characteristic of material, it indicates at which strain the material will fail and thus how well it resists shear stress. The point where forces exceed the elastic limit, and the material will not return to its original shape when the stress is removed, determines the yield strength.

In case of materials resisting forces on a slope, shear strength consists of the combined magnitude from forces resisting downward movements. Processes related to weathering or precipitations are examples of processes with a direct effect on the strength of a material, due to their effect on the effective cohesion and frictional resistance of the material (Selby, 1993; van Beek, 2003). Where effective cohesion is a resisting force per unit area as a result of bonds between the particles that make up the material. Frictional resistance is related to the maximum angle to which a material can be exposed to without failure (Embleton & Thornes, 1979). Strength is therefore in short, a measurement of the ability from a body of mass to withstand a deformation (*strain*) caused by *stress*. Simon and Collison (2002) express the shear strength of saturated soils by the Mohr-Coulomb criterion:

$$\tau_f = c' + (\sigma - \mu_w)\, tan\, \phi' \qquad (2.5)$$

With τ_f the *shear stress* at failure, c' the *effective cohesion*, σ the normal stress, μ_w the pore water pressure and ϕ' the effective angle of shear stress often called the angle of internal fraction or the friction angle. T_f is thus the maximum amount of stress exposed to the material before failure, indicating the strength of the material or its shearing resistance.

Other forces that work on the material (figure 2.3) of the slope are a vertical acting gravitational force and the opposing upward pore-water pressure (Selby, 1993). When the maximum shear stress is mobilized, and overcomes the resisting forces, the mass will move along the length and in the direction of the failure plane.

2.2.2. Hydrology

It has been suggested that spatial and temporal variability in complex hydrological processes, such as runoff, infiltration, interception and precipitation (figure 2.5) govern the behaviour of many mass movements (Selby, 1993; Malet et al., 2005). Each of the in- and outward fluxes of water affect the groundwater table, which in its turn determines the saturation of the soil, the cohesion and the pore water pressure (van Asch, van Beek & Bogaard, 2009; Selby, 1993).

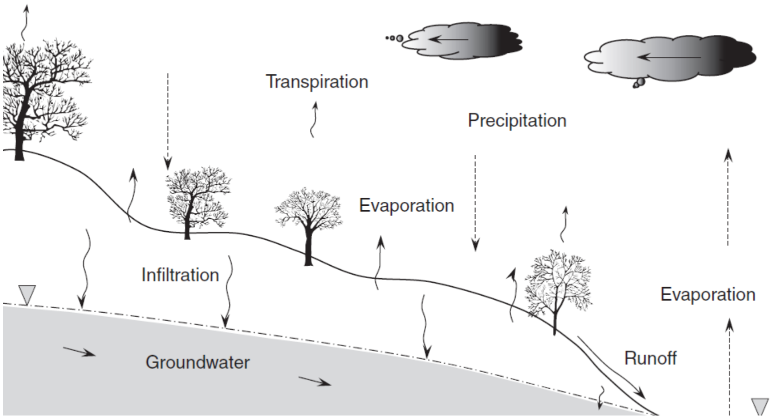

Figure 2.5. Incoming and outgoing water fluxes in a hillslope environment, after Malet et al. (2005).

Pore pressures relate to the force water can apply to pore spaces within a material. Above the groundwater table, pore pressures are negative; below the groundwater table the pore pressure is positive. The *normal stress* (σ) (equation 2.1) upon a body of mass is thus affected by the contact of particles, called the pore pressure (*u*), after Parry (2004):

$$\sigma = \sigma' + u \qquad (2.6)$$

The relation is supported by observations of mass movements after heavy or long rainfalls events. This suggests the importance of infiltration from above or rising groundwater table and the subsequent pore water pressure changes (Embleton & Thornes, 1979; van Asch et al., 1996; Malet & Maquaire, 2003; Terlien 1998). Completely saturated soils also result in an increased normal force on the slopes due to the added weight of water.

The relation between stress and pore pressure implies that the amount of water infiltrating and the infiltration capacity of a soil (Horton, 1933), are key concepts in the stability analysis of hillslopes:

$$f = f_c + (f_0 - f_c)\, exp^{-k_f t} \qquad (2.7)$$

Where the infiltration capacity f is determined by: f_c, a minimum steady constant infiltration capacity; f_0 the infiltration capacity at time t = 0; and k_f a permeability constant that reflects the hydraulic properties of the material. Making the infiltration capacity the maximum rate at which water can be absorbed by an area of soil. Infiltrating water fluxes, exceeding this maximum rate, often result in overland flow of the excess amount of water.

These hydraulic properties (e.g. conductivity, porosity and permeability), summarized in equation 2.7. as k_f, are especially relevant when the fluxes of groundwater are considered and the rate at which they flow in saturated systems. In general, a flux of water is determined by the gradient, in case of groundwater, almost always parallel to the slope (Ghestem, Sidle & Stokes, 2011). But more precise, the flux is related to the soil-water potential, consisting of a matric potential (ΔΨ), pressure head and an osmotic potential. The matric potential is thus a logarithmic property that is related to forces holding water to soil particles, because of osmotic-, pressure- and gravimetrical forces (Selby, 1993). When there is a height difference, the directional flow occurs. In the saturated zone the flow becomes partially determined by hydraulic conductivity, a measure that describes the ease with which water moves through a saturated area of soil (van Beek & van Asch, 2004). The hydraulic conductivity is on its turn determined by the permeability of the soil: the ability of the area of interest to transmit water. Darcy's law describes this combined effect of gradient and hydraulic conductivity properties of a soil on the water flux through a saturated system as followed:

$$Q = \frac{-\,K\,A\,(\Delta\,\Psi)}{\Delta Z} \qquad (2.8)$$

Where Q is the flow in m^3/s, K the hydraulic conductivity ($m^{-1}d\ d^{-1}$), A the cross-sectional area (m^2), ΔΨ the matric potential (kPa) and ΔZ the distance (m) over which the pressure drop is taking place.

Unsaturated systems are more common in mountainous areas, and are characterized by the absence of a hydraulic gradient, the presence of large macro-pores and water in smaller pores. These, and soil properties such as dry bulk density, determine how much water will infiltrate from the surface to the unsaturated zone and how much will cause overland flow and thus erosion (Dirksen, 2000). This makes dry bulk density, porosity and hydraulic conductivity important indicators for the infiltration characteristics that affect the slope stability (Campbell & Henshall, 2000). Macro pores are large radii in the soil, with consequently little matric potential. As a result, significant amounts of water will flow through these macro pores when the soil is saturated.

The available matric potential (ΔΨ) is much lower in the unsaturated zone, making fluxes of water there slower due to a changing ratio soil to water, compared to the saturated systems (Selby, 1993). Figure 2.6 shows the relation between hydraulic conductivity, water content and matric potential. Variation in pore size leads to saturated and unsaturated flows occurring at the same time over a narrow range of energy potential. But in general, a higher hydraulic conductivity is clearly related with saturated soils. This implies that flow of water occurs for saturated soils at lower energy potentials than for unsaturated soils, suggesting a relation between the soil water content and matric potential, aggregated in different characteristic of water release from the soil (Townend, et al., 2000). Usually this function between soil water content and the potential can be plotted in soil water retention curves (figure 2.6), each curve being typical for the given soil sample or texture class, due to unique status of consolidation, particle arrangement and aggregation. Porosity and field capacity of soils are two characteristics that can be derived from the soil water retention curve. The maximum amount of water that a soil can hold after drainage due to gravitational forces is the field capacity of water. This implies that a saturated soil allowed to drain will decrease via gravitation drainage (assuming no infiltration, evaporation etc.) until the rate is negligible, reaching the field capacity. The values often range from 0.1 for sands to 0.3 for clays. The total porosity influences the amount of water that can be stored in a soil. Porosity depends on particle size, compaction and pore distribution. Fissures and cracks can lead to preferential flows and rapid infiltration, altering the permeability and conductivity of the soil. Both aspects can affect the soil-water potential, and the retention curve, significantly.

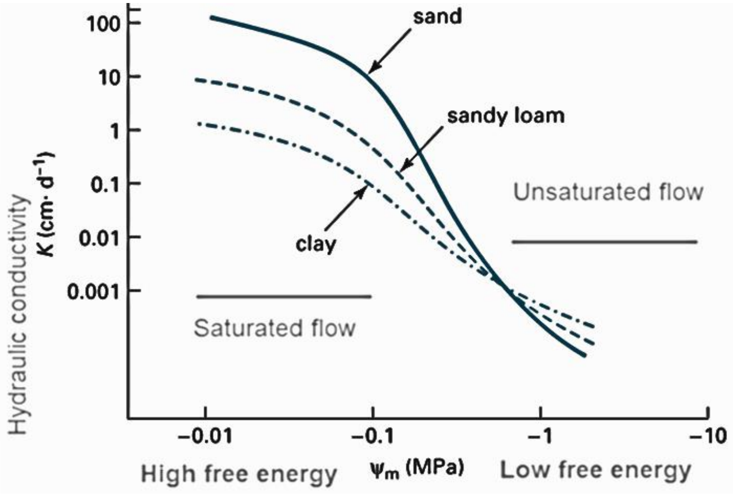

Figure 2.6. Relation between matrix potential (energy) and hydraulic conductivity for different soil types. Variation in pore size is here displayed as different texture classes (Selby, 1993)

2.2.3.Vegetation

Vegetation is an actor that is often used to characterizing the mass movement and its state of activity (Schlögel et al. 2015). Active movement can for example be distinguished where vegetation is lacking or tilted, or only pioneer species are found. But besides vegetation being an indication of activity, vegetation also has a direct impact on slope stability through hydrological and mechanical processes (Ghestem, Sidle and Stokes, 2011). Both individual and aggregated vegetation species can either support or attenuate the stability of the slope.

Rainfall interception, retention, interception, transpiration and root uptake are only a few examples of how processes, because of vegetation, affect the water balance in the slope systems. As described in section 2.2.2 the lowering of the water balance is significant for the increase of the (undrained) shear strength due to the decreasing pore-water pressure. When precipitation or other replenishing processes, lead to an increasing water table, the resulting increasing pore-water pressure could destabilize the slope (Ghestem, Sidle and Stokes, 2011). This suggests that the amount of vegetation can have an indirect effect on the slope stability, via the fluxes of (ground) water.

Larger vegetation species or aggregated clumps of species can also increase the loading of a slope significantly. The vegetation either increases the mass acting on a slope, thus increasing shear stress, or it increases normal stress and therefore shear strength due to friction (figure 2.3.). This partially depends on the location of growth; at the top of the slope or the toe respectively (Simon & Collison, 2002). Vegetation can also improve the stability of the slope via strength of roots and the compaction effect of vegetation, on the soil strength. The overall effect of vegetation on slope stability, whether positive or negative, is in general limited to the top soil layers of the slopes, due to the limited reach of roots. Simon and Collison (2002) suggest it to be likely that the combined effect of extra weight and detrimental hydrological processes rarely outweigh the beneficial effects of increased stability due to root reinforcement and moisture reduction, especially for landslides with a failure surface 3 - 4 meters below these top soil layers.

2.2.4.Climatic factors

The climate influences mass wasting processes, due to global temporal- and spatial fluctuations in temperature and precipitation (Lu & Godt, 2013). The climate can therefore contribute to the net effect of failure parameters, which are described in earlier sections. Depending on seasons these effects might be negligible; for example, during winter's landslide activity is larger while expected vegetation activity is lower than for summer seasons. Another example can be related to temperature changes and its effect on the water capacity of the atmosphere. A higher temperature allows more moisture to evaporate into the atmosphere and thus potentially affect precipitation over mountainous regions.

Many of these abiotic parameters are slow processes that determine the different regimes in which mass wasting processes can take place (Selby, 1993). But especially the regimes related to precipitation are considered significant due to their triggering effect on landslide activity, as described in section 2.2.2.

2.3. Triggering mechanisms

Several types of mass movements exist, each with its own characteristics. Although each type of movement has its own specific causes, they are all related to the general principles and causes of surface failure, described in section 2.2. Mass movements will only occur when the resisting forces (shear strength) are smaller than stress forces (equation 2.9), often initiated by a triggering event. This ratio can be expressed as the Factor of Safety (FoS) of the slope:

$$\text{FoS} = \frac{Shear\ strength}{Shear\ stress} \tag{2.9}$$

When the FoS ratio falls below one, the resting forces are failing and the hillslope will start to move to a new equilibrium. This movement towards a new stable state can be attributed to the different movement mechanisms, such as fall, slide, topple, flow and creep (Embleton & Thornes, 1979). These triggers for mass movements can be divided into two categories: internal and external. External causes are related to an increase in shear stress while internal causes are generally related to a change in resisting forces. Some causes are related to both internal and external principles. Examples of external causes that can be related to a change in the force acting upon a body of mass (Embleton & Thornes, 1979) are:

- Changes in geometry, can affect the stability of a slope due to exceeding the critical movement thresholds in terms of height, unit weight, shear strength and angle of the slope.
- Loading of extra material, can result in new slope equilibrium due to extra shear stresses affecting the potential failure surface.
- Unloading, the removal of materials from the slope that lead to internal changes affecting fissures, reduce strength or the lateral expansion.
- Vibrations, affect the horizontal driving forces acting on a slope instantly resulting in failure when the safety factor reduces to one.
- Liquefactions, occurs when a saturated mass loses its shear strength and starts to behave like a fluid. This can generally be attributed to an earthquake or other forms of rapid loading resulting in a denser compaction of the soil particles. The resulting decrease in porosity will cause the movement of soil particles be affected by the remaining fluids.
- The hydrological cycle, affected by precipitation and the extraction of water. Especially when this happens in a short time frame the resulting changes in pore pressure and cohesion affect the shearing strength directly. Failure can be caused by saturation of the failure surface, increasing the pore-water pressure acting on it and therefore the shear stress. The increase in pore water pressure can result from the percolation of rainfall or by accumulation of groundwater near the failure surface (Lu & Godt, 2013; Terlien 1998).

As opposed to external triggers of landslides, the internal causes result in a reduction of resisting shearing- or strength forces:

- Weathering; results in a reduction of the cohesion of the material, under natural forces of water, air or chemicals. Because of the interaction, the original strength of the exposed material is altered. Besides the reduction of cohesion, weathering also affects the characteristics of the mass movement. Water table changes, formation of regolith, pore-volume changes; changes in cohesion and increase in pore water pressure are but a few of the effects of weathering on slopes.
- Processes such as seepage, were water percolates through fissures, cracks and joints, affecting the surface tension of saturated top soils.
- Soil creep; decreases the shear strength due to the constant deformation of soils. A well-known example is the thaw-freeze cycle that causes materials to shrink and grow when freezing water inside the soil expands.

Erosion is an example of a process that both affect the shear strength as the shear stress on slopes. The resulting downslope movement of soil is a result of increasing pore water pressure (stress increase) and loss of cohesion (strength reduction) (Montgomery & Dietrich, 1994).

The variety in mass movements gives an indication of the complexity of mass wasting and related processes. Often for individual mass wasting events, such as the Charonnier landslide, the relevance of the here described processes and triggers are not fully understood. Only research in the stability, and the processes that affect it, allow differentiating between the relevant actors.

3. Local conditions

In the wet winter of 1993-1994 a body of mass was activated and moved downslope near the Charonnier river (figure 3.2). The resulting landslide is in the French Alps, the department of the Haute Alps, near Veynes and the city of Gap. The department is located west of the Italian Alps and surrounded by the departments of Drome, Isere, Savioe and Alpes-Hautes Provence. The Charonnier River is a small branch of the Le Drouzet River that drains in the small river Le petit Buëch, making it part of the Buëch watershed or the larger Durance river watershed. The landslide is very well accessible via the road that connects Veynes with Barcillonette and Tallard. Due to its small size and corresponding low risk, no research has previously been reported on the current state of its activity; inactive, dormant, stabilized or relict.

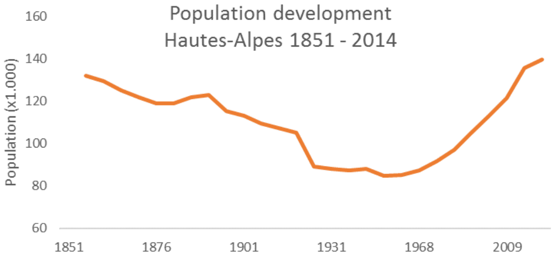

Figure 3.1 Population development in the department Hautes-Alps between 1851 and 2014 (Insee, 2016).

The department Haute Alps is located within the Durance watershed on the boundary of the alpine and Mediterranean climate zones, experiencing an annual precipitation around 900 - 1000 mm in the whole catchment (Mathys et al., 2003). The area has a long-reported history of human influence starting as early as 6000 years ago (Olivier et al., 2009). Since the 19th century the population has been decreasing (figure 3.1.) after it first experienced a steady increase since the 16th century (Descroix & Mathys, 2003). With the fluctuations in population density over the century, with a peak during the industrial revolution, came the changes in land cover and – use. A clear example is the steady decrease in forest cover till the late 18th century, followed by an early reforestation with at least 30% forest cover today (Descroix et al., 2005; Olivier et al., 2009). Land use in the area is divers because of variations in morphology and climate. Valleys are often used for agricultural activity and the hillslopes for livestock activity, vineyards, orchards or forest cover. In the last decades' tourism has increased significantly during winter and summer seasons, contributing around 10% to the gross regional product (Olivier et al., 2009).

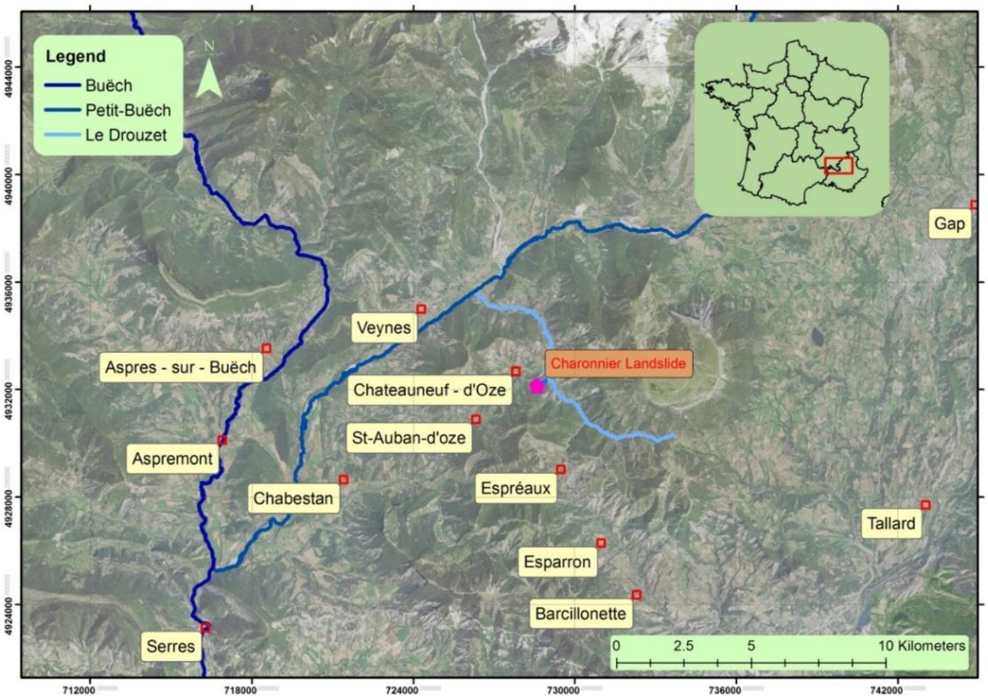

Figure 3.2 Haute – Alps region with the major villages and the relevant branches of the hydrological network.

3.1. Geology and geomorphology

The region of the Haute-Alpes has significant altitude differences, with mountain tops ranging from 500 to 4302 meters. The lithology is characterised by alternating marl and limestone outcrops, deposited during the Jurassic and Cretaceous time frames. The oldest marl deposits from the Oxfordian era are known as the “Terres Noires” which have significant outcrops in the entire south-east of France (Maquaire et al., 2003; Antoine et al., 1995). The Terres Noires are stratified sediments with 3 layers: impermeable black marls from the lower Callovian, highly permeable limestone alternated with marls, from the Oxfordian and an upper unit, with marls from the Argovian. Due to the similarity of the top and bottom marl layer, the Terres Noires can look like a homogeneous layer in the field (Antoine, 1995). The outcrops are a result of the Alpine thrusting uplift in north south direction during the early tertiary (Boogaard et al., 2000) causing crystalline from the Eocene to overlay the black Marls (Macquaire, 2003). The contrast in permeability between black Marls and the crystalline can be observed near outcroppings and over-thrusts, causing springs to occur.

These highly erosive layers of the Terres Noires, on top of the unweathered bedrock (up to 2500-meter-thick), are characterised by a meter-thick homogeneous top layer of fine flat shaped plates, with on top a completely disintegrated silty colluvium layer of 1.5 meter with a very fine particle size (Antoine et al., 1995; Caris & van Asch, 1991; Descroix & Mathys, 2003). On the slopes, a thickness of the top layer has also been reported of several decimetres (Oostwoud et al., 1998). Due to these characteristics, the Terres Noires show geomorphological similarities to badlands: steep, rounded ridges with vertical sides, randomly created by drainage networks on hillslopes. These drainage networks facilitate the depletion of calcite on slopes and its deposition at the valley bottoms. This affects the cohesion and thus erosion processes on the slopes due to the loss of the compaction properties of calcite on these slopes. Therefore, the porosity in valley bottoms is often lower than on the hillslopes, where it increases because of weathering (Antoine et al., 1995). Changing porosity on the hillslope length, in combination with high intensity storms or abundant precipitation, can cause small mass wasting processes, such as erosion, mudslides or mudflows. These smaller mass wasting events are characterized by a shallow and planar slip surface, almost parallel to the surface (several meters deep) width a length in the range of 80 – 120 meters. Landslides in the Terres Noires can reach up to the unweathered bedrock, but are not very common (Antoinne et al., 1995).

The region of the Haute-Alpes was significantly subjected to dynamic morphological processes in the alternating glacial and periglacial periods during the Quaternary timeframe. Also, morainic materials were deposited throughout the valley bottoms of the major tributaries. After these alternating glaciation periods ended some 12.000 years ago, the climate significantly changes during the Holocene. A near complete forest covered the whole of the Buëch basin, with an aggregation period, where sediments are filling the bottom of many secondary valleys (Descroix & Gautier, 2002). The second half of the Holocene is associated with a more erosive period, also showing the first signs of human activity and shorter climatic oscillations. During this Neolithic period, human settlements become more abundant, resulting in the first signs on deforestation and overgrazing. More recently, relative small and short oscillations, such as the little ice age (1230-1350), two centuries of slightly higher temperature, severe deforestation in the 18th and 19th century and an increase in human activity affected area (Kappes et al., 2011). These events, and related morphological activity, can be analysed via the first maps and aerial photography. For example, river dynamics, such as widening of the riverbed, braided patterns, the development of gravel bars and the development of badlands can be observed (Descroix & Gautier, 2002). Despite a demographic decrease more recently and reforestation, eroded areas remain degraded, with gullies and badlands exemplary signs in the landscape.

In the direct area around the Charonnier landslide the lower part of the slopes now consists of the described Terres Noires, while the upper part of slopes consists of Limestone of the Argovien era. It can be observed in historical imagery that the Charonnier river incised in the original hillslope, while after the landslide event, changed its drainage directions (Aerial Imagery, IGN).

3.2. Climate

The climate in the Haute-Alpes is characterized by high seasonal variations (figure 3.3) in both precipitation and temperature (Maquaire et al., 2003). Dry summers do have high intensity rainfall events, with corresponding high kinetic energies. September, October and November are the wettest months, where snowmelt affects the hydrology in spring time. During winter time the precipitation is often snow or long rainfalls, resulting in extra water in the slope systems during spring (van Asch, van Beek & Boogaard, 2009; Descroix & Gautier, 2002;). The distinctive variation in temperature results in many thaw-freeze cycles in winter months, depending on the location ranging from 80 to 160 cycles per season (Descroix & Mathys, 2003; Maquaire et al., 2003). Groundwater fluctuations for the Terres Noires in the region are reported to fluctuate between 6 to 0.5 meters below the surface (Maquaire, 2003).

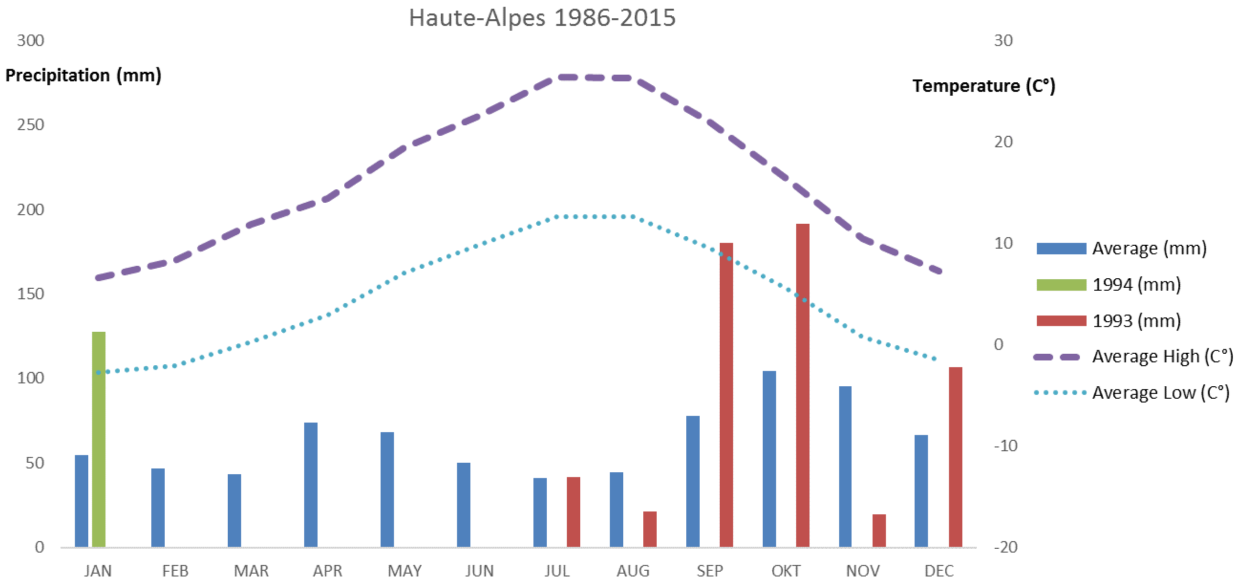

Figure 3.3 Average precipitation (with standard deviation) and temperature in the Hautes Alps region between 1986 and 2015. Precipitation between July 1993 and January 1994 are displayed for comparison, (Meteo France, 2017).

4. Methods

Different methods can be applied to analyse landslides, depending on the desired objective. When one for example, wants to use zonation to analyse regional or global landslide risks, different remote sensing approaches can be used. A range of sensors and platform types give the opportunity to take different extrinsic factors into account. On the other hand when parameters, which cause landslides, on local or watershed level are relevant, a modelling approach is possible. In general, landslide stability analysis requires several types of in situ observations or remote sensing data; but most of the time a combination of both.

Landslide research can be focussed on identifying the spatial extent of areas susceptible for mass wasting processes, because of certain topographic or hydrologic mechanisms (van Beek & van Asch, 2003; Malet et al., 2005; Schlögel et al., 2015). Clear examples of these processes and mechanisms have been discussed in chapter two, such as a steep slope, mass availability and failure parameters. But to establish the stability of the Charonnier landslide a combination of methods was applied. By complementing a DSM and orthomosaic with in situ observations, a detailed overview of the landslide is created. Field measurements, with respect to controlling aspects of mass movement, like infiltration capacity and soil strength, allow modelling the current and future stability of the landslide.

4.1. Remote Sensing

Remote sensing tools comprehend techniques to recognize, monitor and predict landslide movement via earth observations (Scaioni, et al., 2014; Pajares, 2015). Remote sensing tools are well suited to analyse relations between mass movement types, process controlling aspects and triggering factors such as geomorphology, land cover, hydrology, topography, geology and the presence of man-made structures. This implies that different properties of landslides can be analysed with remote sensing tools (van Beek, 2003). For each aspect of interest different combinations of sensors and platforms are possible, all with their own advantages and disadvantages. One of such aspects of interest, are digital terrain or surface models, which approximate the earth surface, including objects on the surface (DSM) or approximating the actual terrain (DTM). Both products are well suited to study the spatial variation in morphology at the Charonnier Landslide.

Depending on the requirements of the output such as scale, resolution and temporal coverage of the model, a wide range of platforms is available. Often the type of sensor dictates the platform type that can be used due to limitations in for example stability, weight and power (Lillesand et al., 2014). Certain of these sensors act as their own source of energy, making them active such as radar or lasers sensors. Other sensors only relate to the naturally emitted energy from the object of interest, such as optical sensors (Lillesand et al., 2014). Classifications of these sensors generally relate to the part of the spectrum they are taking their information from. Objects on the earth emit and reflect energy with various distinctive signatures, such as wavelength, that provide information about the feature under investigation. Based on the wavelength the electromagnetic energy, like heat, visible light, Ultra-Violet (UV) and radio waves, can be assigned to the electromagnetic spectrum (figure 4.1). Each of these electromagnetic signals (in Nanometres) can be extracted with different sensors to analyse reflection or emittance characteristics from the object of interest.

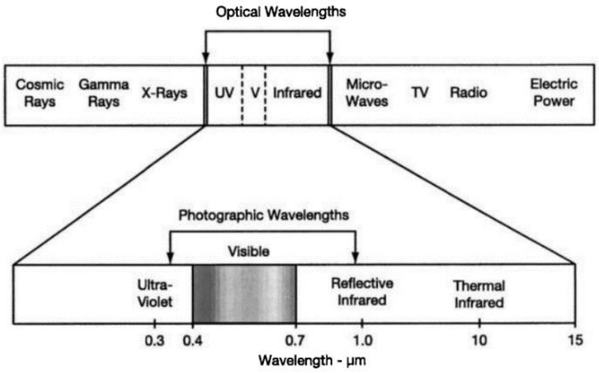

Figure 4.1. All the wavelengths (in nanometres) with an enlargement on the optical spectrum (After Landgrebe, 2005).

One type of sensors, often used in landslide research, is focussed on the photographic wavelengths (figure 4.1): the visible part of the electromagnetic spectrum (390 – 700 nm). Near Infrared and Shortwave infrared spectrums are also considered to be in this optical part of the spectrum. Their usage often depends on the type of platform used to acquire the images: space borne or airborne. Especially aerial photography has often been applied in landslide research (e.g. Varnes, 1984) because coverage is sufficiently large, photographs are easy to use and temporal coverage can be controlled. Over the years' different platforms have been used to acquire these digital (or stereographic) photographs. For example helicopters, small aircrafts (Henry et al., 2002) and more recently Unmanned Aerial Vehicles (UAV's) (Turner, Lucieer & De Jong, 2015) are used to estimate the scene topography.

When extracting physical properties, such elevation, from these photographs the photogrammetry technique is applied (Mora et al., 2004). The displacement between two (or more) overlapping images allows the retrieval of topography because the same object is displayed at different heights relative to the other image, by an amount related to their actual altitude (Lillesand et al., 2014), when the exact location and pose of the camera are known. This principle has been applied to geomorphological research for decades but only more recently has a similar method been applied with UAVs: Multi-View Stereo Photogrammetry (MVS) (Clapuyt et al., 2016). As opposed to the traditional photogrammetry this method doesn't use known camera settings and triangulation to estimate topography. Instead control points can be identified within the image with known geographical coordinates (x, y and z), allowing the camera position to be determined for each photo (Westoby et al., 2012). In the MVS image processing workflow, conventional photogrammetric principles, such as location of pose and camera, are complemented with 3D vision algorithms (Smith et al., 2015) like Scale Invariant Feature Transformations (SIFT) and Structure from Motion (SfM) to build a dense point cloud that represents the surface. This allows the use of consumer grade, uncalibrated cameras, without internal camera parameters such as principal points, distortion, focal length or distance to the surface.

The dense clouds acquired by UAV (as well from other) platforms can be used to generate representations from the studied surface, like an orthomosaic and a Digital Surface Model (DSM). The orthomosaic is based on the merge of rectified photographs with a uniform and high resolution. It provides the user with a product that uses true distances and easy interpretation of features, like in a photograph (Lillesand et al., 2014).

4.1.1.Image acquisition

For every remote sensing project, there is a trade-off between resolution, spatial coverage, image quality and cost effectiveness (smith et al., 2015). Due to the relative small size of the Charonnier landslide, the amount of spatial coverage is not a challenge, allowing the use of a small UAV. With its relative low flying height (table 4.1.) high resolution images can be obtained. So, to obtain the highest pixel resolution and image quality with the material available, flying height, -speed and stability of the sensor are the relevant aspect to consider. The more stable the platform can fly, the less distortion in the final images, as with any other remote sensing platform (Lillesand et al., 2014). The stability of a sensor is often recorded with an internal GPS system and characterized as pith, yaw and roll movements. Due to the lack of an internal GPS system during the flights these factors are excluded from this image analysis.

Not only is the stability of the platform of importance when aiming for maximum quality. Because the number of pictures and their quality (sharpness and resolution) determines the quality of the final 3D point cloud, it is important to consider other orientation factors of the sensor. For example, the distance between the sensor and the object is of interest (equal to flying height, see figure 4.2); decreasing the distance will improve the spatial resolution (Westoby et al., 2012) according to the following relation:

$$Scale = \frac{f}{H-h} \tag{4.1}$$

Where f is the focal length, H the flying height above the chosen datum and h the flying height above the terrain (Lillesand et al., 2014). Another relevant factor is the orientation of the camera, either oblique or vertical. Oblique aerial photos are taken with the camera under an angle, with or without the horizon in the photo. Vertical photos are taken with the lens parallel to the terrain. Since the ability to determine height and from images is determined by multiple viewpoints of the sensor, sufficient high quality pictures from different angles are required up to a certain maximum orientation angle.

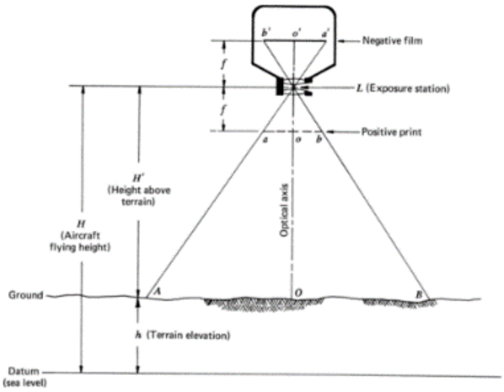

Figure 4.2. Internal orientation elements of an optical sensor (Westoby et al., 2012).

With these aspects in mind a flight campaign was organised during the fieldtrip. Low altitude aerial photos were collected with a Canon compact digital camera (Powershot D10, focal length 6.2 mm and 12 MP resolution) connected to a polystyrene fixed wing flying platform with a span of 2 metres. The sensor captures pictures in JPEG format with a lossy compression, reducing the size of files. Between June 3rd and 5th 2016, nine flights were performed with an average flight time of fourteen minutes, taking in total 1428 pictures (table 4.1). Flying was performed between 12:00 pm and 14:00 pm where possible, to avoid long object shadows in the images. Due to unexpected rainfall on June fourth, the remaining flights were performed on June fifth. The total area covered was approximately 0.24 km^2 and the pictures were taken from an average of 117.6 meters above ground. Due to topography and resulting limitations in line of sight the pilot was forced to manually control the UAV and depart from three different locations to maintain visible contact with the UAV, causing variation in flying height and speed.

Table 4.1. Flight details. Flight 7 was excluded from analysis due to blurred images.

Date	Flight	Duration (min)	Pictures (used in analysis)	Average Altitude (m)
3-6-2016	1	12	136 (40)	103.9
	2	15	178 (57)	105.5
	3	11	95 (31)	92.9
	4	12	137 (63)	111.6
	5	14	161 (77)	106.1
4-6-2016	6	28	346 (243)	118.3
5-6-2016	7	12	72 (0)	0
	8	10	163 (106)	129.3
	9	10	140 (74)	142.1
Sum		124	1428 (691)	
Average		13.8	158.7	117.6

For the photographs a (non-metric) Canon compact camera was used, even though it has an unknown internal orientation. Thus, to be able to determine 3D locations within the photos, a reference system had to be created. As opposed to the traditional photogrammetry this doesn’t have to be done with camera settings and triangulation. Instead control points can be identified within the image with geographical coordinates (x, y and z), allowing the camera position to be determined for each photo (Westoby et al., 2012). For this reason, a total of 53 clearly distinguishable markers (figure 4.3.) and objects had been placed and measured with a Trimble differential GPS unit, from here on referred to as Ground Control Points (GCP). With the use of a differential Global Positioning System (DGPS) the GPS signals are accurately surveyed up to centimetre accuracy (Smith, et al., 2015). The differential GPS uses a modem to correct received satellite locations with satellite locations to a stationary location with known coordinates. Because each of the signals received contains a certain error a stationary measurement devise can correct the received signals in the field. The coordinates were referenced into the UTM 31N WGS84 reference grid.

Figure 4.3. Example of a ground control point visible within the images

4.1.2.Image processing

From the original 1428 pictures, images with major blur, outside the study area or with less than 80 percent overlap with other images, were removed. This resulted in 691 images useful for image processing in the Agisoft Photoscan software package, version 10.2 (2014). Before the image processing, masks were built to extract vegetated areas from the individual photographs that where situated outside the area of interest (see figure 4.4). The masks ensure that vegetated parts are not used in the construction of the vector DSM and feature matching. Vegetation on top of the landslide

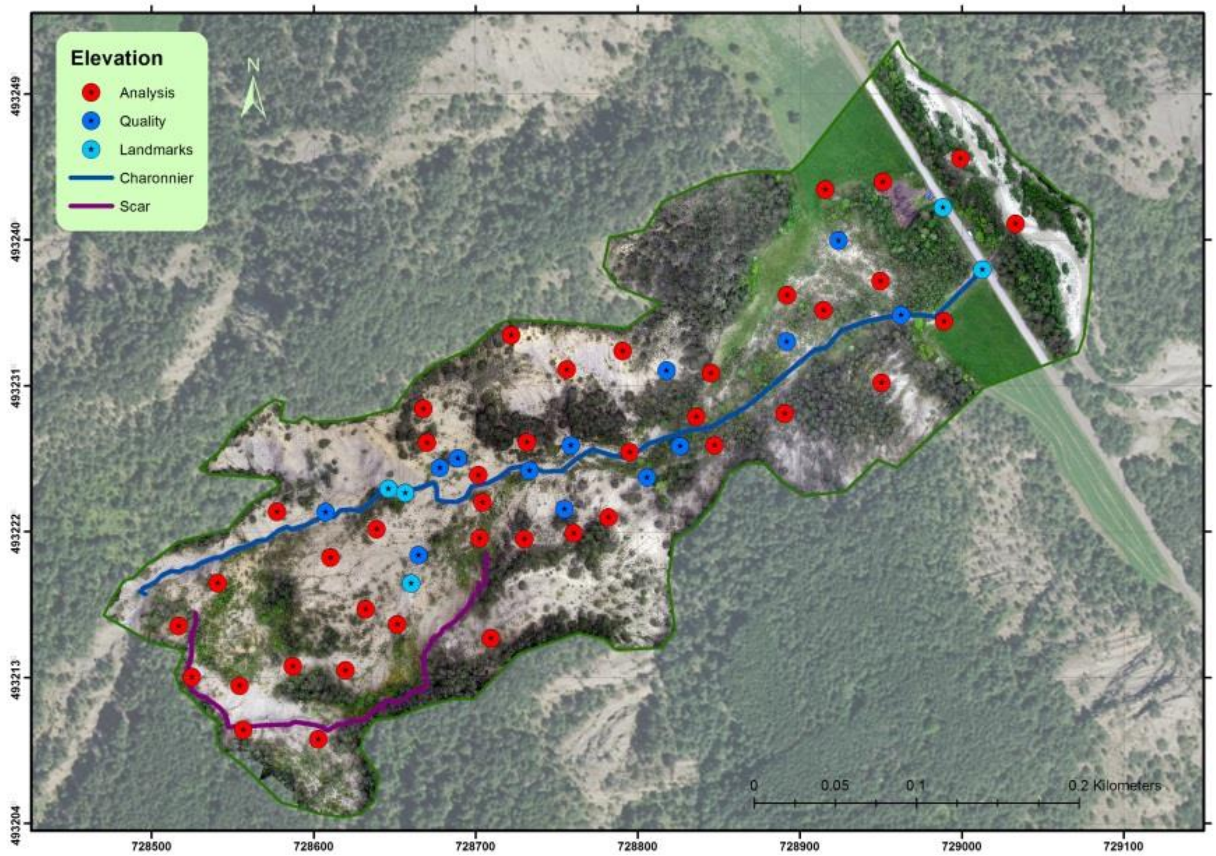

Figure 4.4. Charonnier Landslide with all GCP's and landmarks used in the analysis and quality control.

and within the area of interest was not masked out of the images to obtain a complete surface elevation model.

This Agisoft Photoscan package uses the MVS approach (figure 4.5) to obtain an elevation model from un-orientated and overlapping images: first, features are identified that remain constant despite changes in orientation; making them suitable for matching in each image. In the next step these identified features are related between key points in other images, subsequently descriptors are used to describe each feature (Smith et al., 2015). Despite difference in view point and scale the SIFT algorithm can recognize the features in different images based on colour gradients and image brightness (Fonstad et al., 2013; Clapuyt et al., 2016). After filtering the key point descriptors for erroneous matches, the structure for motion (SfM) bundle adjustment is applied. This algorithm uses the 2D recognized feature points to simultaneously estimate the 3D geometry of a scene and different external camera parameters, such as location (x, y, and z) and pose, as well internal parameters like focal length and distortion in the images (Fonstad et al., 2013). The output here is a sparse point cloud, with in this case 23,000 points, that can be scaled and georeferenced in the WGS84-UTM 31N coordinate system, with ground control points (GCP) visible in the images. These ground control points are tagged manually in the pictures using the Agisoft interface and matched with the real-world coordinates. The final step in this workflow is the point density increase of the sparse cloud up to 59 million points, via MVS image matching algorithms (Smith et al., 2015). With the resulting dense cloud, it is possible to construct a mesh interpolation of all the points where surfaces are displayed by triangular vectors: A Triangulated Irregular Network (TIN), representing the surface (Clayput et al., 2016). With the surface representation photographs can be rectified and distortion can be corrected and finally merged in an ortho-mosaic with a true representation of the surface (Niethammer et al., 2012).

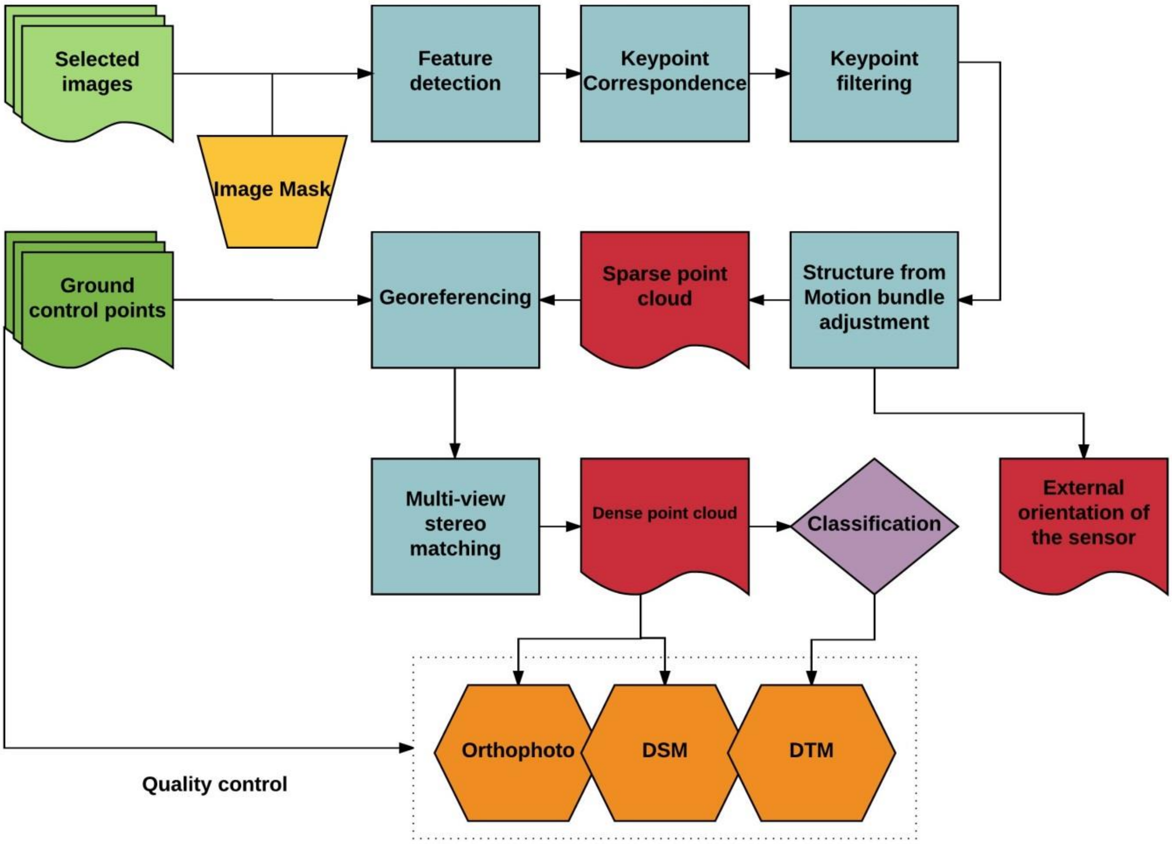

Figure 4.5. MVS Image processing flowchart applied in the Agisoft Photoscan processing environment.

As opposed to the active LIDAR sensors, the passive optical sensor used here only return a first signal, therefore representing the surface, including vegetation and other objects on the terrain (see Appendix VII). LIDAR can return a second signal, penetrating vegetation and thus representing the terrain in a digital terrain model (DTM) (Wallace et al., 2016). But also approaches exist to reconstruct the terrain from surface models generated from aerial photos. Many of these approaches are based on a technique where vegetation is removed and the open areas are interpolated. The AgiSoft software package for example allows the automatic or manual classification of the derived point cloud (figure 4.5). The automated classification is based on angle between adjacent cells and the size of a moving window. Rather than using trial and error to obtain the correct settings for automated classification, a manual approach was applied. Therefore, any point representing medium to large vegetation, such as trees and large bushes were classified and excluded from the texture generation. The result was used to determine the height of the terrain, excluding vegetated surfaces, to estimate a terrain model.

When it is possible to reconstruct the plane of the landslide surface and the plane of the failure surface it becomes possible to estimate the displaced volume (Nikolaeva et al., 2014; Lucieer et al., 2013). It is assumed that the exclusion of vegetation from the DSM results in an approximation of the DTM. The estimation of the failure surface is in general based on a pre-and post-event terrain model (Nikolaeva et al., 2014). Due to the lack of such a high detailed, pre-event, terrain model, pre-event elevation must be estimated based upon the surrounding surface. By interpolating the estimated original elevation from outside the active landslide area the reconstruction is possible (Feng et al., 2015). Due to the activity from the Charonnier River this is only possible in the areas where the difference between post- and pre-event can be visually classified. The boundaries from the toe (figure 4.1) with the surrounding fields are a clear example where such a classification is possible.

4.1.3.Quality control

There are different methods available to validate the output DSM and orthomosaic: point to raster, raster to raster and point cloud to point cloud (Smith et al., 2015). Since only point observations are available for verification and validation, the point to raster method can be applied. In this case, the remaining 13 ground control points and 5 clearly distinguishable landmarks, with known coordinates, are used to test the accuracy of the scaling and geo-referencing (see figure 4.3 and figure 4.4). These 18 control points were not introduced during the image processing and are therefore independent from the DSM. The visible location of the ground control points in the orthomosaic were pinned with ArcGIS tooling and assigned the corresponding X, Y and Z coordinates. A distance between the measured ground control point and the observed location of the marker in the orthomosaic can be measured (figure 4.6). The related angle indicates the direction of the error. This angle is expected to be random for all ground control points. When this is not the case, the area is most likely not photographed from sufficient directions; a bias exists in the error.

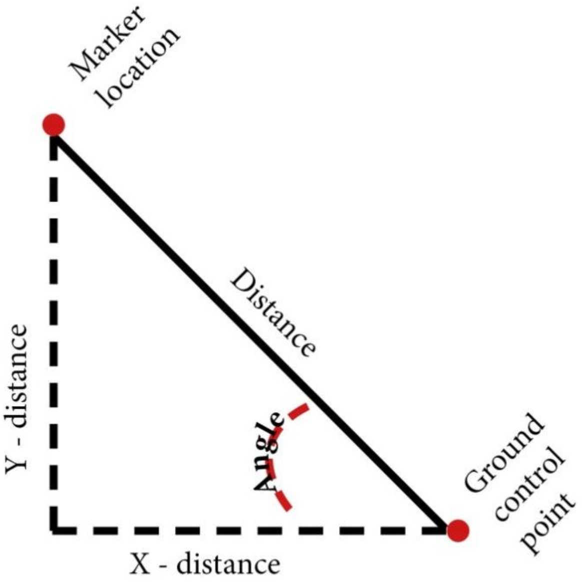

Figure 4.6. Near distance and the angle between the observed marker location and the measured ground control point.

4.2. Precipitation analysis

To establish the recurrence times of precipitation events the following assumptions were made: maximum values are realisation of independent random variables, no trend over time and the maximum values are identically distributed. The recurrence time (T) is then the mean number of years between two events with a certain amount of precipitation (*p*):

$$T\ (p) = \frac{1}{1-F(p)} \qquad (3.1)$$

F represents the cumulative distribution based on the ordered ranks (i) of all the yearly maximum rainfall events between 1985 and 2015 (N) from small to large according to:

$$F\ (p) = \frac{i}{N+1} \qquad (3.2)$$

The maximum daily precipitation doesn't take duration of rainfall events into account. Therefore, the precipitation of consecutive days with rainfall was summed in to one precipitation event, called antecedent rainfall (Terlien, 1998). The steps described in equation 3.1 and 3.2 were performed again to obtain recurrence times that incorporate the length of precipitation events.

4.3. Soil characteristics

In situ observations can provide the data for the establishment or confirmation of empirical relations and define parameters for models with their own distinctive spatial- and temporal variability (van Beek & van Asch). Laboratory observations on the other hand have a strong emphasis on excluding interactions from the process of interest. These laboratory observations allow the downscaling of space, or upscaling the timeframe under consideration (Embleton & Thornes, 1979). Therefore, a combination of both in situ- and laboratory observations is applied to obtain relevant soil characteristics for the stability assessment of the Charonnier landslide.

When sampling any phenomena in the field, the interval and size of the samples should be representative for the scale of the process of interest. The samples should also be able to represent the desired variability in the observed phenomena (van Beek & van Asch, 2003). For soil characteristic analysis, the landslide was therefore divided in an area with undisturbed parent material and an area with disturbed landslide material. A core method was applied to determine several relationships between these soil characteristics, based upon 36 samples. This is a destructive measuring method that can used to determine bulk density, saturation, porosity and moisture content (Selby, 1993). After the core is collected an inverse auger-hole test is performed to determine the saturated conductivity.

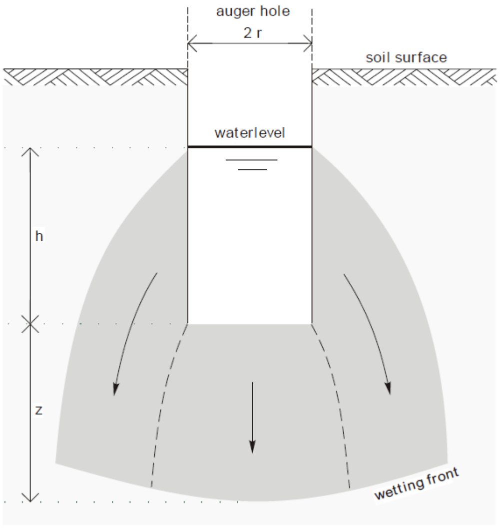

Figure 4.7. The concept of Inverse auger hole testing (Oosterbaan & Nijland, 1986)

4.3.1. Saturated conductivity

The saturated hydraulic conductivity will be used to for the description of the hydrology. It is assumed this parameter represents the maximum rate of flow in saturated conditions (see section 2.2) and thus can be linked to the flow rate in unsaturated condition through the conductivity according to Darcy's law (equation 2.8). The saturated hydraulic conductivity was chosen over unsaturated conductivity because failure of the Charonnier landslide most likely occurred in (near) saturated conditions (see section

2.2). Previous research indicated conductivities of 0.08 – 8.64 meters per day (Malet et al., 2005).

The conductivity was determined in situ via 22 inverse auger-hole tests. For each test, a hole was made between 0.38 - 100 centimetres deep with an auger. Each obtained conductivity value is an average, related to the size, shape and distribution of pores at the sample location. After draining the profile several times the soil is saturated up to a considerable distance, creating a temporary artificial water table (figure 4.7). The constant infiltration at the bottom and side walls can then be measured via the draw done of the water level. The result will approximate the saturated conductivity for that specific soil profile (Oosterbaan & Nijland, 1986) according to:

$$K = 1.15r\ \frac{\log\left(h_0+\frac{1}{2}r\right)-\log\left(h_t+\frac{1}{2}r\right)}{t-t_0} \qquad (4.3)$$

With K (in meters) being the hydraulic conductivity (m per day), *r* the radius (m), *t* is the time in seconds since start of measuring, the height (m) of the water column and h_0 the h_t value at start of measurement. On average the test lasted over 22 minutes to ensure a constant draw down of the water level. Measurements were recorded every 10 seconds in the first 2 minutes, increasing to every minute when constant drawdown of the water level was observed.

This method is highly sensitive to macro-pores and the depth of the auger hole, making the results often an overestimation (Youngs, 2000). Therefore, not all samples can be used to estimate the saturated conductivity. Only at a (near) constant draw down of the water level is it possible to estimate the saturated conductivity. An increasing rate suggest the rapid infiltration of water to deeper soil layers due to high porosity, often resulting from macro-pores which are common in the Terres Noires layers (Caris & van Asch, 1991). Previous research has already shown that there exists a high variation in K values for these Terres Noires layers, ranging from 5 – 40 cm per day in top layers, sometimes even multiple meters per day. The lowest layer experience conductivity values between 0.1 and 5 cm per day, suggesting that water can accumulate in the top layer (Antoine et al., 1995).

4.3.2.Dry bulk density

It was discussed in section 2.2.2 how bulk density is related to the amount of infiltration and thus potentially to the stability of the slope. It represents the density of soil, including pore space but excluding the mass of water. The analysis of the soil samples can be used to dissect the following elements from the sample: volume of the soil particles and the pore volume which may contain air of water. They reflect the arrangement, size and distribution of particles and pores. The number of pores, or porosity, is discussed in section 4.3.3. Both dry bulk density and porosity give an indication of the soils permeability to water and air. More specific: dry bulk density relates dry mass of a sample to a unit volume the sample occupies; it is thus a useful indicator for compaction. A total of 36 sample rings, with a known volume of 100 cm^3, where hammered into the ground up to 50 centimetres deep. Upon removing the ring from the soil, plastic lids and tape were used to seal of the soil sample. The mass is determined by weighing the sample and the ring, 24 of the 36 samples were then first completely saturated to determine the soil retention curves (see section 4.3.3). After drying the samples in the oven for 24 hours the net difference in sample weight determines the dry weight (M_s) and can be related to dry bulk density(p_b) via the volume of the sample (V) (Campbell & Henshall, 2000):

$$p_b = \frac{M_s}{V} \qquad (4.4)$$

Maquaire et al. (2003) report dry bulk densities between 1.26 and 1.74 grams per cm^3 for the Terres Noires near Barcelonnette.

Another aspect that can be determined from the same data is the amount of water in the soil, the soil water content. This can be either expressed as volumetric water content per known volume or gravimetric water content per mass of dry soil. By taking a sample of a known volume and drying it in the over for at least 24 hours at 105 degrees Celsius will indicate the weight of the water that has been evaporated and the weight of the soil remaining in the sample:

$$\Theta = \frac{w\,\rho_b}{\rho_w} \tag{4.5}$$

Where Θ is the volumetric water content, w the water content, ρ_b the dry bulk density and the density of water (ρ_w) (Gardner et al., 2000). For a known volume, the volumetric water content is thus equal to mass of water over the volume in the sample not occupied by soils.

4.3.3.Soil water retention curve

To quantify the potential amount of water storage in the soil of the Charonnier landslide, the storage capacity or porosity of the landslide must be determined. Porosity is the ratio of pore volume in contrast to the bulk volume. Within a known saturated sample volume, the weight and density of water in sample relates to the porosity. By weighing 24 out of 36 collected samples, at different levels of matric potential the soil retention curve can be constructed. This curve displays the relation between matric potential and the volumetric water content as explained in section 2.2.2. It gives an indication of the size and distribution of pore spaces and is thus affected by texture and structure of the material.

To obtain the soil water retention curve samples are placed in a tank with a layer of sand, fine enough to remain saturated up to the highest suction that is to be measured. The samples are minimally disturbed and situated in steel rings with a diameter of 7.5 cm, closed off by a nylon cloth to retain the soil. The cloth doesn’t prevent water flow as a result from the contact with the sandy transport medium (Topp & Zebchuk, 1979). The tank is connected to an outflow vessel that can be moved in height, relative to the layer of sand in the tank (see figure 4.8). After the samples are weighted, fully saturated for 24 hours and weighted again a negative pressure head is applied. By lowering the outflow vessel relative to the soil samples, an outflow of water or pressure head is produced until a new equilibrium is reached within the tank. This equilibrium value can be recorded gravimetrically by weighing the samples and can be translated to water content (equation 4.3) after the sample has been oven dried. Coarse porosity is then determined from the resulting water retention curve based upon measurements at different pressure heads. The porosity is reached after complete saturation without a pressure head, assuming all pores are filled with water. Previous research has shown that the porosity for Terres Noires region varies between 14 and 36% (Maquaire, 2003).

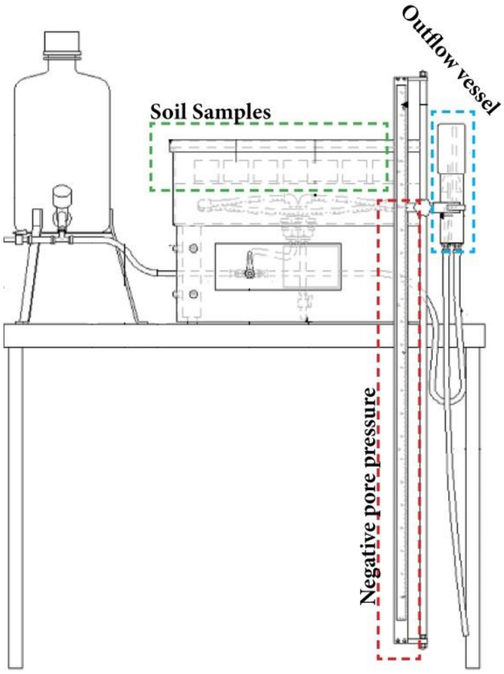

Figure 4.8. Sandbox set-up used to determine the water retention curve of the soil samples (Eijkelkamp instruction manual).

4.4. Strength parameters

As discussed in chapter two the strength of a material refers to the ability of a material to resist deformation, caused by compression, tension or shear stress. Before a material can undergo movement, a force larger than the strain must be induced. Straining forces are for example negative pore water pressure, surface tension, friction and (chemical) bounding, all imposing strength on the material (Embleton & Thornes, 1979). For the stability analysis, it is thus necessary to measure the strength- and stress parameters on 18 collected soil samples. When looking for the strength of soil involved in landslides, the samples should represent the appropriate moisture content and normal stress applied to the slope. The samples were collected below the regolith depth (20 cm) with a shovel to capture the properties of the undisturbed material. Therefore, a small area in the soil was excavated and an undisturbed sample of roughly 10x10x5 cm collected.

A direct shear test was used to apply shear stress along a fictive failure plane (van Genuchten, 1989; Selby, 1993). Resulting in representative values for c' (effective cohesion), τ_f (peak strength) and ϕ' (effective stress) as shown in equation (2.5). This relation between shear strength and normal load can be tested by a direct shear apparatus. Trimmed and saturated soil samples of 60mm by 60mm with a thickness of 20 mm were confined in a shear box (figure 4.9). The box contains two halves that can only move relative to each other. After assembling the undisturbed sample in the shear box, a normal load is applied perpendicular to the sample, a porous stone plate makes sure the stress is evenly distributed and to allow the in- and outflow of water, avoiding the build-up of pore pressure. In the first stage the saturated sample is consolidated for at least 24 hours to a normal loading of 15 kilograms, representing the average loading near the failure surface.

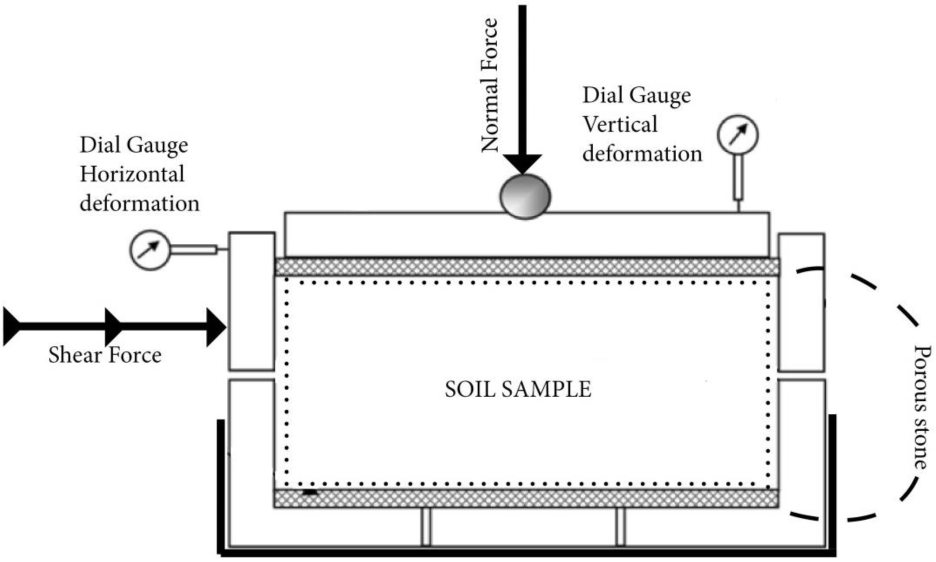

Figure 4.9. Shear Box – concept design of a shear box to measure strength of soil samples (after Selby, 1993).

During the shearing stage, the top half of the sample was sheared with a shearing velocity of 0.2 mm per hour, under a constant load, ultimately causing failure. The normal stress (σ') is then equal to applied normal force (F_z) over the area (A_s) of the sample according to equation (2.1). The applied shear stress (τ) is related to the force as a result of the shearing velocity (e.g. F_x) and the area of the sample (A_s) according to equation (2.2). To avoid the effect of pore pressure on the shear strength results the test are run at very low speeds (0.2 mm/hr) to reduce pore pressure to 0 and making the effective stress equal to the total stress (equation 2.6)

Two dial gages (figure 4.9) record the horizontal and vertical displacement during shearing; these are used to determine F_z and F_x. Vertical deformation is recorded to assess the volume change of the sample during the test. An increase in volume often indicates dense materials that will dilate during shear testing. A decrease in volume often indicates loose materials that will contract during shear testing. The peak in all stress strain curves are the final state stresses and are used to construct strength envelopes. Peaks in shear strength testing are a result of sliding and rolling of particles, causing a volume expansion and build up strength. Residual strengths are related to a denser reorganization of particles causing the sample to contract and giving extra strength to the soil.

An increasing normal load will require more shear stress to cause a sample to fail; the function that describes this relation can be used to construct a failure envelope. The maximum ratios of shear strength (τ’) and effective normal strength (σ’) will be used to construct the Mohr coulomb envelope (section 2.2). This will indicate the combinations of normal stress, shear stresses and the corresponding angle at which failure will occur. The best fit line through these max stress/strain ratios can be used to determine the angle of repose (ϕ') and effective cohesion (c') values via the Mohr-Coulomb failure law (equation 2.5). The angle of repose, or friction angle, indicates the steepest angle at which the material remains stable without being supported by vegetation or negative pore pressure, often between 27° - 33° for Terres Noires (Maquaire, 2003), sometimes up to 35.4° (Antoinne et al., 1995). The effective cohesion is related to the structure of particles and the retention capacity and has an average of 13 kPa for drained direct shear tests (Maquaire, 2003; Antoinne et al., 1995). Soils with higher cohesion are more prone to mass wasting than soils with lower cohesion and higher susceptibility for erosion (Maquaire, 2003).

4.5. Water table

It has been explained in section 2.2.2. how mass movements are related to changes in pore water pressure. Infiltration of rainwater and the resulting groundwater flows are thus important factors to take into consideration. The depth a groundwater table is controlled by rainfall characteristics such as duration, intensity, evapotranspiration and soil moisture distribution (Van Asch et al., 1996). The distribution, or flow, is related to Darcy’s law (equation 2.8) which combines the effect of a gradient and the hydraulic conductivity of a soil to a water flux. In an unsaturated hillslope, a water table determines the flow distribution and incoming and outgoing fluxes of water govern the water table. Assuming flow to be horizontal and uniform in vertical sections, the Dupuit equation (4.6) allows the estimation of discharge (Q) along a hillslope intersection:

$$Q = \frac{K}{2L}(h_0^2 - h_1^2) \tag{4.6}$$

With K being the saturated conductivity, L the length of the slope, h0 and h1 the downslope and upslope initial vertical water table heights respectively. This equation estimates vertical groundwater height along a two-dimensional slope assuming high hydraulic conductivity values and steep slopes (Sidle & Terry, 1992). To generate a groundwater as result of a certain amount of precipitation, critical for a hillslope the equation must be solved for h_1.

$$h_1 = \frac{Q*2l^{\,2}}{K+h_0^2} \tag{4.7}$$

Q is here related to the net precipitation (after interception and evapotranspiration estimated at 50%) that infiltrates into the soil, the width of the transect (1 meter) and the length of the transect (L). Although the water table does not follow a parabolic form, for relative flat slopes it closely predicts the water table (Kasenow, 2001). Extreme recorded precipitation events in October 1993 and 2003, December 1993, 2003 and November 2000 result in some of the highest groundwater tables. The H2 value is an addition of rainfall on top of the unknown initial groundwater table at the top of the landslide in meters. Assuming H1 at 0 meters below the surface, at the base of the slide, to represent complete saturation there.

Table 4.2. Estimated surplus of groundwater table

	P (mm)	Pnet (mm)	H2 (m)
okt-03	230	115	11,6
dec-93	106,9	53	7,9
okt-93	191	96	10,6
nov-00	256	128	12,3
dec-09	150,8	75	9,4
jan-13	153	77	9,5
nov-91	194,5	97	10,7

4.6. Modelling Landslide

Analysis of landslides via, for example remote sensing, has a strong focus on spatial zoning. These techniques, related to risk and susceptibility mapping, have the risk of a bias towards events or specific mass wasting characteristics (van Beek & van Asch, 2004). To avoid this, and include the temporal extent and -variation in local landslide conditions, different types of models can be used to capture the behaviour of individual landslide events based on the relevant parameters for example the analytical models, data driven models and physically based models.

Data driven models consider landslides in a stable state, or in equilibrium along their potential slip surface (Dikau, 1996). As discussed in section 2.3, this is the factor of safety, consisting of the ratio between the sum of opposing factors and the sum of the stress forces (equation 2.9). The sums of both aspects are in general derived from observations and statistical relations. When only the observations are considered, it is generally considered to be a deterministic, when the statistical relations are considered a stochastic factor is included in the model (Scaioni, 2014). For data driven models it remains important to assess the weighting of different parameters, which generally is based on expert judgement (van Beek & van Asch, 2003). Although the subjectivity can be avoided with statistical quantitative weights, a lack of temporal variation remains.

Physically based models attempt to model the behaviour of a landslide once it is destabilised. These models often integrate physical properties, related to mass movement, over a grid that covers the spatial extent of the mass movement (Lu & Godt, 2013; Dikau, 1996; Selby, 1993). An advantage for these physical based models is the objectivity due to the adding of parameters rather than statistically based techniques. The usefulness of such a model remains depended on the chosen parameters, and their ability to represent the land sliding process after calibration and validation (van Beek & van Asch, 2004). If the parameterization is applied successfully, the process based models can quantify the impact from spatial- and temporal changes in the environment on landslide behaviour. Often it is required to couple different types of physical based models with a stability model. This introduces a complicating factor for the model users when parts of the processes are not fully understood (van Beek & van Asch, 2003).

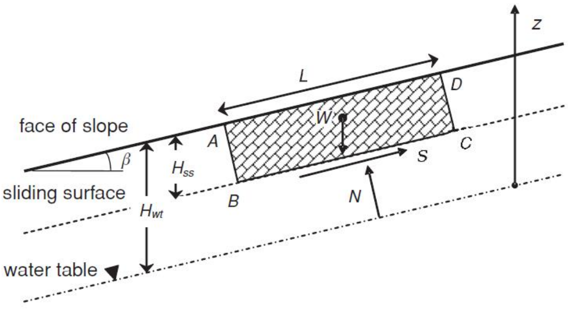

Figure 4.10. Infinite slope model (after Selby, 1993).

Examples of analytical models are the infinite slope model, Swedish method of slicing or Bishop's method of slicing. The infinite slope model is a conceptual, two-dimension model (figure 4.10), often used to illustrate basic translational failure situations (van Beek & van Asch, 2003). The infinite long failure plane is shallow and parallel to the slope, to provide model output with an expected safety factor. Equilibrium conditions related to the forces acting upon the body of mass W can be established (equation 4.8), with γ being the unit weight of the hillslope, L the length of the block, H_{ss} the depth and β the slope angle.

$$W = L\, H_{ss} \cos\beta \tag{4.8}$$

Based on the described equations (2.2), (2.4) and (2.5) it is possible to derive shear strength and stress parameters for the model. The infinite slope model is mainly used to derive range for the failure parameter, where both the contribution of effective cohesion and friction angle, to slope stability, are separately distinguished (Lu & Godt, 2013). Limitations of the infinite slope model are the assumption of infinite dimensions and failure slopes being parallel to the slope. An alternative analytical approach is the method of slicing, which divides the failure slope into several blocks. Iteration over these blocks allows the construction of a factor of safety (Selby, 1993). But both the infinite slope and method of slicing approach assume an average shearing resistance along the slip surface of interest, often estimated from a limited number of samples (Embleton & Thornes, 1979). Bishops method is an extension on the Swedish method of slicing, including slice interaction and thus allowing the differentiation in slice characteristics.

4.6.1. Slip4ex model

Slip4ex (Greenwood, 2006) is a straightforward, analytical, Microsoft Excel based approach that allows to reconstruct landslide dimensions and related parameters, to analyse the slope stability using the method of slices. In the model it is possible to distinguish up to 3 soil layers with their corresponding thickness, angles and soil characteristic. For the Charonnier landslide no distinction is made because the Terres Noires is assumed to be a homogeneous layer. The location and depth of the failure surface are estimated with observations in the field and the DSM. The known locations of the scar near the head of the landslide and the end of the source area are often end points of the failure surface. A known centre of a circle (O) and its corresponding radius (R) allow reconstructing the failure surface below the mass, if the shape of the failure surface is part of this circle (figure 4.11). The radius of the circle determines the curvature of the failure surface, with a lower radius resulting in a more curved shape and a deeper situated failure surface. A higher radius decreases the curvature and thus the depth of the landslide. For each radius value the middle point of the slip circle had to be altered to ensure equal intersects of the failure surface with the terrain model. Assuming one homogeneous soil layer there are no weak interaction layers, the rupture surface will therefore develop because of the forces acting upon it. Then the smallest FoS possible will represent the most likely failure surface, often a spoon shaped plane. The FoS will decrease due to the dependence on the radius of the slip circle. By dividing the surface in slices the total factor of safety can be reconstructed, where each slice contributes to the shear strength according to equation 2.5. This method of slices can be used to characterize the relevant dimensions of individual slices, determine resisting and disturbing forces and estimate a total FoS for the failure surface with equation:

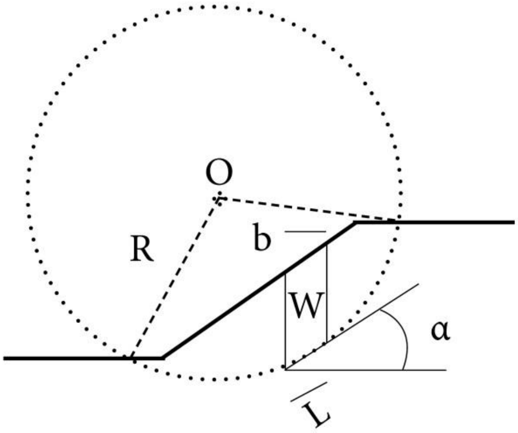

Figure 4.11. Method of slices (after Selby, 1993).

$$FoS = \frac{\sum(c' l + N' \tan\phi')}{\sum W \sin\,\alpha} \tag{4.9}$$

With c' the *effective cohesion*, ϕ' the *effective angle of shear stress*, l the length of the slice of interest at the base, W the weight of the slice, N' all the effective normal forces and α the slope at the slice base. Two methods with different derivatives from this limit equilibrium are used to present the FoS. Swedish method of slices assumes a water surface being parallel to the slip surface and Bishop's method of slices includes inter slice pore water forces (Greenwood, 2006). Other assumptions include an initially completely saturated soil profile, neglecting vertical water transport and soil transmissivity determines the lateral flux that follows the topographic gradient.

It is also possible to include the effect of vegetation on the slope stability (equation 4.9) in the slip4ex model. This is assumed to be negligible for the Charonnier landslide due its failure surface depth of 4 to maximum 10 meters which is common in the region (Malet & Maquaire, 2003), minimizing the effect mechanical support from roots on the failure surface (see section 2.2.3). A groundwater table relative to the surface, because of effective precipitation, can be added to account for the effect of positive pore pressures to the slope stability, as explained in section 2.2.2. A variation in groundwater will be applied to determine the critical slope conditions.

5. Results

The results can be divided in the photogrammetry results: a digital surface model & an orthomosaic, various soil sample results and the stability analysis. The Charonnier can roughly be divided in a source (10209.5 m^2), transport (10402.4 m^2) and deposition area (14306.0 m^2) (figure 5.1), with a total length of 550 meters and a estimated area coverage of 34,918 m^2 (3.49 ha) which is roughly the size of five soccer fields. The distinction between these areas is based on field observations, the orthomosaic and the change in altitude observed in the DTM (figure 5.1). Especially the source area and the deposition area are covered by vegetation, see appendix VII. The transport area is affected by activity from the Charonnier river, such as erosion and sediment transport. The source area can be associated with a slump type of behaviour near the scar, the tongue can be associated with mudslide and creep type of behaviour (see chapter 2.1).

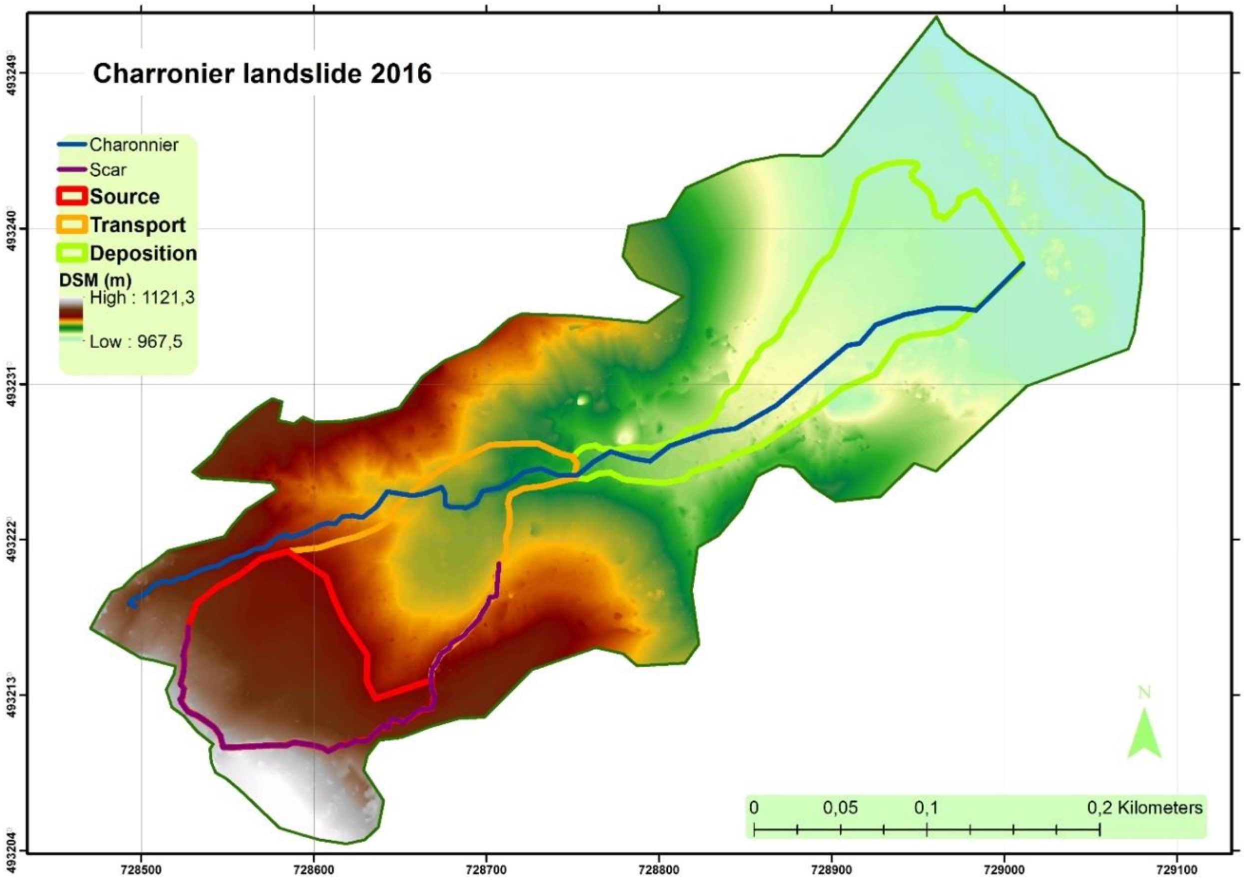

Figure 5.1. Area divided in source, transport and deposition zones, with the DSM in the background.

5.1. Photogrammetry

The photogrammetry results are a Digital Surface Model (DSM) and an orthomosaic of the Charonnier landslide. In total an area of 113.689 m^2 was covered with an average point density of 288 points per m^2. This resulted in a DSM resolution of 0.058 meters per pixel and for the orthomosaic a resolution of 0.029 meters per pixel (appendix VIII).

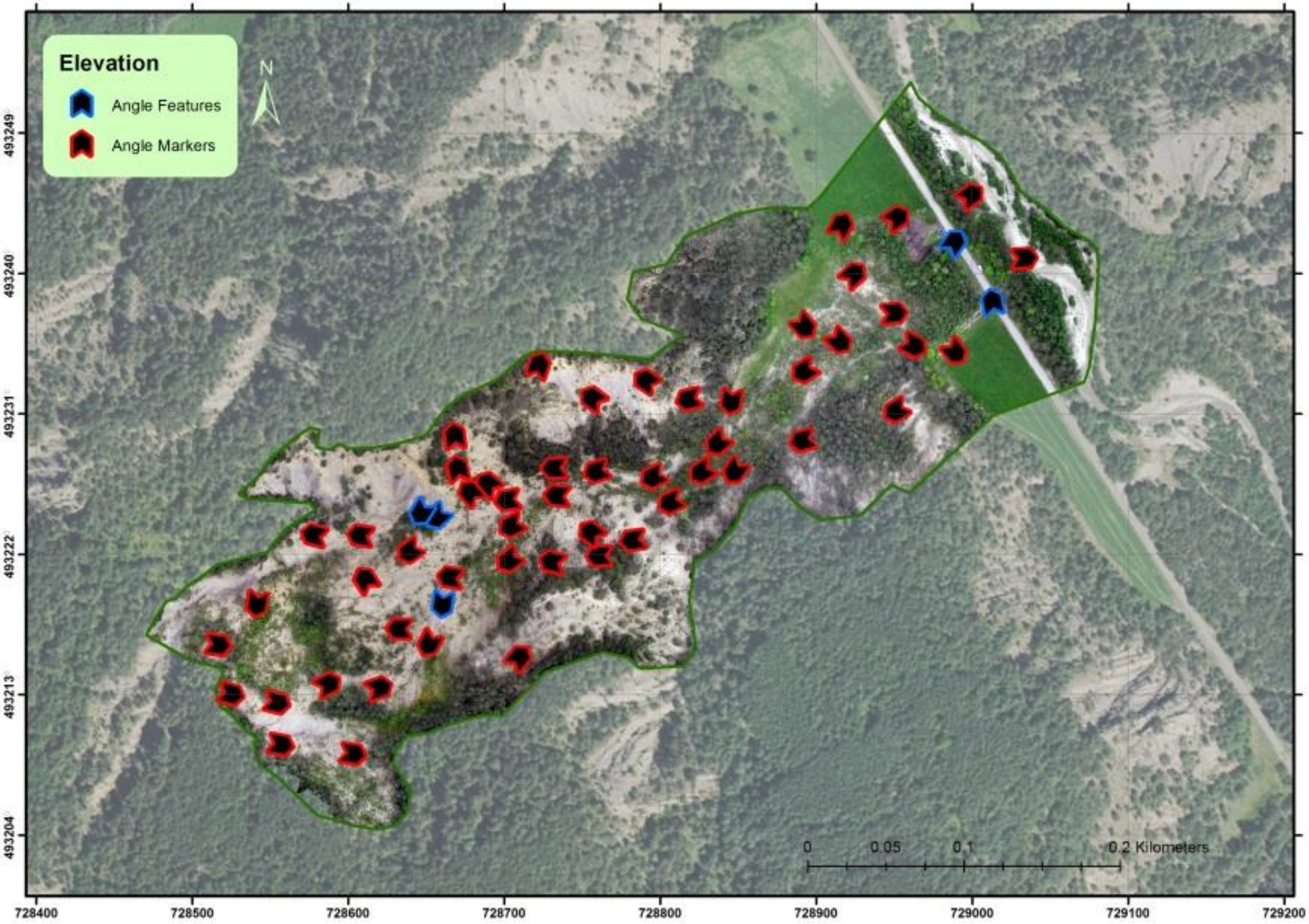

Figure 5.2. Directional error of the markers corresponding to their numerical values, visible in table 5.1.

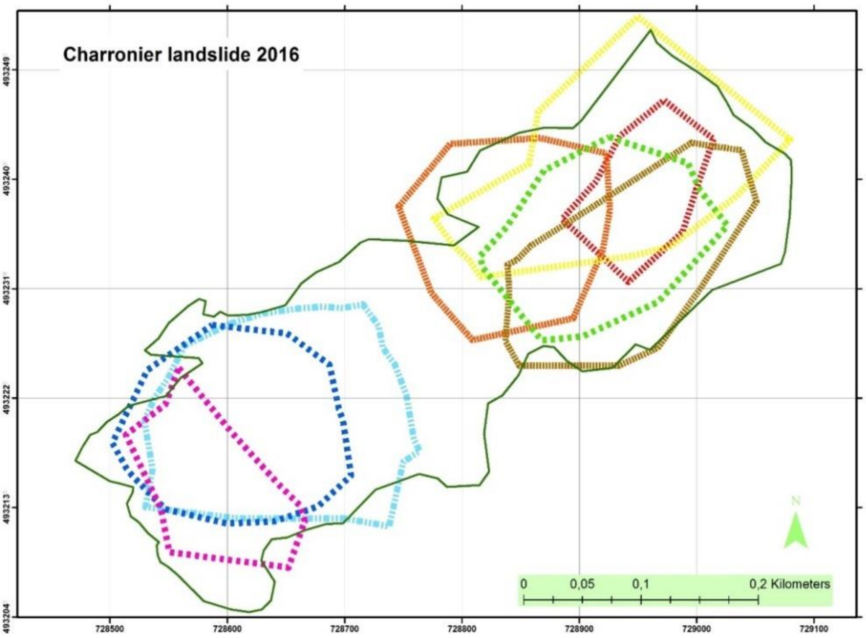

Figure 5.3. Flight areas

The accuracy of the assigned coordinate system was tested with 13 independent ground control points and 5 clearly visible features. The overall accuracy is 7.9 centimetres and 9.5 centimetres in altitude (table 5.1). The direction of the distance between the GCP location in the orthomosaic and the measured coordinates can be visualised with the angle (see section 2.1). As can be seen in figure 5.2, in the centre part of the landslide there are multiple points with an angle between 180 ° and 240° and to the north-west side of the area there are 4 GCP's located in vicinity of each other with an angle between 90° and 110°. Near results are biased in locations, related to areas with insufficient overlap from the different flights. Figure 5.3 gives an overview of the absolute locations of the photos for the 8 successful flights (table 4.1); projection angle of the photograph is not included. The overview suggests that some areas are only photographed from 1 or 2 angles, especially in the middle of the landslide and near the crown of the landslide.

Table 5.1. Positional errors in X, Y and Z direction of the 18 reference points

GCP	ΔX (m)	ΔY (m)	ΔZ (m)	Distance (m)	Angle (°)
1	0.05	0.04	0.10	0.06	35.07
2	0.07	0.01	0.22	0.07	349.61
3	0.10	0.11	0.10	0.15	226.74
4	0.15	0.02	0.18	0.15	187.89
5	0.05	0.03	0.08	0.06	212.43
6	0.09	0.07	0.06	0.12	140.96
7	0.06	0.05	0.09	0.07	139.79
8	0.10	0.01	0.13	0.10	174.64
9	0.09	0.03	0.11	0.09	197.22
10	0.02	0.01	0.11	0.02	193.52
11	0.02	0.01	0.05	0.03	213.08
12	0.16	0.03	0.04	0.16	170.32
13	0.06	0.04	0.08	0.07	212.02
14	0.07	0.01	0.03	0.07	170.85
15	0.02	0.01	0.11	0.02	332.78
16	0.02	0.02	0.05	0.02	42.90
17	0.03	0.04	0.06	0.05	130.85
18	0.09	0.04	0.11	0.10	205.23
	0.069	**0.0316**	**0.095**	**0.079**	

The absolute height profile of the Charonnier River and the scar (visible in figure 5.1) measured with the differential GPS are compared to altitude values derived from the DSM (figure 5.4). As can be seen in figure 5.5 (a, c & e) the impact of vegetation on the quality of the surface model becomes visible. Points measured in vicinity of trees are clearly affected in the resulting DSM.

The Charonnier river bed, with less coverage by vegetation, shows a near fit 1:1 between the elevation extracted from the derived DSM and the measured altitude (figure 5.5 a). When comparing the measured altitude with the observed altitude of the scar profile, the model fit reduces (figure 5.5 c). The overall fit (R = 0.9934) of the surface model can be seen in figure 5.5 (e). By excluding vegetation points from the texture generation step in the MVS method (see section 4.1.2), a better fit for all points (R = 0.9992) can be achieved in the resulting terrain model (DTM). In the constructed hill shade models for both the DSM and DTM, the difference can be observed between the final elevation models (figure 5.5 g&h). It should be noted that the altitude comparison is not based on marked positions in the orthomosaic but the measured altitude is compared with the derived altitude at the given location in the orthomosaic. This implies that the altitude comparison can be subjected to small offset in X or Y direction as a result from the accuracy error.

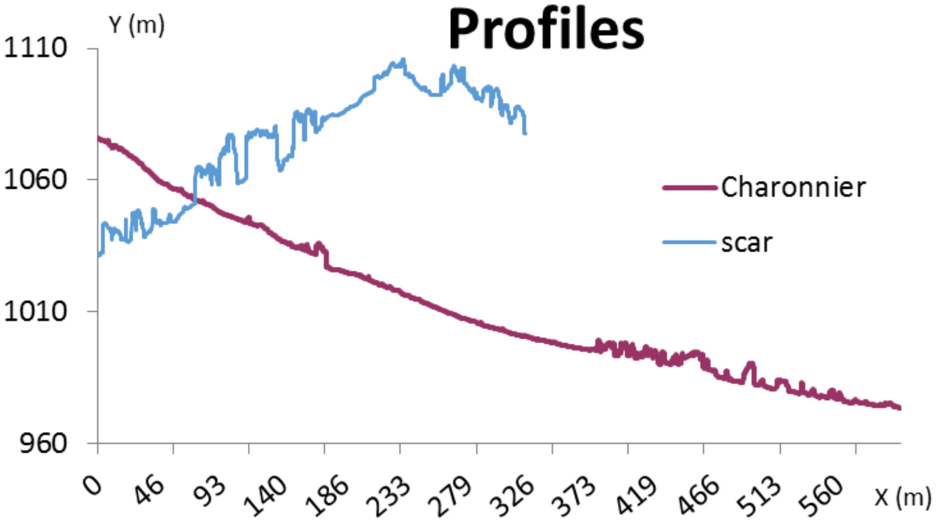

Figure 5.4. Altitude profiles Charonnier and scar as measured from the derived DSM.

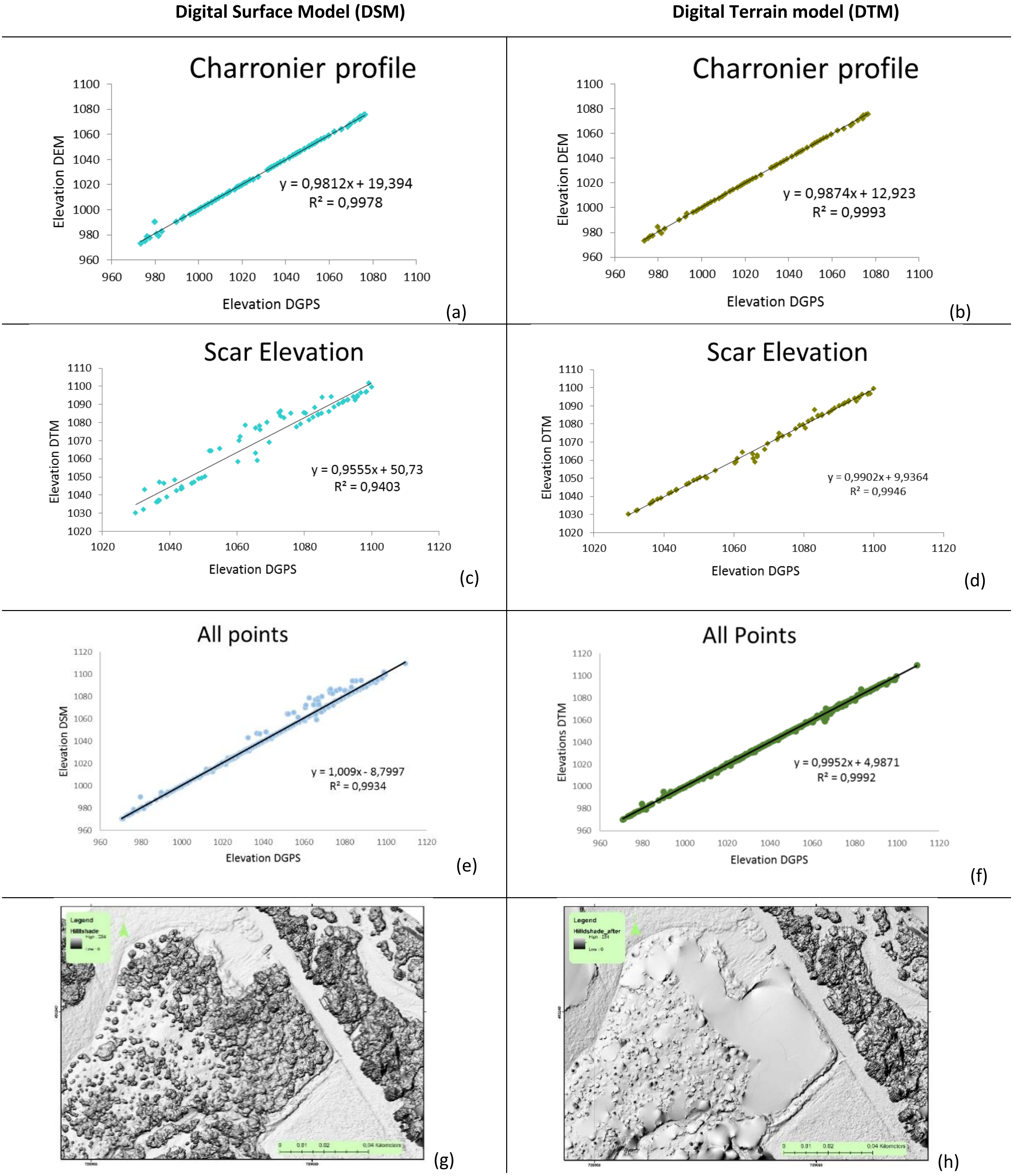

Figure 5.5. Relative model comparison between terrain (DTM) and surface model (DSM).

5.2. Precipitation analysis

Figure 5.6 shows the average monthly precipitation for Tallard (figure 3.2), located approximately 13 kilometres to the south-east of the Charonnier landslide. The temperature is an approximation of the highest and lowest measured temperatures for the period 1960 - 1991. On average the region received 766.75 mm per year between 1986 and 2015, in 1993 this was 907.5 mm (figure 5.6). Landslide activity in the Haute-alps during the winter of 1993-1994 was related to two extreme precipitation events in October 1993 and January 1994. Already saturated soils were exposed to a surplus of water, causing reactivation of mass movements in the Buëch tributaries (Pech & Sevestre, 1994).

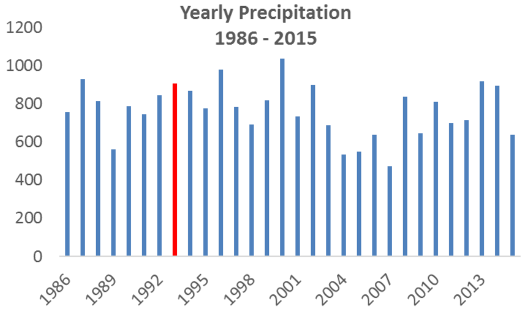

Figure 5.6. Yearly precipitation for the Tallard meteo station.

Figure 5.8 shows why antecedent rainfall analysis for the wettest months is relevant. The amount of precipitation determines the potential soil saturation, before extreme events can cause slope failure to occur (see section 2.2.2). For the period September 1993 – January 1994 a total of 626 mm precipitation was recorded. Even for the wet autumn/winter months this is a significant amount of precipitation, despite November being the second driest recorded. Only in 2000-2001 more precipitation was recorded for the same months (735.9 mm), with “only” 85 mm of rain in December. After a wet December month in 1993 (figure 5.8), a rainfall event of 65 mm on the 6th of January 1994 (figure 5.7) caused the slope to fail.

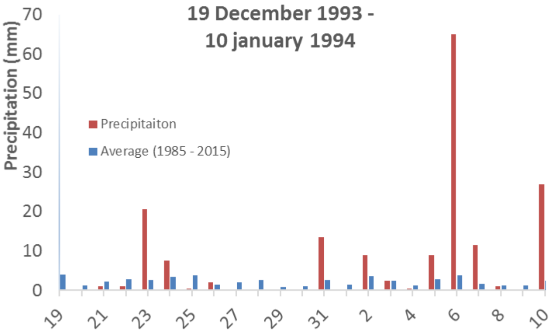

Figure 5.7. Rainfall events in the days leading up to the landslide event on January 4, 1994.

The rainfall characteristics between September and January show an increase in precipitation from halfway of September with intense rainstorms from October onwards (figure 5.8). When looking at the extreme precipitation autumns and winter months in 2000 – 2001 compared to 1993 – 1994 (figure 5.8), there is a difference in timing of excessive rainfall. In 2000-2001 the wettest month was November, whereas December and January were relatively dry. For 1993-1994 the wet period was in October and December. The wettest periods before the landslide event of 1994 are 1987 - 1988 and 1990 – 1991 with a cumulative amount of rain 423 and 391 mm respectively between September and January.

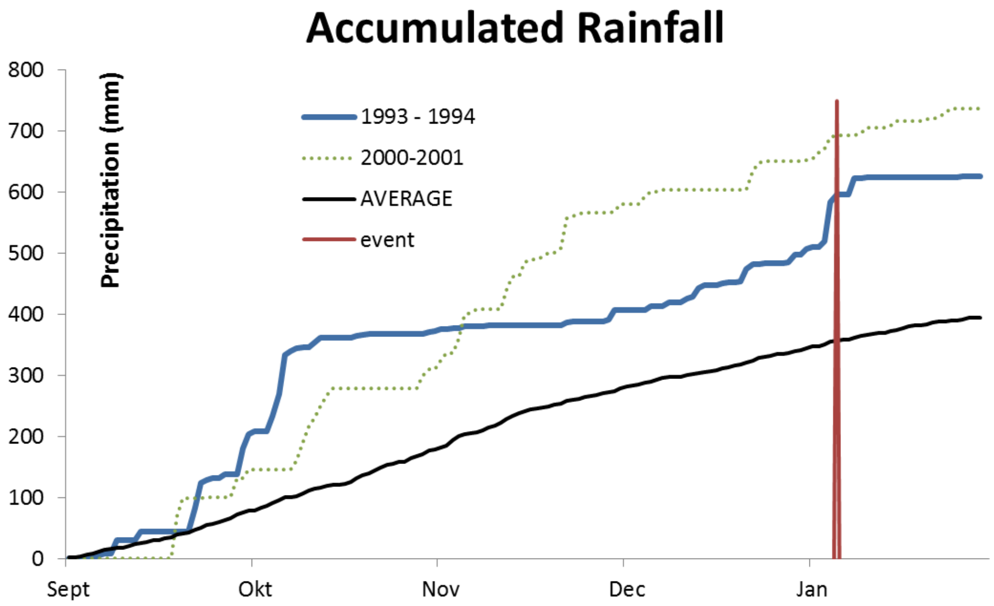

Figure 5.8. Accumulated rainfall for seasons experiencing extreme monthly precipitation in at least one of the October – March months.

Between the 2nd of January and the 8th of January 1994, a total 98.5 mm of antecedent precipitation was recorded, with a peak on the 6th of January of 65 mm precipitation. This peak, according to the corresponding Gumbel distribution, can be related to a return period of 4 years. When looking at the antecedent rainfall the return period for these 6 consecutive rainy days decreases to a return period of 2 years (see figure 5.9). Suggesting that this amount of rain (98.5 mm) spread over multiple days happens more often, than the 65 mm of rain observed on the 6th of January. Between October 5th and 10th, a total of 138.4 mm antecedent precipitation was already recorded, with a peak of 64.1 mm of rain on October 7th. After multiple day rainfall events in November 1997 (T = 11), 1999 (T = 16.5) and 2002 (T = 33) this is the largest cumulative amount of precipitation recorded with an estimated return period of 8.25 years.

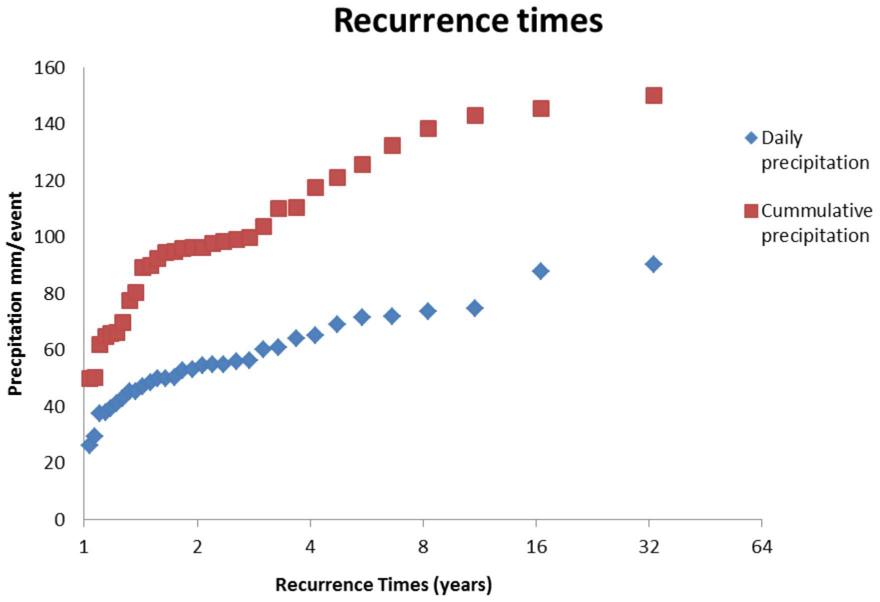

Figure 5.9. Recurrence times for extreme precipitation events

5.3. Soil samples

In total 36 soil samples have been collected of which 24 were used to determine, dry bulk density (DBD), volumetric water content (VMC) and the soil retention curve (SWRC). The remaining twelve were only used to determine the VMC and DBD (table 5.2). Furthermore, a total of 22 auger hole tests were performed, of which only 18 resulted in logical saturated conductivity values. In addition to these soil samples 18 strength samples were collected, in both the parent material and the disturbed landslide material. In total 29 shear stress tests were performed of which 27 were successful. All samples were collected in vicinity of the source area of the landslide (Appendix II). The samples are either collected from source locations, such as the parent materials and the backside of the main slumps, or they are collected from heterogeneous accumulation material. The samples are collected to estimate the storage capacity of the soil; therefore, the following soil characteristics are analysed: porosity, pore size, conductivity and water potential.

Table 5.2. Basic statistics soil characteristics

	Unit	Source material	Accumulated material
DBD (n)		**(18)**	**(18)**
Average	[g * cm^3]	1.52	1.53
STDEV		0.15	0.10
Range		1.19 – 1.74	1.34 – 1.71
VMC (n)		**(18)**	**(18)**
Average	[-]	0.31	0.29
STDEV		0.05	0.06
Porosity (n)		**(6)**	**(18)**
Average	[-]	0.52	0.54
STDEV		0.03	0.03
Range		0.48 – 0.56	0.49 – 0.61
Conductivity (n)		**(10)**	**(12)**
Average	[m^{-1} * d^{-1}]	1.86	3.49
STDEV		2.2	4.2
Range		0.11 – 8.47	0.39 – 12.92
Specific Gravity (n)		**(6)**	**(18)**
Average	[g * cm^3]	3.4	3.31
STDEV		0.10	0.26
Bulk Weight Saturated (n)		**(6)**	**(18)**
Average	[N * cm^3]	21.16	20.28
STDEV		0.89	0.95
Bulk Weight Field capacity (n)		**(6)**	**(18)**
Average	[N * cm^3]	20.31	18.97
STDEV		1.04	1.22

*5.3.1.*Soil characteristics

The dry bulk density is very similar for the source material and accumulated materials, indicating very similar pore spaces in and near the source area of the landslide (table 5.2). There is a linear relation between bulk density and depth. This implies that pore space, and thus storage capacity for water, reduces with increasing depth (figure 5.10).

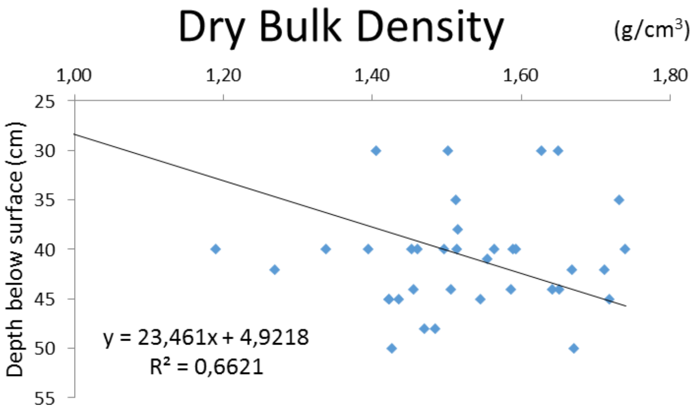

Figure 5.10. Dry bulk density for different depths

To obtain information about the storage capacity of the Terres Noires soils, the VMC was determined (equation 4.5). By normalizing the VMC values of 24 samples a soil retention curve (SWRC) can be plotted with the volumetric moisture content against the applied soil water potential (figure 5.11) and used to determine porosity and field capacity. Field capacity is the amount of soil moisture the soil can hold under gravitational forces. The average field capacity for the area is estimated at 41% (Appendix II) and the porosity at 53% (table 5.1).

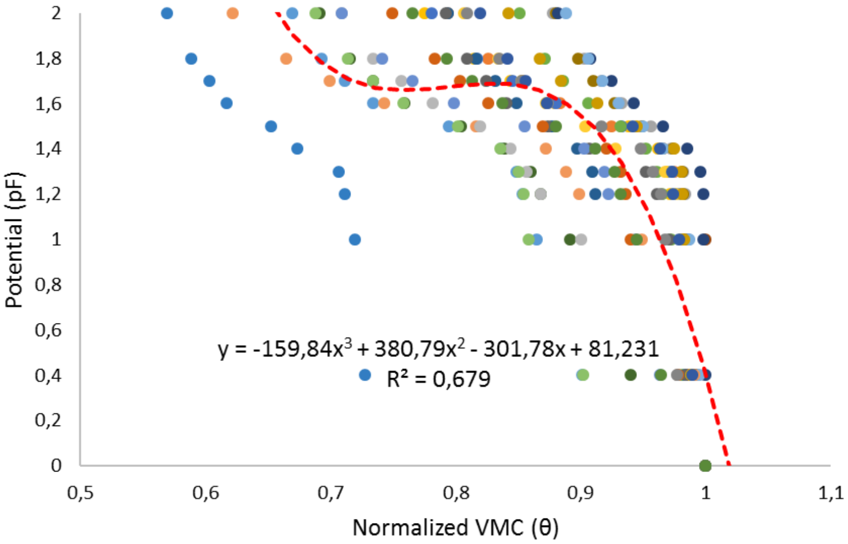

Figure 5.11. Dry bulk density for different depths

The porosity in the accumulated material is slightly higher than for the parent material (table 5.2). The overall relative high porosity determines many properties of the Terres Noires, such as the low strength of the material and high saturated bulk weight.

5.3.2.Saturated conductivity

The accumulated material has a higher saturated conductivity and a wider range of conductivity values. This implies that the transportation or drainage of soil moisture is quicker than in the relatively undisturbed parent material. The relation of saturated conductivity with depth can be constructed when the samples with high and unrealistic conductivity values are excluded. It can be seen from figure 5.12 that the conductivity decreases with depth. This can be related to the increase in DBD with depth (figure 5.10), resulting in smaller pores for water movement at greater depths.

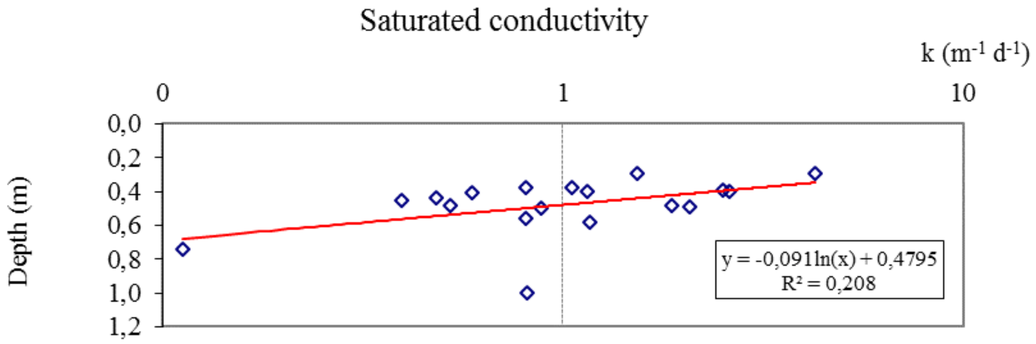

Figure 5.12. Saturated conductivity

5.3.3.Stress – strain relation

As explained in section 2.2.1 the stress-strain curve shows behaviour of the material when it's subjected to an evenly spread normal load and increasing shear force, as is the case with the performed shear strength tests explained in section 4.4. Stress curves for the 29 performed shear strength test show a variety in behaviour over time, when subjected to a shear stress (appendix V and VI). Successful tests can have an increasing shear stress till peak strength then decreasing, ultimately reaching an equilibrium or residual strength, this is often the case with dense material. Loose materials show an equally increasing shear stress over time, also reaching an equilibrium state (figure 5.13). This type of plastic failure can be attributed to compaction and particle reorganization (Maquaire, 2003). Almost all samples are tested for a normal strength ranging from 0.9 to 3.5 kPa per m^2. All successful tests showed a decrease in volume, indicating loose materials.

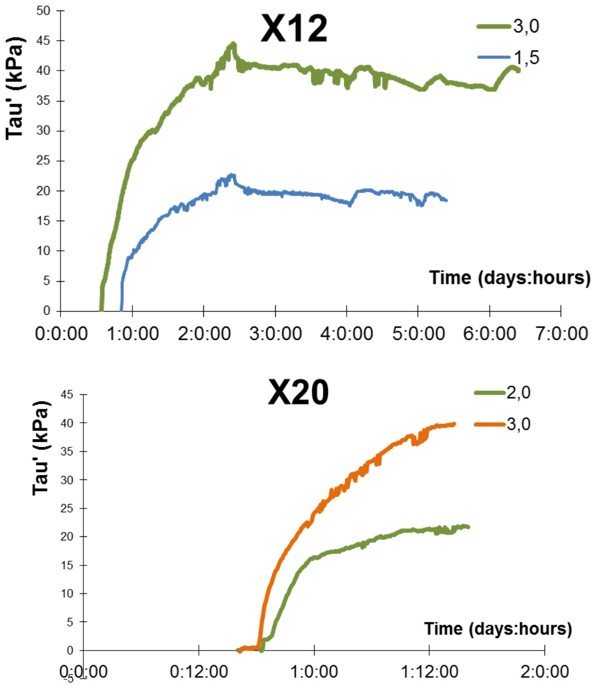

Figure 5.13. Examples of Shear stress over time, with a peak and without a peak.

For each of the individual shear tests the peak shear stresses (τ') are determined with the corresponding normal stresses (σ). The Mohr-Coulomb plot (section 4.4) allows the determination of the friction angle and effective cohesion of the parent and slump material (figure 5.14 and table 5.3).

Table 5.3. Friction angle and Cohesion

	Effective Cohesion (c')	Internal friction angle (ϕ')
Parent material	7.6 kPa	30.2 °
Slump material	6.0 kPa	33.1 °

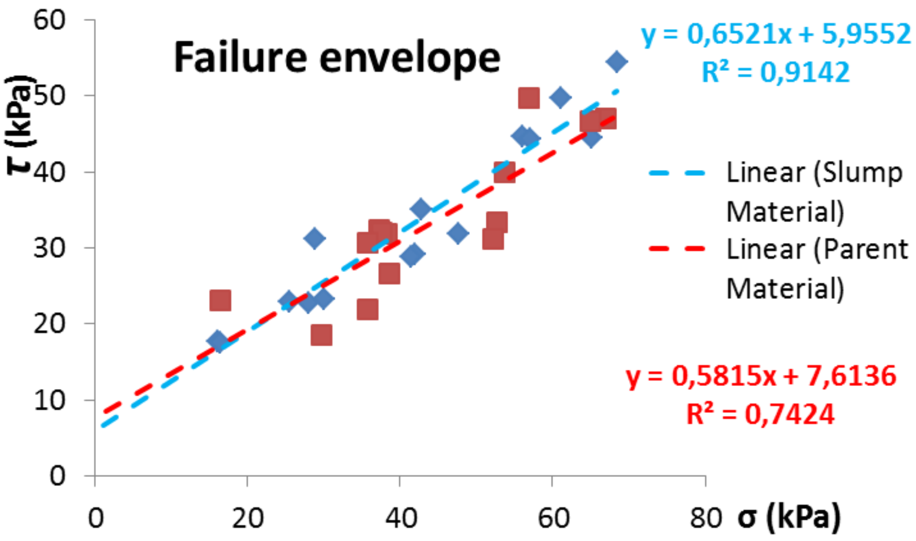

Figure 5.14. Mohr-Coulomb plot for the slump and parent material indicating the friction angles

Slump- and parent material show small differences in effective cohesion and friction angle, determined from the Mohr-Coulomb plot (figure 5.14). Parent material has a higher effective cohesion value and lower friction angle indicating that failure occurs on slopes with a smaller angle compared to slopes in the slump material, assuming the absence of external forces. The parent material has a higher effective cohesion, suggesting a higher retention capacity.

5.4. Stability analysis

As described in section 4.6.1 the slip4ex model (Greenwood, 2006) is used to reconstruct the Charonnier landslide dimension and analyse its stability. The described input parameters (table 5.3) are assigned values that are obtained from the soil sample analysis (section 5.3). The 2D surface dimensions are based on transects derived from the DSM over 250 meters from the same origin (see figure 5.16). This results in 25 slices with an equal width of 10 meters and a varying altitude (see figure 5.15).

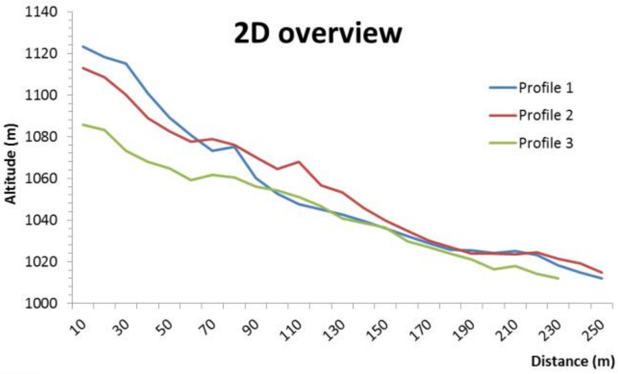

Figure 5.15. 2D display of transects chosen to use as input for the slip4ex model

Based upon the described method in section 4.6.1 the failure surface is estimated by testing different radius values and origin coordinates (Appendix III) to reduce the depth of the rupture surface between 1 – 10 meter below the surface, while maintaining the best estimate location of the rupture surface. For the three transects (figure 5.15) different groundwater levels are then used as input to obtain corresponding critical factors of safety. From figure 5.17 can be seen that transect two obtains a FoS equal to one for different radiuses with a lower groundwater level than transect one and three. At complete saturation (groundwater level is zero meters below surface) transect three still has a factor of safety around 1 for different radius values. For these first test the parent material values from table 5.3 were used as input parameters and the altitude values corresponding to the transects from figure 5.17.

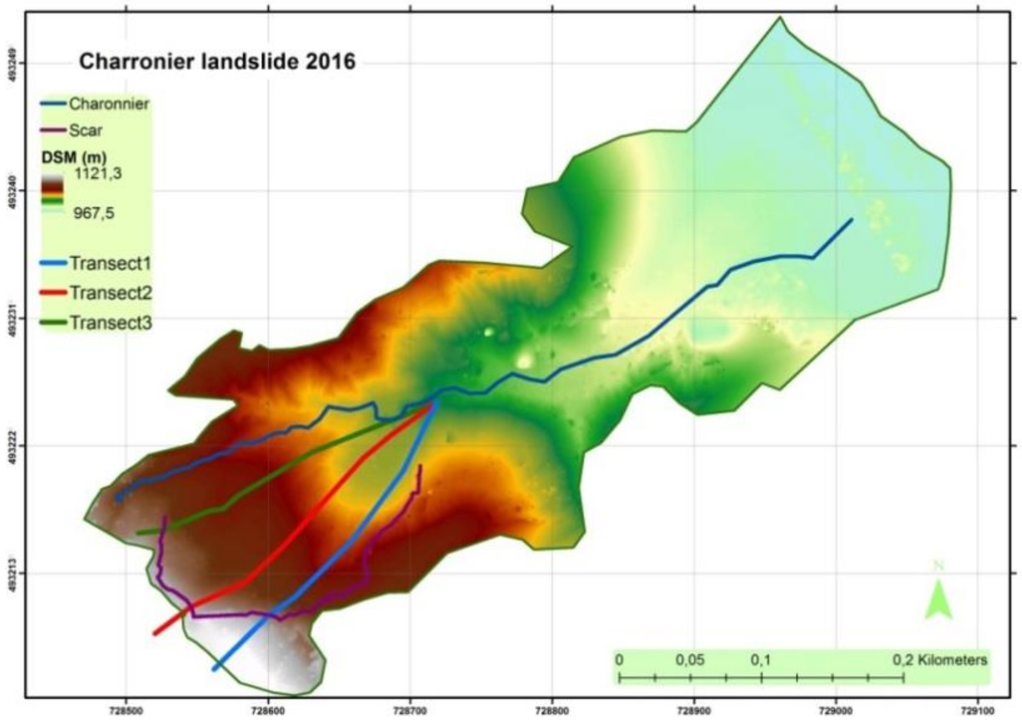

Figure 5.16. Location of the transects used as input for the slip4ex model

It can be seen in figure 5.17 that transect 2 has the most unstable slope, reaching a FoS of 1 with a groundwater depth between 3 and 2 meters. Transect 1 only reaches a FoS of 1 with (almost) complete saturation while transect 3 doesn't fail, even with complete saturation. For the instable part of the landslide, near transect 2, a comparison between the stability with parent material and slump characteristics is made (table5.3). Figure 5.14 shows that the stability improves, for all types of shapes of the rupture surface that are considered in this research, when slump material characteristics are used as input.

The results from figure 5.17 and 5.18 are based on a groundwater table that has a constant depth, relative to the surface. When a varying groundwater level is implemented the development of the FoS, for different groundwater depths, changes. A depth of the groundwater table at the base (h0) of the failure surface of 0 meter (saturated) and a depth of the groundwater table at the head of the landslide (h1) of 30 meters is represented in figure 5.19 (a) as an example. The interpolation of the groundwater table between those two points is non-linear according to the Dupuit equation (4.6), representing an increasing difference between groundwater table and surface further upslope.

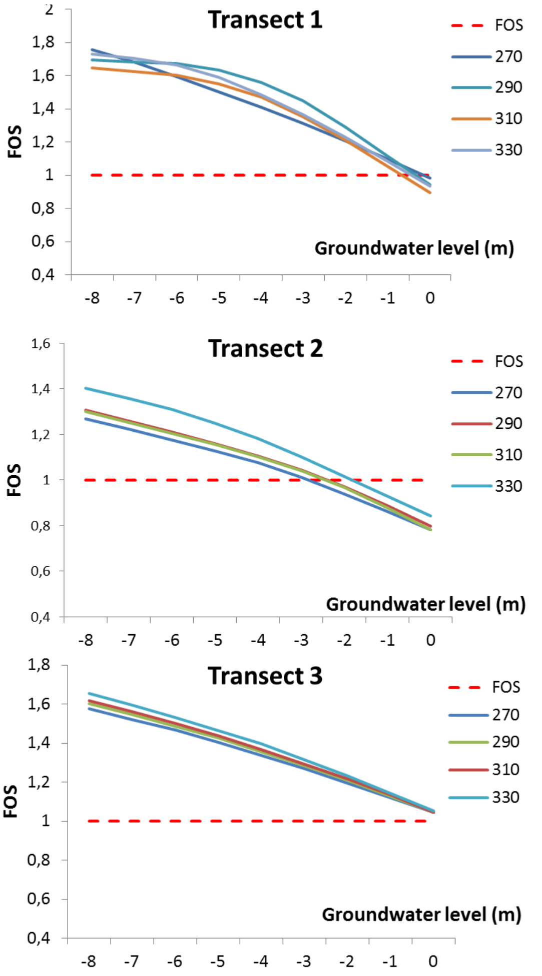

Figure 5.17. FOS for different radiuses, at different groundwater depths ranging from -8 to 0 meters below the surface

Table 5.4. Input parameters for the SLIP4ex model, all derived from the in-situ observations.

SLIP4EX input parameters				
Factor	**Notation**	**Unit**	**Parent material**	**Slump material**
Ambient Bulk weight	Y_{moist}	[kN*m^{-3}]	20.31	19.0
Saturated bulk weight	Y_{sat}	[kN*m^{-3}]	21.16	20.0
Effective cohesion	c'	kPa	7.6	6.0
Angle of internal friction	ϕ'	[°]	30.2	33.1
Saturated conductivity	K	[m^{-1}*day]	1.86	3.5

Figure 5.19 (b) indicates the development of the factor of safety for two radius values for different groundwater depths at the head of the landslide (1). At a saturation of 5 meters at the head and 0 meters at the base of the slide the failure surface with the highest curvature (R=270) fails, with less curvature the surface only fails at a groundwater level of 3 meters at the head of the landslide and 0 meters at the base. When the groundwater level at the base of failure surface is set to 3 meters the development of the FoS for, different H1 values, changes (figure 5.19 c). A FoS below one is only reached for the surface with a radius of 270 meters, when the groundwater at H1 is 3 meters.

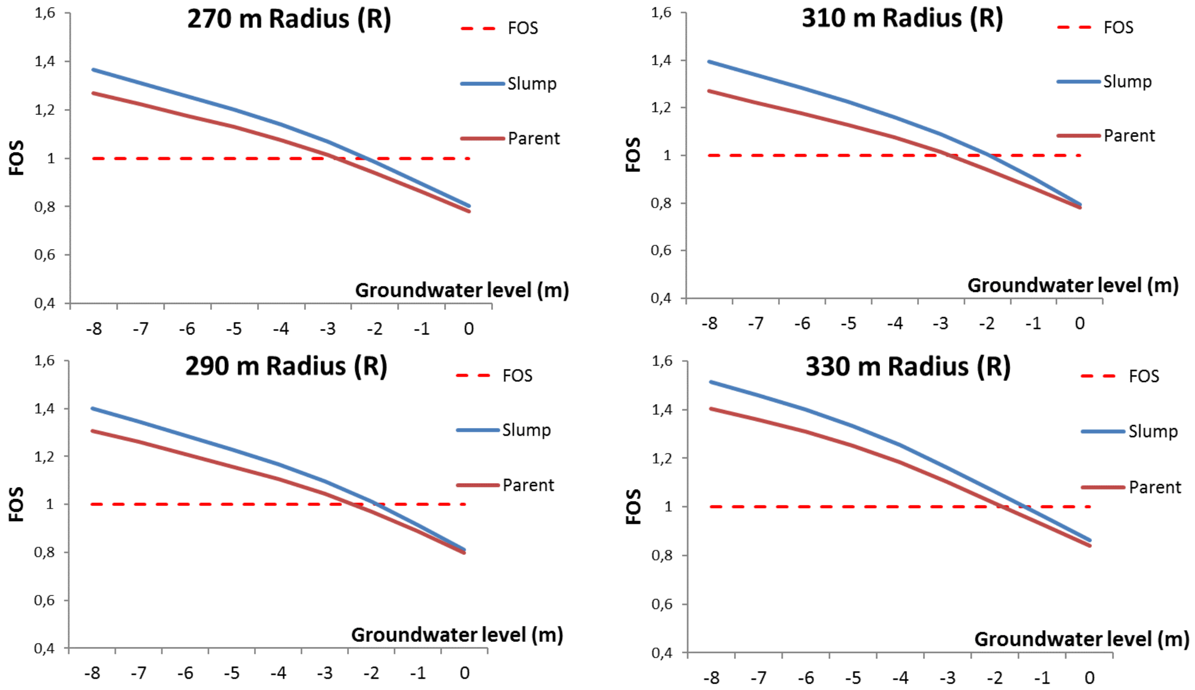

Figure 5.18. Different input parameters, representing slump and parent material, compared for the slope stability at different groundwater levels at the location of transect 2.

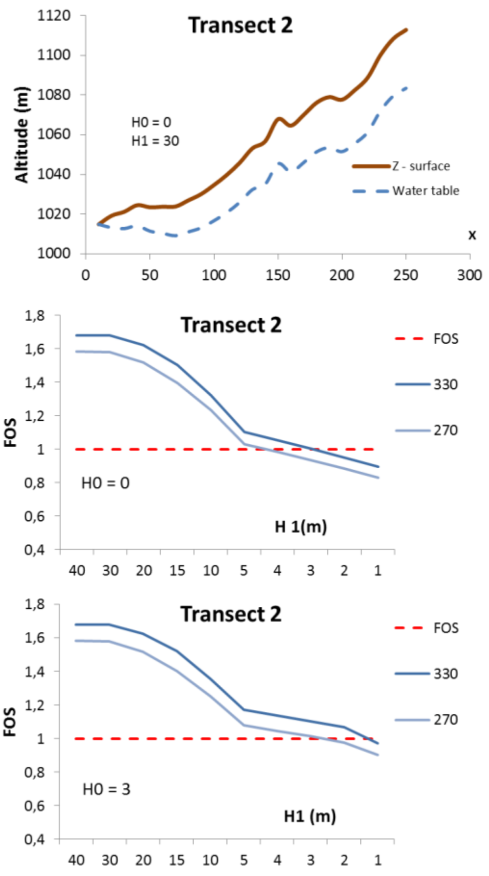

H0 = 0
H1 = 30

(a)

H0 = 0
H1 varies between 40 and 1

(b)

H0 = 3
H1 varies between 40 and 1

(c)

Figure 5.19. FOS for different non-linear groundwater tables applied to transect 2.

5.5. Volume estimation

The better model fit of the DTM (figure 5.5 f) compared to the DSM (figure 5.5 e) allows the estimation of volume displacement in the Charonnier catchment (figure 5.1), since vegetation cover is assumed to be excluded from the DTM. For the estimation involved in the source area the estimation of the rupture surface is used as reference while for the deposition area the original surface, as observed next to the toe is used as reference.

Based on the method described in section 4.1, an estimated volume of 21,102 m^3 displaced soil has accumulated in the disposition zone (or toe) of the landslide (figure 5.1) corresponding to 32,287 tonnes of debris, assuming an average dry bulk density of 1.53 kg per m^3 (table 5.2). The stability analysis described in section 5.4 allows the estimation of the rupture surface depth near the used transects in the analysis. With radius values corresponding to shallow rupture surfaces (R = 330 meter) the resulting depth values were linear interpolated, resulting in an estimation of the rupture surface. The displaced volume, above the current best estimate of the rupture surface is estimated around 100,775 m^3, corresponding to 154,186 tonnes of debris in the source area. The volume of displaced material above the best estimate in the transport area is estimated at 48,738 m^3, corresponding to 74,570 tonnes of debris material. Previous research indicates an average of 300 m^3/ha/year erosion for the Terres Noires (Descroix & Mathys, 2003; Antoine et al., 1995).

6. Discussion

Based upon the presence of slumps, a distinguishable scar and the shape of the mass movement the Charonnier slope failure and its sliding surface can be characterized as a shallow rotational landslide caused by excessive rainfall between October 1993 and January 1994. The movement of the landslide was during the event parallel to the hillslope and confined by the valley slopes of the Charonnier river (figure 5.12). Despite being triggered by excessive rainfall early January, the causes of the landslide are more diverse and related to the material properties of the Terres Noires as will be discussed below.

6.1. UAV campaign

The UAV campaign, between June 3rd and 5th, resulted in an orthomosaic and DSM with 3 and 6-centimetre resolution respectively. Both have a 0.08 horizontal and 0.1 metre vertical accuracy. Despite a bias in the accuracy (figure 5.2), because of insufficient view angles, these results are well suited to document geomorphological surface characteristics. These obtained results, with a consumer graded flying platform and sensor, are within the range of 0.1-meter absolute accuracy achieved by for example Lucieer et al. (2013), or even more accurate than 0.5-meter accuracy reported by (Niethammer et al., 2012). There are results with an accuracy up to 0.025 m (Harwin & Lucieer, 2012), suggesting that, considering the basic equipment, the accuracy is within the expected range. The achieved accuracy and quality can be partially related to the texture and contrast in the captured images. The presence of vegetation and bare ground allow the VMS matching process to yield a high accuracy (Fonstadet al., 2013).

The reported quality and accuracy can be improved towards the 0.025 meter reported by Harwin and Lucieer (2012), by implementing constant and lower altitude flight lines, reducing the amount of flights spread over multiple days, investing in a high end compact camera and the inclusion of internal orientation registration, during capturing of aerial photographs (Lucieer et al., 2013). The registration of internal and external orientation with GPS allows the quantification of the stability of the airplane during the acquisition. With sufficient platform stabilization and constant flying altitude, a higher quality and resolution of the orthomosaic becomes possible, making the interpretation and manual placing of ground control points more accurate (Henry et al, 2002). By including an on-board GPS system flight planning becomes an option, allowing the control of image overlap, flight speed and coverage. Also in areas with large altitude differences, jumps in image scale, because of varying flying altitude, could be avoided with these automatic pilot options, available in recent UAV upgrades. Another improvement is related to the sensor that is attached to the platform (Smith et al., 2015). The sensor is a Canon compact camera set at automated settings. As a result, images are captured in JPEG format without adjustments in ISO and shutter speed. It is recommended to use a sensor with a higher resolution and the possibility to capture pictures in RAW format, allowing post processing of the images. Low ISO and shutter speed reduce the noise and prevent motion blur. All these proposed adjustments result in an improved key point matching between images and visual placement of markers in the images. Despite Agisoft being capable of handling these limitations, the overall quality will benefit, although this has yet to be quantified and reported in the scientific literature.

The analysis used to determine the involved displaced volume is based on an estimated terrain model (DTM). The volume estimation of 100,775 m^3 involved in the landslide event, can only be improved if the pre-event hillslope can be reconstructed with a similar resolution (e.g. Lucieer et al., 2013). This would allow the comparison of altitude over time and thus the displaced volume. The post-event terrain model presented in this research is an estimation, based on the exclusion of vegetation from the texture generation phase in the image processing workflow. The comparison between estimated altitude values and measured altitude values shows that the exclusion results in a better fit of the terrain model; it should be noted that the resulting DTM remains an approximation of the surface. The relative accuracy measurement is also potentially biased, because the location measurements with differential GPS were often located away from forest canopy to ensure sufficient satellite signal to estimate an accurate location. Especially in areas with smaller to no vegetated areas the applied image processing can be an affordable alternative to LIDAR data acquisition. When automated approaches, based on texture or slope differences (Feng et al., 2015) are implemented, UAV based remote sensing can become an alternative used to determine terrain models despite partial vegetation cover.

The difference (circa 79,500 m^3) between the estimated displaced volume (section 5.5) and accumulated volume in the deposition zone cannot fully be explained by a high erosion rate of 300 m^3/ha/year estimated for the Terres Noires (Descroix & Mathys 2003). This suggests that there is an uncertainty in the measurements, related to the exact location and area of the accumulation zone and the estimation of the depth of the original surface. Nevertheless, the displaced volume indicates that the impact of the event is small compared to other mass movements in the Terres Noires or the Alps (Niethammer et al., 2010). To quantify temporal changes at the Charonnier landslide as result of the erosion rate or current slide movement (e.g. creep), a new remote sensing campaign is necessary with at least an orthomosaic and DTM of similar resolution and quality as result. Volume displacement can be used to determine potential creep or erosive properties such as the erosion rate, at the Charonnier landslide.

6.2. Soil properties

Due to the landslide's accessibility it was possible to analyse a wide range of soil properties from collected soil samples. Because sufficient surface water could be collected at the hillslope, inverse auger-hole test were performed. These tests give indications of the saturated conductivity for an undefined mix of horizontal and vertical water flow (Caris & van Asch, 1991). The obtained saturated conductivity values vary strongly between decimetres per day to multiple meters as a result of the wide variety of characteristics that affect the conductivity. Previous research, performed in black marl environments, found similar conductivity values ranging from 0.08 – 8.64 meters per day (Malet et al., 2005). The difference in saturated conductivity for parent material and slump material at the Charonnier landslide cannot be explained by a variation in pore size and bulk density and is therefore most likely a result of the presence of macro-pores, especially in the slump material (Maquaire, 2003). These macro-pores increase the infiltration rate to deeper soil layers and therefore decrease the amount of runoff and infiltration in the top layer. The conductivity observations support the idea that macro-pores provide water flow in top layer of slopes that shows a significant decrease of permeability with depth, favouring the development of a perched water table and lateral flow in the top layer (Caris & van Asch, 1991).

Other soil characteristics such as porosity, moisture content and bulk weight were obtained from undisturbed soil samples collected at a depth varying between 0.28 m and 0.45 m. Despite potential soil disturbance during collection and transport, the resulting values for dry bulk density are comparable to other research focused on the Terres Noires (Maquaire, 2003). With similar average bulk densities, the range for parent material is larger (1.19 – 1.74 g * cm^3) than for accumulated material (1.34 – 1.71 g * cm^3). The presence of small stones in the samples caused some to result in higher bulk density values. Porosity values ranging from 48 % - 61 % are significantly higher than comparable research performed in the Terres Noires by Maquaire (2003), who found values between 14% - 36%. This can be related to the relative low depth at which the soil samples are collected in this research, compared to Maquaire (2003) at 0.5 – 1 metre. The determined saturated soil weight and dry bulk weight are used in the stability analysis, affecting the weight of the soil above and below the water table. A relative high weight for saturated parent material and slump material (21.16 and 20.28 N * cm^3 respectively) was observed. The weight of the soil at field capacity was lower with 20.31 and 18.97 N * cm^3 for parent and slump material respectively. They are within the range of soil weights observed by others (e.g. Maquaire, 2003) and can therefore represent the soil weight in the stability analysis. The soil sample results also support the idea that the storage capacity (and saturated conductivity) of the Terres Noires decreases with depth, resulting in a layer of several meters where water can accumulate after precipitation.

All derived soil properties and saturated conductivity represent the soil characteristics during the field campaign and do therefore not include the temporal- and spatial fluctuation that these factors experience. Time fluctuations related to daily, seasonal, or global shifts or a difference in location properties, such as depth or altitude, all determine the observed characteristics of the soil. Especially in relative shallow soils the response of, for example soil moisture content to wet or dry events, cause a redistribution of water (Van Asch et al., 1999). It is therefore not possible to extent this research to a larger scale or longer temporal frame and compare the results one on one to research performed by others (e.g. Maquaire, 2003)

6.3. Stability analysis

The strength of the parent- and slump material is derived from 29 shear strength tests, performed on 15 soil samples. The results indicate an effective cohesion of 6° for the disturbed slump material and 7.6° for the undisturbed parent material, suggesting a higher retention capacity in the parent material (Maquaire, 2003). The internal fraction for parent material is 30.2° and for slump material a little higher at 33.0°, giving the slump materials a higher internal strength. This can be attributed to the progressive regain of strength Terres Noires show in the long term as a result of the alteration of the clay material (Maquaire, 2003), even after landslide events. Long term changes processes can therefore affect the internal angle and cohesion value and thus the stability of the slope. The results of the Mohr-Coulomb failure envelope should be interpreted with care, the stress and strength properties are more complex than such a test can suggests (Embleton & Thornes, 1979). During the test there is for example no control over drainage, such that pore pressure cannot be measured and has to be assumed zero due to very low displacement speeds (Van Asch et al., 2007). Another assumption is related to the dimensions of the shear plane. During a shear test the failure plane is pre-determined parallel to the movement, which might not be the case in the field (Gan et al., 1988). Another consideration must be made about the desired quality of the soil samples. They should be undisturbed and the collected depth, at max 30 cm, might not always be sufficient to model the peak strength of an intact hillslope (Selby, 1993).

The hillslope stability is sensitive for the shape and depth of the failure surface (Antoine et al., 1995). Curved and deep (> 10 meters) failure surfaces are less realistic for the Charonnier landslide; they cause failure with relative deep groundwater levels (figure 5.18). Despite being an estimation based on geomorphological observations, the relative shallow failure surface (4 – 10 meter) seems most likely, with a top layer (1-2 meters) characterized by high saturated conductivity (Antoine et al., 1995; Caris & van Asch, 1991; van Asch & van Steijn, 1991). A minimization of the FOS at different groundwater depths suggest that the location of the failure surface is near transect two (figure 5.17). A groundwater table of 3 – 0 meters below and parallel to surface is required to cause failure for failure surfaces at every depth and varying curvature. Research has shown that complete saturation of soils in the Terres Noires is very unlikely to have happened in the past 30 years (van Asch et al., 1996). The stability of the slump material is also compared to the stability of the slope with parent material characteristics (figure 5.18). From these results, it can be obtained that parent material of the Charonnier is less stable than the slump material, suggesting that the stability since the landslide in 1994 has been improved, because of above described regain of strength (Maquaire, 2003). It explains partially why extreme rainfall in 1996 – 1997, 2000-2001 and 2003 – 2004 didn't cause a noticeable reactivation of the Charonnier landslide.

The analytical analysis of the water table is in line with the previously determined relation between depth of water table and the slope stability (Terlien, 1998). A saturated slip surface causes a reduction in cohesion which can result in a critical ground water depth, depending on the internal slope angle. Deeper landslides are therefore often triggered by larger amounts of water as a result from for examples multiple day (even week) events or high intensity rainfall events (Van Asch et al., 1999). This can be observed in figure 5.18 where a high curvature (R = 330 meter) results in a FoS below 1 at a groundwater level of 1 meter below the surface. A lower curvature (R = 270 meter), and thus a flatter sliding surface, already causes failure at a groundwater level of 3 meters below the surface. By implementing a more realistic groundwater surface, non-linear to the sloped surface of the landslide, resulted in an even higher stability of the Charonnier landslide. Suggesting that near the location of transect two, a groundwater level is necessary of at least 3 but more likely 1 meter below the surface to cause instability (figure 5.19).

Response of the groundwater table to excessive rainfall, such as in 1993 – 1994, can be localized because of the presence of macro-pores. Positive pore pressures at shallow failure surfaces can often only be achieved by water flowing from the top soil through fissures into the sliding surface. Shallow landslides are therefore not uncommon in the notorious Terres Noires. Another example of the localized reaction to changes in the safety factor comes from the (lack of) response of the Charonnier landslide to other extreme rainfall events (1996-1997 and 2000-2001) that came after the 1993-1994 rainfall events. Due to the stable state of the hillslope after the 1993-1994 event, these rainfall events probably resulted in overland flow and consequent erosion and the formation of Badlands rather than reactivation of the landslide. These observations show that failure is related to long term rainfall and low evapotranspiration, rather than short extreme events because most of the water rapidly moves laterally down slope in the subsurface or a buffering system related to macro-pores (van Asch & van Steijn, 1991). In long term wet conditions there is sufficient vertical drainage, due to these macro-pores, which can cause instability because of a perched groundwater table (Caris & van Asch, 1991; van Asch et al., 1996). The question remains why other extreme rainfall events before the autumn of 1993-1994 (e.g. 374 mm between October 1987 – January 1988) or even the extreme rainfall in October 1993 didn't cause sufficient high pore pressure near the slip surface. Assuming that potential past failures before 1994, are not concealed by the mass movement in January 1994. Extremely low evapotranspiration between December and January, in combination with sufficient accumulation of rainfall in the groundwater body through fissure systems were most likely required. Because December 1993 is not the wettest month recorded, a temperature analysis could improve the rarity of such a combination of extremely low evapotranspiration and high antecedent rainfall.

The use of the analytical SLIP4EX model is justified when it is assumed that the water flow during an antecedent precipitation event is mainly in the vertical direction in the top layers of the hillslope. As a result, the stress is only expressed in two directional principles: horizontal and vertical. The lack of the third principal stress direction makes the resulting factors of safety often a conservative estimation. Even when interaction between slices is included with Bishops method (Greenwood, 2006). The results show that a high groundwater table is necessary to reactivate slope activity because of increasing pore water pressure. It has been suggested that the presence of a perched water table is likely in the Terres Noires after long periods of rainfall, caused by a decrease in saturated conductivity with depth (Maquaire, 2003; Caris & van Asch, 1991). In such a case a smaller amount of rainfall is necessary to result in a critical situation because more water flows in to the lower layers due to the presence of macro-pores (van Asch et al., 1996).

During the analytical stability analysis, the Terres Noires was assumed to be a homogeneous material. Previous research has shown that the material can be described as a homogeneous material along a vertical profile. But observation in conductivity and bulk density indicate a relation with depth, suggesting that this is not the case (van Asch et al., 1999).

7. Conclusion

This research aimed to test how UAV remote sensing outputs can be combined with more conventional research methods to capture the stability of the Charonnier Landslide and it complex causes and triggering mechanisms. Research questions where formulated in order to explore the contribution of UAV remote sensing to stability analysis.

The Charonnier mass movement is an intricate process with diversity in causes, relevant processes and resulting movement types. The high amount of precipitation in the winter of 1993 – 1994, causing a rising water table that ultimately resulted in positive pore pressures, is recognized as the trigger for the landslide. How infiltration occurs, via the soil or via the macro-pores, determines if the failure was caused by a single extreme event or antecedent rainfall. The rainfall pattern suggests that infiltration after extreme wet period between September 1993 and December 1993 with a precipitation of 626 mm created a perched water table that caused increased infiltration rates via macro pores in the wet month of December, eventually triggered by a 65-mm precipitation event on January 6th.

7.1. Research questions

A 3 and 6-centimetre resolution, for the orthomosaic and DSM respectively, were created with an 8-cm horizontal and 10 cm vertical accuracy. Suggesting that DSM and orthomosaic can be constructed with the help of UAV remote sensing campaign, even in steep and vegetated areas. Although the current surface had to be estimated, because a pre-event elevation model was not available, the displaced volume could be estimated at 100.755 m^3, an overestimation related to the presence of vegetation. To improve this volume estimation, a reconstruction of the original surface is thus required, allowing the analyses of difference in height, and thus volume. In such a case the presence of vegetation remains challenging, affecting the terrain model. Manual excluding vegetation points from the texture generation analysis proved a practical solution to improve the estimation.

The collected strength samples are suited to estimate the current stability of the Charonnier landslide. A small difference in effective cohesion (7.6 and 6.0 kPa) and internal fraction (30.2° and 33.1°) was found between parent material and the displaced slump material. This can be attributed to the long-term changes in chemical composition of the Terres Noires, improving the strength and stability of the hillslope since the failure in 1994. The reconstruction of the failure plane is based on in situ observations of the estimated entry- and exit point of the failure surface. Different radius values have been applied to minimize the depth below 10 meters, which is common for landslides in the Terres Noires. Ultra-sounding or other below surface measurements are required to improve estimations of the exact location of the failure surface. The stability of the failure plane greatly depends on the fluctuations in the groundwater table, a critical depth of ranges from 3 – 1 meter, depending on the exact curvature and depth.

Extreme precipitation events often result in rapid lateral subsurface flow out of the system, rather than fissure flow into the sliding surface which is the case in extreme antecedent rainfall. But even with antecedent rainfall, the timing of the event determines the landslide reactions. In times of high evapotranspiration and rainfall interception the subsurface cannot be saturated to a critical height. Only long term antecedent rains, filling the topsoil to a sufficient height, can cause enough saturation of the sliding surface to obtain a critical FoS. Since the landslide event in 1994 more intense rainfall events lasting multiple days didn’t cause reactivation of the landslide. It is therefore most likely that the rainfall during October and December 1993 was accompanied by very low evapotranspiration; this can only be supported if daily temperature measurements are known. It is expected that such a temperature analysis will indicate that December and January are the months with sufficiently low temperature to cause landslides in case of above average antecedent rainfalls.

The overall relation between strength and slope instability has been constructed, the stability of the Charonnier landslide can be explained by the 2D representation and analysis in slip4ex model. The response of the safety factor to the amount of saturation is considered the most significant due to the soil characteristics of the Terres Noires. The results suggest that a (near) saturation of the soil profile, or the formation of a perched water table as a result of macro-pores, could potentially reduce the factor of safety below zero. Precipitation events with higher return periods than recorded in the past 30 years are most likely required to result such a groundwater level rise. But to determine the amount of precipitation causing such an increase in groundwater table, the dynamics of the groundwater must be determined. Factors such as vegetation, erosion rate and landslide movement due to creep are not considered in the stability analysis, and can significantly contribute to the current stability of the landslide, suggesting that the FoS might change over time.

Overall it can be concluded that a combination of the presented methods allows the analysis of the current stability of the Charonnier landslide. An integration of UAV remote sensing with in situ observations is well suited for small scale landslide research with limited time and resources. Under time and resources constrains ones' priorities should be the dry bulk density, porosity and saturated conductivity between a depth of 0.2 and 2 meters allowing the estimation of rupture surface location and effect of groundwater table on the current stability via the slip4ex 2D model. The rainfall pattern suggests that the triggering mechanism is related to the changes in water tables. To rule out any other triggering mechanism more details about the response of the groundwater table to precipitation events must be acquired.

7.2. Future research

The here presented results indicate that the combination of UAV remote sensing, in situ observations and stability modelling yield an encouraging first answer and could be the basis for refinement when more effort is invested in data collection during future campaigns. Additional data acquisition could allow an improved event analysis for the Charonnier Landslide. Especially improved hydrology analysis, related to the fluctuations of the groundwater table related to temperature changes, infiltration and surface runoff, could significantly improve the reconstruction of the Charonnier landslide event. For example the response of the groundwater table to precipitation could be a focus in future research and can be analysed with Dupuit formula, which was explored here.

Also, the determination of the rupture surface, with ultra-sounding or deeper surface drills could also contribute to the stability analysis and allow an improved estimation of displaced material during the event. The latter can also be acquired by reconstructing a pre-event DEM, with sufficient resolution, based on for example historical aerial photographs. With classical photogrammetry on aerial photographs from the French geological survey (IGN), this digital surface model can be estimated for the pre-event situation (Fonstad et al., 2013). Stereographic photos will have to be purchased with a known internal and external orientation, before a DTM with sufficient resolution can be achieved. When the rupture surface estimation is improved a detailed analytical analysis, in three dimension models, becomes possible. This can for example provide more detailed information about groundwater fluctuations.

Future research in the image acquisition, processing and analyses steps can be directed to the effect of these steps on the quality of the final output to increase the added value of UAV remote sensing campaigns. For example, the optimum amount of GCP's, the quality of their location measurements, flying with auto-pilot to control sufficient overlap at lower altitudes and higher resolution sensors affects the final output to an unknown extent. A quantification of the effect of these choices on the final output can help projects in the future optimize their resources, depending on required output quality. Other suggested improvements are related to image acquisition, more specifically the implementation of mission planning software, onboard GPS systems, improved sensors and imagery. The resulting improved image quality should make accuracy up 0.025 meters possible.

During these future campaigns a focus could be to analyse the current stability and soil dynamics by making a comparison with 2016 imagery. With sufficient output quality displacement of material, larger than the accuracy could allow ones to differentiate between landslide activity and erosion and sedimentation processes. Attention to improved and automated vegetation masking can also contribute to this differentiation between these relevant (sub-) surface processes. To automate such a process different approaches can be explored as an alternative to expensive LIDAR remote sensing techniques and can be a topic for further study.

8. References

Antoine, P., Giraud, A., Meunier, M., & Van Asch, T. (1995). Geological and geotechnical properties of the “Terres Noires” in southeastern France: weathering, erosion, solid transport and instability. *Engineering Geology*, *40*(3), 223-234.

Campbell, D. J., & Henshall, J. K. (2000). Bulk density. *Soil environmental analysis. Physical methods. Second edition. Marcel Dekker, Inc., New York*, 315-348.

Caris, J. P. T., & Van Asch, T. W. (1991). Geophysical, geotechnical and hydrological investigations of a small landslide in the French Alps. *Engineering Geology*, *31*(3), 249-276.

Clapuy, F., Vanacker, V., & van Oost, K. (2016). Reproducibility of UAV-based earth topography reconstructions based on Structure-from-motion algorithms. *Geomorphology, (260)*, 4-15.

Crozier, M. J., & Glade, T. (2005). Landslide hazard and risk: issues, concepts and approach. *Landslide hazard and risk. Wiley, West Sussex*, 1-40.

Descroix, L., & Gautier, E. (2002). Water erosion in the southern French Alps: climatic and human mechanisms. *Catena*, *50*(1), 53-85.

Descroix, L., & Mathys, N. (2003). Processes, spatio-temporal factors and measurements of current erosion in the French Southern Alps: a review. *Earth Surface Processes and Landforms*, *28*(9), 993-1011.

Descroix, L., Gautierz, E., Besnier, A. L., & Amogu, O. (2005). Sediment budget as evidence of land-use changes. *Sediment Budgets*, *292*, 262.

Dikau, R. (1996). *Landslide recognition: identification, movement, and clauses* (No. 1). Wiley.

Dilley, M. (2005). *Natural disaster hotspots: a global risk analysis* (Vol. 5). World Bank Publications.

Dirksen, C. (2000). Unsaturated hydraulic conductivity. Soil Analysis: Physical Methods, second ed., Marcel Dekker Inc., New York, 183-237.

Embleton, C., & Thornes, J. B. (Eds.). (1979). Processes in geomorphology (Vol. 436). Arnold.

Feng, Q., Liu, J., & Gong, J. (2015). UAV remote sensing for urban vegetation mapping using random forest and texture analysis. *Remote Sensing*, *7*(1), 1074-1094.

Flageollet, J. C., Maquaire, O., Martin, B., & Weber, D. (1999). Landslides and climatic conditions in the Barcelonnette and Vars basins (Southern French Alps, France). *Geomorphology*, *30*(1), 65-78.

Fonstad, M. A., Dietrich, J. T., Courville, B. C., Jensen, J. L., & Carbonneau, P. E. (2013). Topographic structure from motion: a new development in photogrammetric measurement. *Earth Surface Processes and Landforms*, *38*(4), 421-430.

Gan, J. K. M., Fredlund, D. G., & Rahardjo, H. (1988). Determination of the shear strength parameters of an unsaturated soil using the direct shear test. *Canadian Geotechnical Journal*, *25*(3), 500-510.

Gardner, C. M., Robinson, D. A., Blyth, K., & Cooper, J. D. (2000). Soil water content. *Soil analysis: physical methods*, 1-74.

van Genuchten, P. M. B. (1989). *Movement mechanisms and slide velocity variations of landslides in varved clays in the French Alps* (Vol. 98). Koninklijk Nederlandse Aardrijkskundig Genootschap.

Ghestem, M., Sidle, R. C., & Stokes, A. (2011). The influence of plant root systems on subsurface flow: implications for slope stability. *Bioscience*, *61*(11), 869-879.

Greenwood, J. R. (2006). SLIP4EX – A program for routine slope stability analysis to include the effects of vegetation, reinforcement and hydrological changes. *Geotechnical & Geological Engineering*, *24*(3), 449-465.

Harwin, S., & Lucieer, A. (2012). Assessing the accuracy of georeferenced point clouds produced via multi-view stereopsis from unmanned aerial vehicle (UAV) imagery. *Remote Sensing*, *4*(6), 1573-1599.

Haque, U., Blum, P., da Silva, P. F., Andersen, P., Pilz, J., Chalov, S. R. & Lamas, P. C. (2016). Fatal landslides in Europe. *Landslides*, *13*(6), 1545-1554.

Henry, J. B., Malet, J. P., Maquaire, O., & Grussenmeyer, P. (2002). The use of small-format and low-altitude aerial photos for the realization of high-resolution DEMs in mountainous areas: application to the Super-Sauze earthflow (Alpes-de-Haute-Provence, France). *Earth Surface Processes and Landforms*, *27*(12), 1339-1350.

Horton, R. E. (1933). The role of infiltration in the hydrologic cycle, *Transactions of American Geophysical Union*, 14, 446–460.

Kasenow, M. (2001). Applied ground-water hydrology and well hydraulics. Water Resources Publication.

Kappes, M. S., Malet, J. P., Remaître, A., Horton, P., Jaboyedoff, M., & Bell, R. (2011). Assessment of debris-flow susceptibility at medium-scale in the Barcelonnette Basin, France. *Natural Hazards and Earth System Sciences*, *11*(2), 627-641.

Klose, M., Maurischat, P., & Damm, B. (2016). Landslide impacts in Germany: A historical and socioeconomic perspective. *Landslides*, *13*(1), 183-199.

Lillesand, T., Kiefer, R. W., & Chipman, J. (2014). *Remote sensing and image interpretation*. John Wiley & Sons.

Lu, N., & Godt, J. W. (2013). *Hillslope hydrology and stability*. Cambridge University Press.

Lucieer, A., de Jong, S., & Turner, D. (2013). Mapping landslide displacements using Structure from Motion (SfM) and image correlation of multi-temporal UAV photography. *Progress in Physical Geography*, 0309133313515293.

Malamud, B. D., Turcotte, D. L., Guzzetti, F., & Reichenbach, P. (2004). Landslide inventories and their statistical properties. *Earth Surface Processes and Landforms*, *29*(6), 687-711.

Malet, J. P., & Maquaire, O. (2003, May). Black marl earthflows mobility and long-term seasonal dynamic in south-eastern France. In Proc. 1st Int. Conf. on Fast Slope Movements (pp. 333-340).

Malet, J. P., Van Asch, T. W., Van Beek, R., & Maquaire, O. (2005). Forecasting the behaviour of complex landslides with a spatially distributed hydrological model. *Natural Hazards and Earth System Science*, *5*(1), 71-85.

Mathys, N., Brochot, S., Meunier, M., & Richard, D. (2003). Erosion quantification in the small marly experimental catchments of Draix (Alpes de Haute Provence, France). Calibration of the ETC rainfall–runoff–erosion model. *Catena*, *50*(2), 527-548.

Mantovani, F., Soeters, R., & Van Westen, C. J. (1996). Remote sensing techniques for landslide studies and hazard zonation in Europe. *Geomorphology*, *15*(3), 213-225.

Maquaire, O., Malet, J. P., Remaıtre, A., Locat, J., Klotz, S., & Guillon, J. (2003). Instability conditions of marly hillslopes: towards landsliding or gullying? The case of the Barcelonnette Basin, South East France. *Engineering Geology*, *70*(1), 109-130.

Metternicht, G., Hurni, L., & Gogu, R. (2005). Remote sensing of landslides: An analysis of the potential contribution to geo-spatial systems for hazard assessment in mountainous environments. *Remote sensing of Environment*, *98*(2), 284-303.

Moine, M., Puissant, A., & Malet, J. P. (2009). Detection of landslides from aerial and satellite images with a semi-automatic method. Application to the Barcelonnette basin (Alpes-de-Haute-Provence, France). In *Landslide processes-from geomorphologic mapping to dynamic modelling* (pp. 63-68).

Montgomery, D. R., & Dietrich, W. E. (1994). A physically based model for the topographic control on shallow land sliding. *Water resources research*, *30*(4), 1153-1171.

Mora, P., Baldi, P., Casula, G., Fabris, M., Ghirotti, M., Mazzini, E., & Pesci, A. (2003). Global Positioning Systems and digital photogrammetry for the monitoring of mass movements: application to the Ca'di Malta landslide (northern Apennines, Italy). *Engineering Geology*, *68*(1), 103-121.

Niethammer, U., Rothmund, S., James, M. R., Travelletti, J., & Joswig, M. (2010). UAV-based remote sensing of landslides. *International Archives of Photogrammetry, Remote Sensing and Spatial Information Sciences*, *38*(Part 5), 496-501.

Niethammer, U., James, M. R., Rothmund, S., Travelletti, J., & Joswig, M. (2012). UAV-based remote sensing of the Super-Sauze landslide: Evaluation and results. *Engineering Geology*, *128*, 2-11.

Nikolaeva, E., Walter, T. R., Shirzaei, M., & Zschau, J. (2014). Landslide observation and volume estimation in central Georgia based on L-band InSAR. *Natural Hazards and Earth System Sciences*, *14*(3), 675-688.

Olivier, J. M., Carrel, G., Lamouroux, N., Dole-Olivier, M. J., Malard, F., Bravard, J. P., & Amoros, C. (2009). The Rhône river basin. *Rivers of Europe*, 247-295.

Oosterbaan, R. J., & Nijland, H. J. (1986). Determining the saturated hydraulic conductivity.

Parise, M. (2003). Observation of surface features on an active landslide, and implications for understanding its history of movement. *Natural Hazards and Earth System Science*, *3*(6), 569-580.

Parry, R. H. (2004). *Mohr circles, stress paths and geotechnics*. CRC Press.

Pajares, G. (2015). Overview and current status of remote sensing applications based on unmanned aerial vehicles (UAVs). *Photogrammetric Engineering & Remote Sensing*, *81*(4), 281-329.

Pech, P., & Sevestre (1994), A. Les Consequences Financieres de L'episode Pluvieux Dans Le Basin-Versant Du Buëch, 1993-1994. *Mappemonde, 4,* 94.

Razak, K. A., Straatsma, M. W., Van Westen, C. J., Malet, J. P., & De Jong, S. M. (2011). Airborne laser scanning of forested landslides characterization: terrain model quality and visualization. *Geomorphology*, *126*(1), 186-200.

Schlögel, R., Malet, J. P., Reichenbach, P., Remaître, A., & Doubre, C. (2015). Analysis of a landslide multi-date inventory in a complex mountain landscape: the Ubaye valley case study. *Nat. Hazards Earth Syst. Sci*, *15*, 2369-2389.

Scaioni, M., Longoni, L., Melillo, V., & Papini, M. (2014). Remote sensing for landslide investigations: An overview of recent achievements and perspectives. *Remote Sensing*, *6*(10), 9600-9652.

Selby, M. J. (1993). Hillslope materials and processes. *Hillslope materials and processes.* Second edition. Oxford university press.

Sidle, R. C., & Terry, P. K. K. (1992). Shallow landslide analysis in terrain with managed vegetation. IAHS Publ, (209), 289-298.

Simon, A., & Collison, A. J. (2002). Quantifying the mechanical and hydrologic effects of riparian vegetation on streambank stability. *Earth Surface Processes and Landforms*, *27*(5), 527-546.

Smith, M. W., Carrivick, J. L., & Quincey, D. J. (2016). Structure from motion photogrammetry in physical geography. *Progress in Physical Geography*, *40*(2), 247-275.

Snavely, N., Seitz, S. M., & Szeliski, R. (2008). Modelling the world from internet photo collections. *International Journal of Computer Vision*, *80*(2), 189-210.

Terlien, M. T. (1998). The determination of statistical and deterministic hydrological landslide-triggering thresholds. *Environmental geology*, *35*(2-3), 124-130.

Topp, G. C., & Zebchuk, W. (1979). The determination of soil-water desorption curves for soil cores. *Canadian Journal of Soil Science*, *59*(1), 19-26.

Townend, J., Reeve, M. J., & Carter, A. (2000). Water release characteristic. *Soil environmental analysis. Physical methods. 2nd ed. Marcel Dekker, New York*, 95-140.

Turner, D., Lucieer, A., & de Jong, S. M. (2015). Time series analysis of landslide dynamics using an unmanned aerial vehicle (UAV). *Remote Sensing*, *7*(2), 1736-1757.

Van Asch, T. W., Van Beek, L. P. H., & Bogaard, T. A. (2007). Problems in predicting the mobility of slow-moving landslides. *Engineering geology*, *91*(1), 46-55.

Van Asch, T. W., Van Beek, L. P. H., & Bogaard, T. A. (2009). The diversity in hydrological triggering systems of landslides. In *Proceedings of the First Italian Workshop on Landslides* (pp. 8-10).

Van Asch, T. W., Buma, J., & Van Beek, L. P. H. (1999). A view on some hydrological triggering systems in landslides. *Geomorphology*, *30*(1), 25-32.

Van Asch, T. W., Hendriks, M. R., Hessel, R., & Rappange, F. E. (1996). Hydrological triggering conditions of landslides in varved clays in the French Alps. *Engineering Geology*, *42*(4), 239-251.

Van Asch, T. W., & Van Steijn, H. (1991). Temporal patterns of mass movements in the French Alps. Catena, 18(5), 515-527.

Van Beek, L. P. H. (2003). Assessment of the influence of changes in land use and climate on landslide activity in a Mediterranean environment.

Van Beek, L. P. H., & Van Asch, T. W. (2004). Regional assessment of the effects of land-use change on landslide hazard by means of physically based modelling. *Natural Hazards*, *31*(1), 289-304.

Varnes, D. J. (1984). *Landslide hazard zonation: a review of principles and practice* (No. 3).

Wallace, L., Lucieer, A., Malenovský, Z., Turner, D., & Vopěnka, P. (2016). Assessment of forest structure using two UAV techniques: A comparison of airborne laser scanning and structure from motion (SfM) point clouds. *Forests*, *7*(3), 62.

Westoby, M. J., Brasington, J., Glasser, N. F., Hambrey, M. J., & Reynolds, J. M. (2012). 'Structure-from-Motion' photogrammetry: A low-cost, effective tool for geoscience applications. *Geomorphology*, *179*, 300-314.

Wijdenes, D. O., & Ergenzinger, P. (1998). Erosion and sediment transport on steep marly hillslopes, Draix, Haute-Provence, France: an experimental field study. Catena, 33(3), 179-200.

Wu, W., & Sidle, R. C. (1995). A distributed slope stability model for steep forested basins. *Water resources research*, *31*(8), 2097-2110.

Youngs, E. G. (2000). Hydraulic conductivity of saturated soils. *Soil and Environmental Analysis: Physical Methods, Revised, and Expanded*, 141.

Websites
http://www.insee.fr/ visited august 2016.

Figures

2 Theoretical background

2.1 Varnes (1984)
2.2 Varnes (1984)
2.3 After Hoek & Bray, J. D. (1981)
2.4 Embleton & Thornes (1979)
2.5 Malet et al., (2005)
2.6 Selby (1993)

3 Area description

3.1 Insee, 2016
3.2 Aerial photograph IGN
3.3 Meteo France

4 Method

4.1 After Landgrebe (2005).
4.2 After Westoby et al. (2012).
4.3 –
4.4 Aerial photograph IGN (background)
4.5 After Snavely et al., (2008)
4.6 After ESRI (2017)
4.7 Oosterbaan & Nijland (1986)
4.8 After Eijkelkamp instruction manual
4.9 After Selby (1993)
4.10 After Selby (1993)
4.11 After Selby (1993)

5 Results

5.1 –
5.2 Background Aerial photograph IGN
5.3 –
5.4 –
5.5 –
5.6 –
5.7 –
5.8 Meteo France
5.9 –
5.10 –
5.11 –
5.12 –
5.13 –
5.14 –
5.15 –
5.16 –
5.17 –
5.18 –
5.19 –
5.20

9. Appendix

I. Location of soil samples

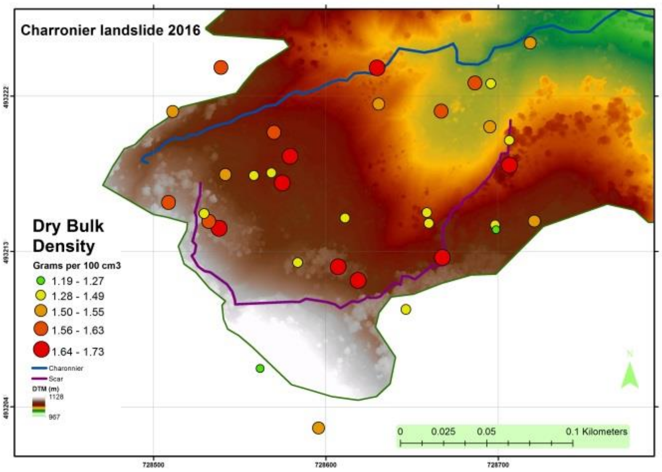

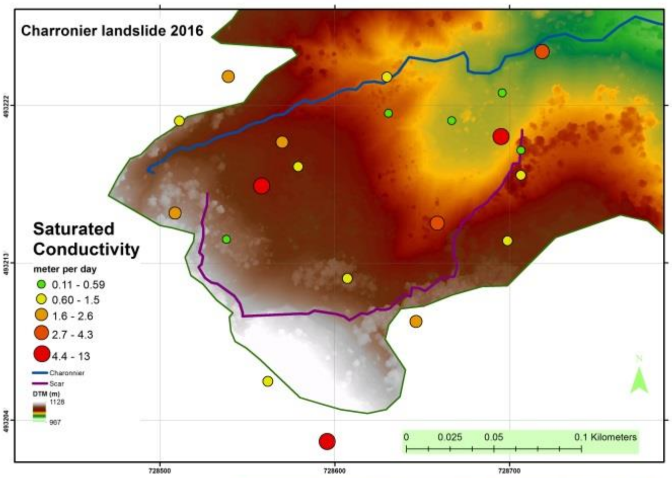

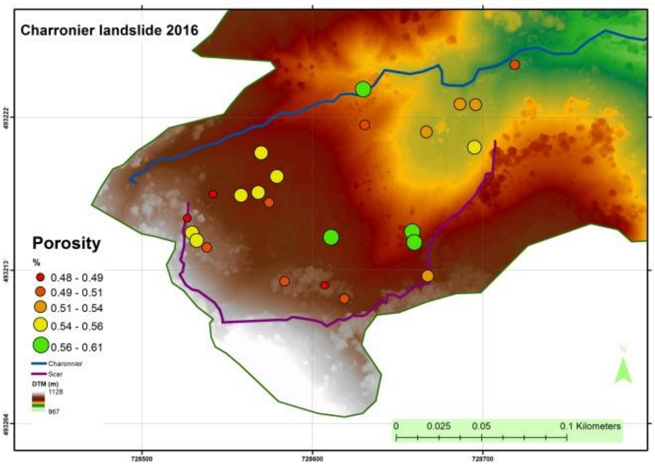

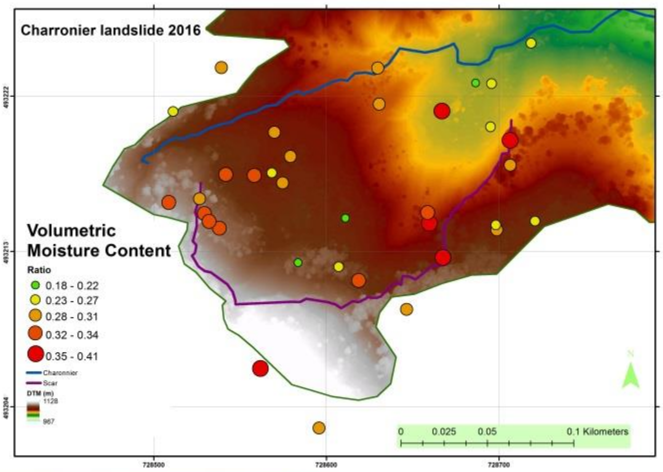

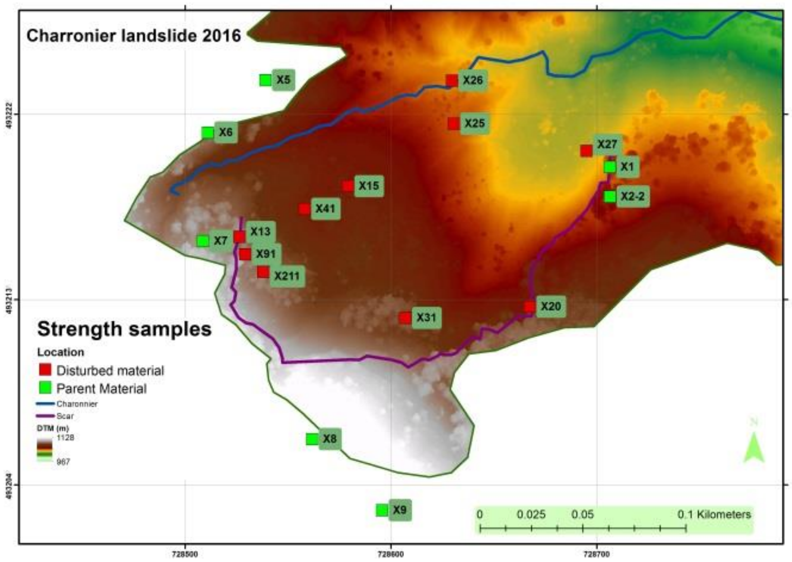

II. Soil samples

GPS coordinates	Class	DBD [g *g^{-1}]	VMC [g *g^{-1}]	Porosity	KSAT [m^{-1} * d^{-1}]	Strength sample	Field Capacity [g *g^{-1}]	Specific gravity [g * cm^{3}]	Saturated Bulk weight [g * cm^{3}]	Bulk Weight at Field capacity [g * cm^{3}]
X71	Accumulated Material	1,64	0,34	0,50	-	-	0,42	3,28	21,02	20,25
X11	Accumulated Material	1,42	0,22	0,51	-	-	0,34	2,90	18,97	17,31
X14	Accumulated Material	1,43	0,25	0,55	-	-	0,43	3,18	19,40	18,19
X15	Accumulated Material	1,67	0,28	0,54	0,81	√	0,42	3,66	21,70	20,54
X41	Accumulated Material	1,46	0,33	0,54	12,92	√	0,44	3,19	19,65	18,63
X16	Accumulated Material	1,50	0,33	0,49	-	-	0,42	2,94	19,51	18,79
X17	Accumulated Material	1,71	0,29	0,50	-	-	0,40	3,41	21,69	20,68
X18	Accumulated Material	1,34	0,20	0,58	-	-	0,36	3,19	18,83	16,71
X19	Accumulated Material	1,42	0,37	0,58	-	-	0,46	3,36	19,62	18,44
X21	Accumulated Material	1,59	0,28	0,54	2,07	-	0,44	3,48	21,35	20,73
X22	Accumulated Material	1,59	0,41	0,52	0,39	-	0,46	3,31	20,68	20,11
X23	Accumulated Material	1,59	0,18	0,54	-	-	0,33	3,43	20,86	18,86
X24	Accumulated Material	1,47	0,33	0,61	3,36	-	0,43	3,75	20,39	18,65
X25(1)	Accumulated Material	1,55	0,30	0,51	0,52	√	0,41	3,17	20,20	19,22
X25 (2)	Accumulated Material	-	-	-	-	√		-	-	-
X26	Accumulated Material	1,65	0,28	0,57	1,17	√	0,40	3,84	21,79	20,17
X27	Accumulated Material	1,51	0,26	0,54	8,82	√	0,37	3,29	20,10	18,44
X28	Accumulated Material	1,46	0,27	0,53	0,59	-	0,30	3,12	19,51	17,25
X29	Accumulated Material	1,52	0,24	0,50	4,27	-	0,37	3,05	19,80	18,54
X1	Source Material	1,45	0,41	-	0,48	√		-	-	-

X2.2	Source Material	1,67	0,29	-	0,88	√		-	-	-
X2.1	Source Material	-	-	-	0,81	-		-	-	-
X3	Source Material	1,51	0,25	-	-	-		-	-	-
X4	Source Material	1,40	0,27	-	-	-		-	-	-
X5	Source Material	1,63	0,30	-	1,87	√		-	-	-
X6	Source Material	1,50	0,25	-	1,15	√		-	-	-
X7	Source Material	1,56	0,34	-	2,52	√		-	-	-
X8.1	Source Material	1,41	0,21	-	-	-		-	-	-
X8.2	Source Material	1,19	0,36	-	1,53	√		-	-	-
X9	Source Material	1,52	0,31	-	8,47	√		-	-	-
X10	Source Material	1,49	0,30	-	2,60	√		-	-	-
X2	Source Material	1,27	0,28	-	1,05	-		-	-	-
X12	Source Material	1,55	0,32	0,56	-	-	0,44	3,50	20,71	19,58
X13	Source Material	1,74	0,29	0,48	-	√	0,42	3,34	21,77	21,19
X91	Source Material	1,44	0,33	0,56	-	-	0,46	3,24	19,55	18,57
X31	Source Material	1,73	0,27	0,49	0,81	√	0,36	3,37	21,76	20,57
X21-1	Source Material	1,72	0,34	0,50	0,11	√	0,37	3,48	21,81	21,22
X20	Source Material	1,65	0,38	0,53	-	√	0,46	3,48	21,35	20,73
	Average	**1,53**	**0,30**	**0,53**	**2,60**		**0,41**	**3,33**	**20,50**	**19,31**

III. Transects used for stability modelling

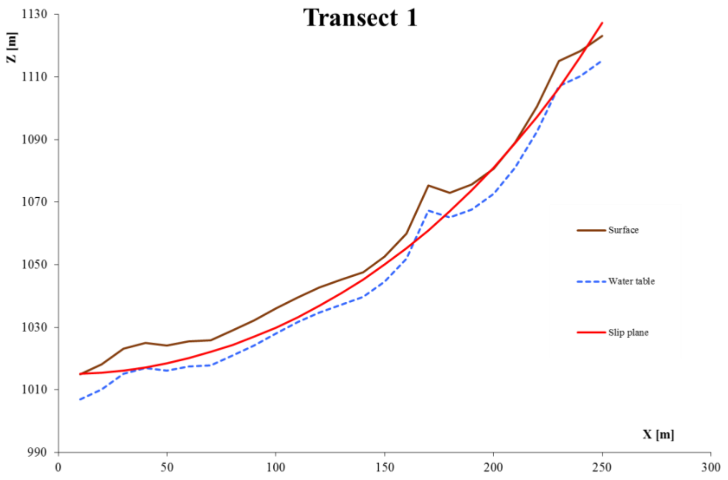

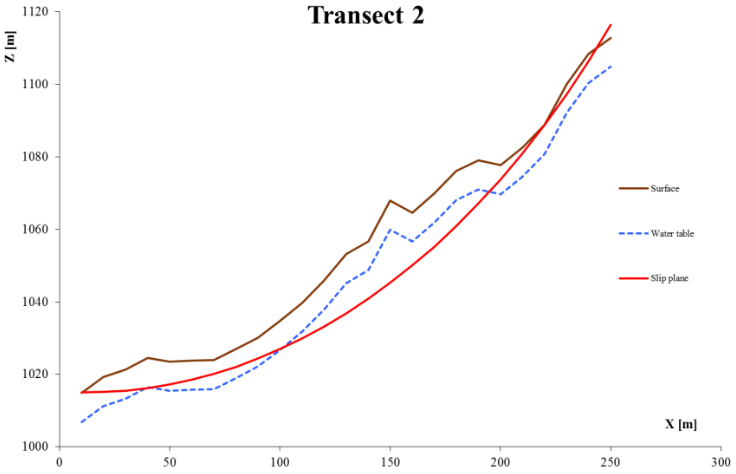

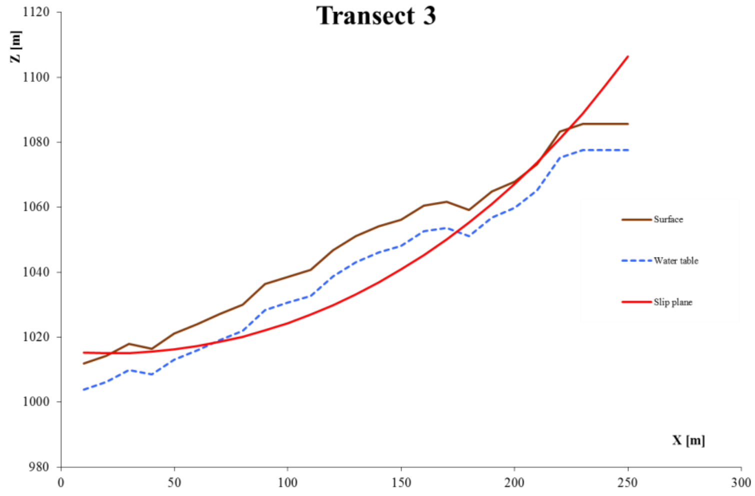

IV. Saturated Conductivity

	Depth (m)	Ksat (m.d-1)	R²	Altitude (m)	Length (sec)	Material
1	0.44	0.48	0.97	999	1500	Parent Material
2	0.29	4.27	0.99	958	1200	Below slumps
3	0.29	1.53	0.84	1087	1500	Parent Material
4	0.38	1.05	0.98	1078	1500	Parent Material
5	0.38	0.81	0.97	1025	1500	Back slump
6	0.39	2.52	0.85	1047	1380	Parent Material
7	0.4	2.60	0.99	1020	1800	Parent Material
8	0.4	1.15	0.98	1037	1500	Parent Material
9	0.41	0.59	1.00	969	1500	Below slumps
10	0.45	0.39	0.99	969	1500	Below slumps
11	0.48	0.52	0.99	986	1500	Below slumps
12	0.48	1.87	1.00	1019	1500	Parent Material
13	0.49	2.07	0.99	1004	1560	Slump
14	0.5	0.88	1.00	992	900	Parent Material
15	0.56	0.81	0.99	1004	1500	Slump
16	0.58	1.17	0.99	992	1500	Below slumps
17	0.74	0.11	0.97	1021	1500	Back slump
18	1	0.81	0.96	992	1800	Parent Material
19	0.41	3.36	0.92	993	1110	Back slump
20	0.38	8.82	1.00	978	710	Below scar
21	0.6	12.92	0.99	998	570	Slump
22	0.46	8.47	1.00	1081	550	Parent Material
Average	**0.48**	**2.60**	**0.97**	**1011**	**1345**	

V. Strength results – Parent material

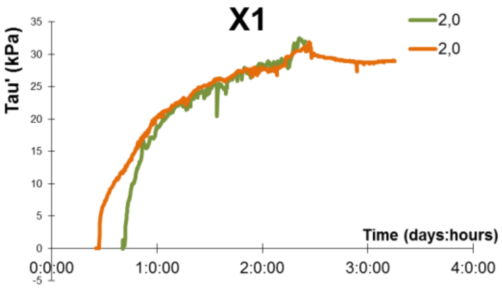

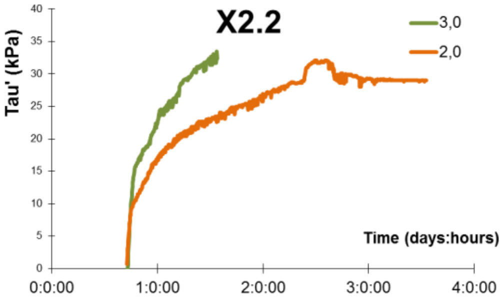

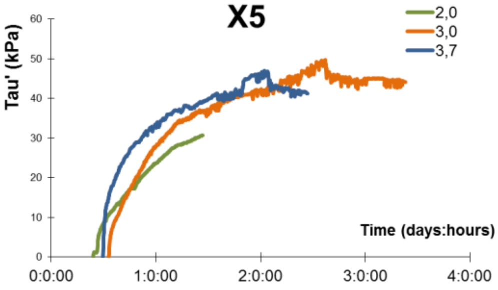

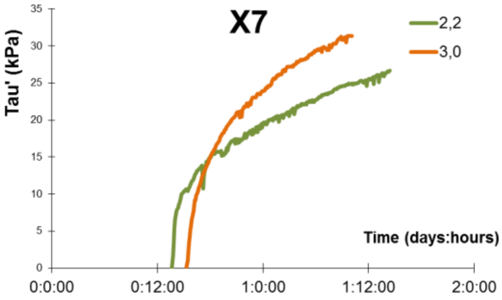

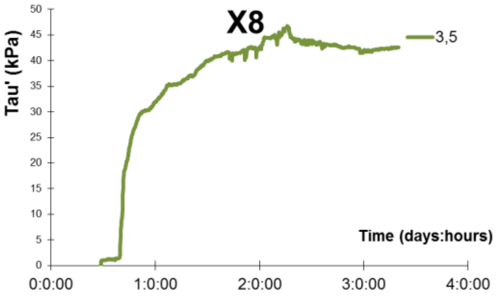

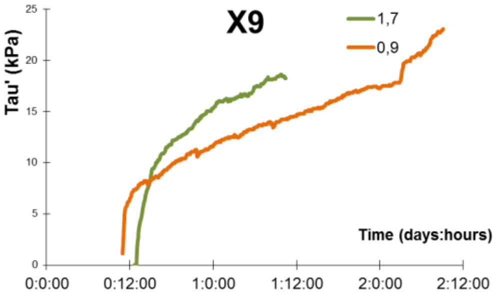

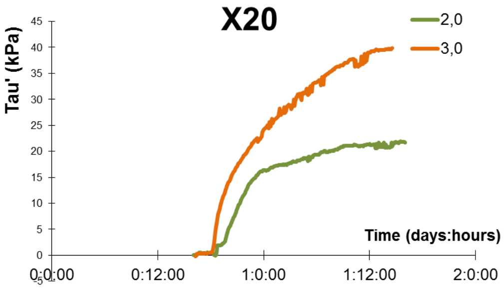

VI. Strength results – Slump material

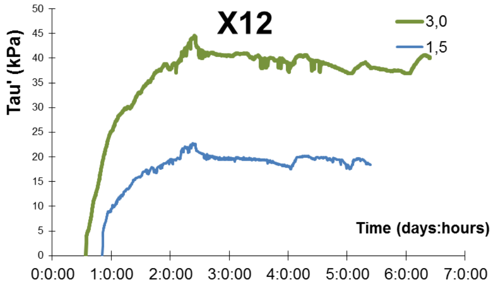

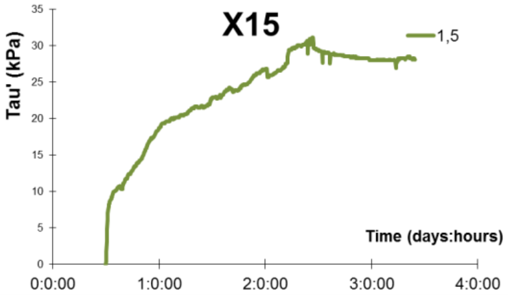

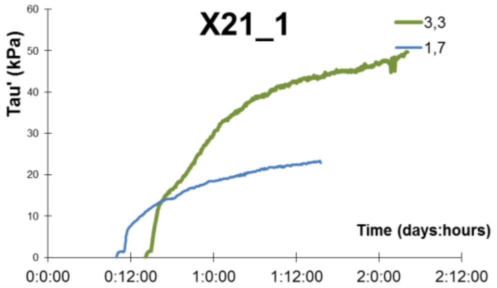

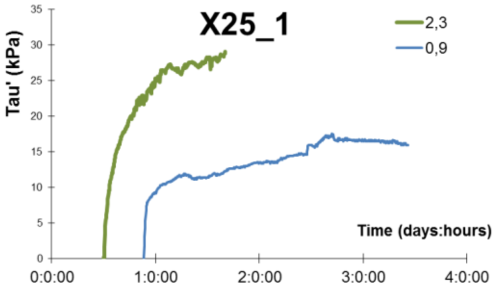

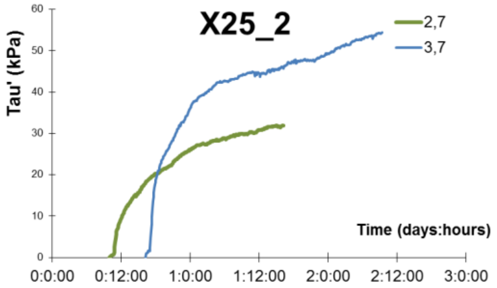

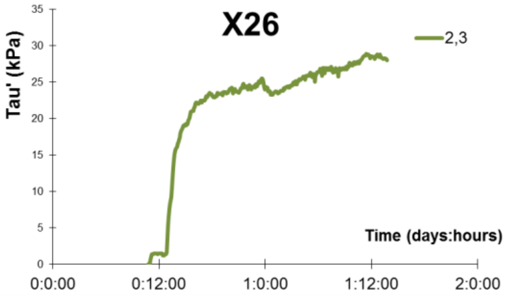

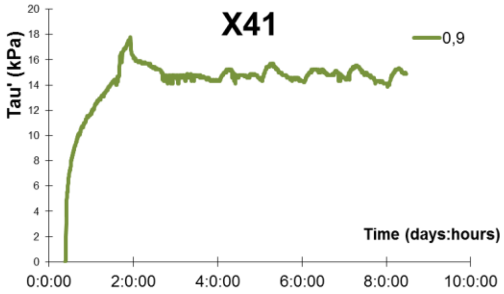

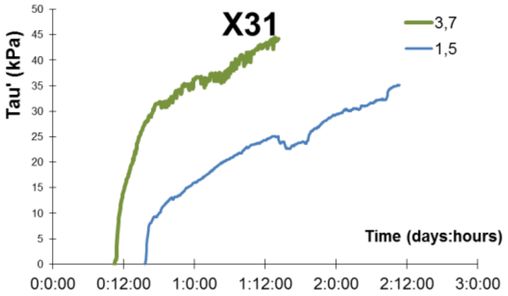

VII. Overview Charonnier Landslide – Hillshade

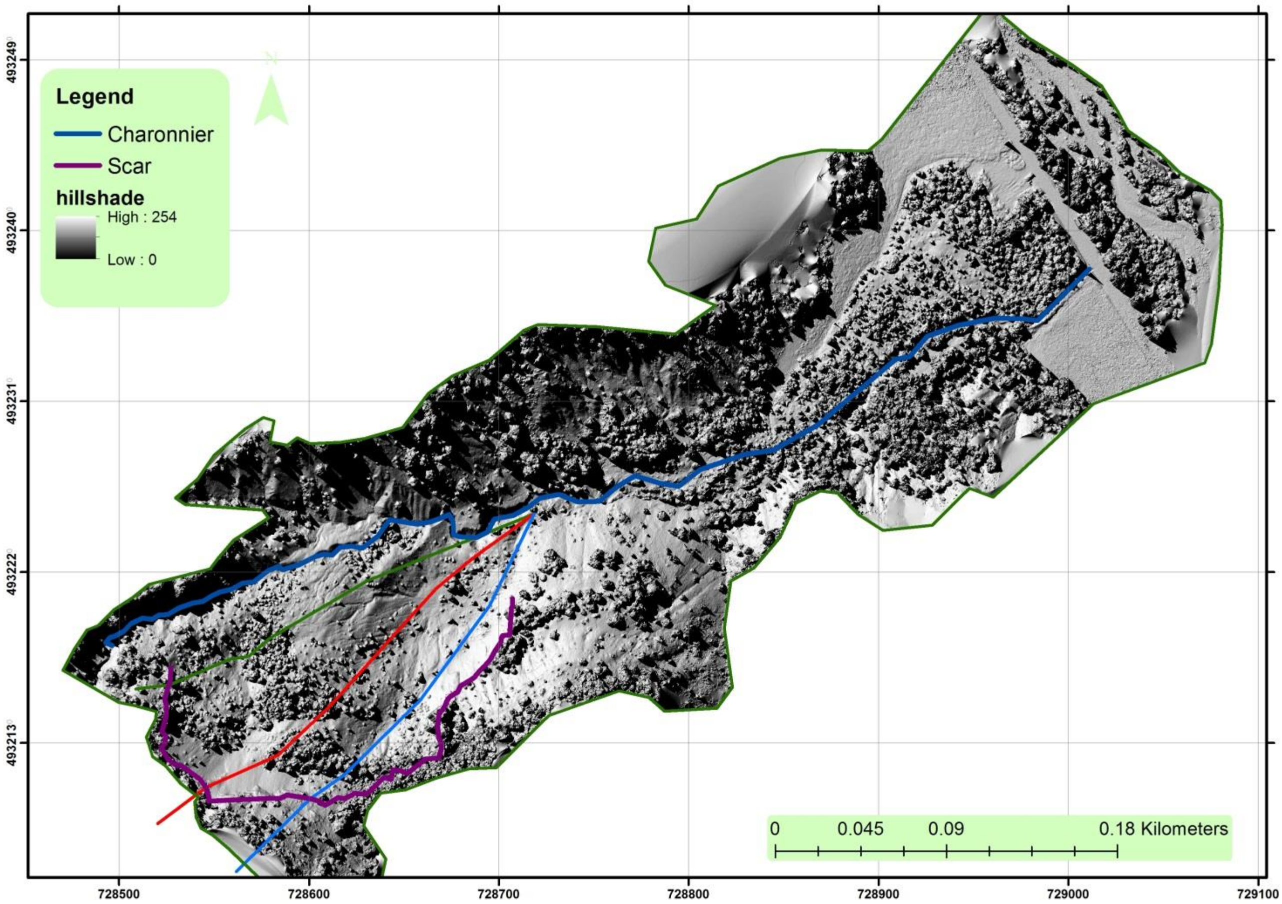

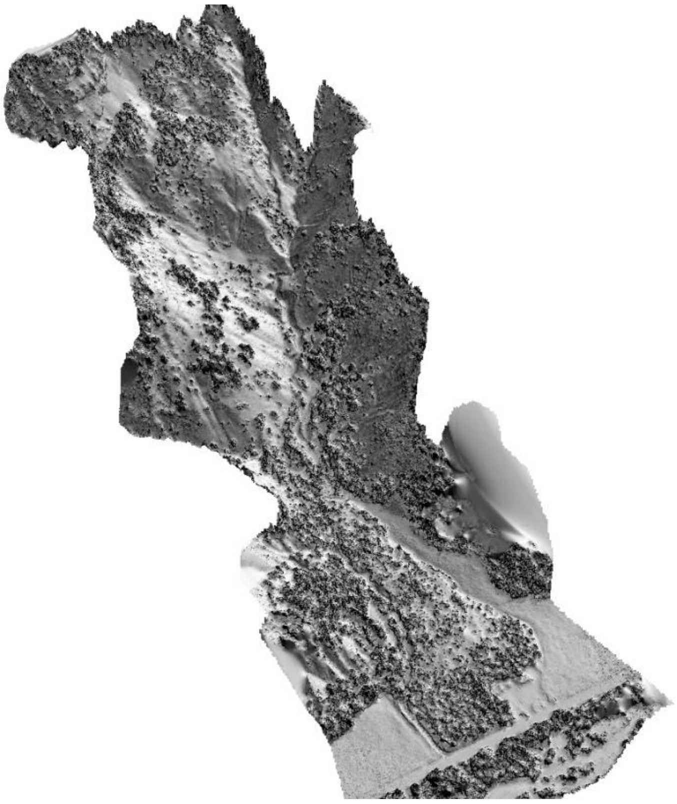

3D overview Charonnier Landslide

Including the source, transport and deposition area.

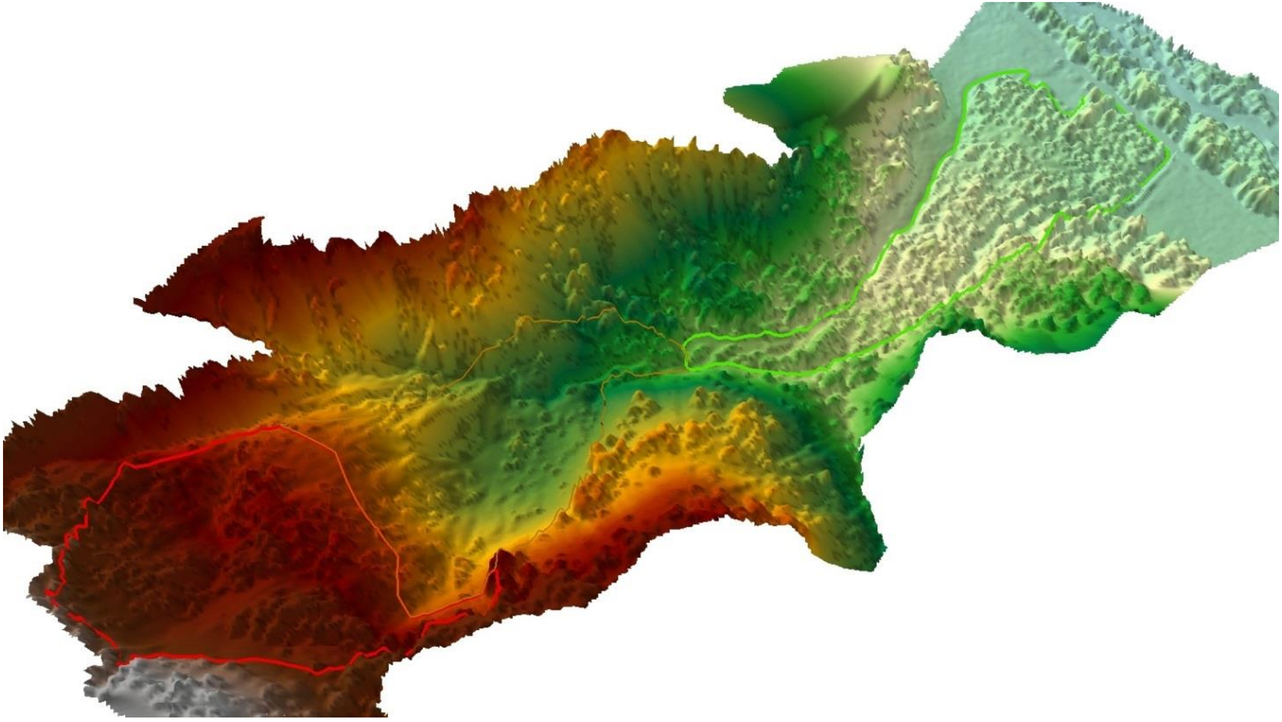

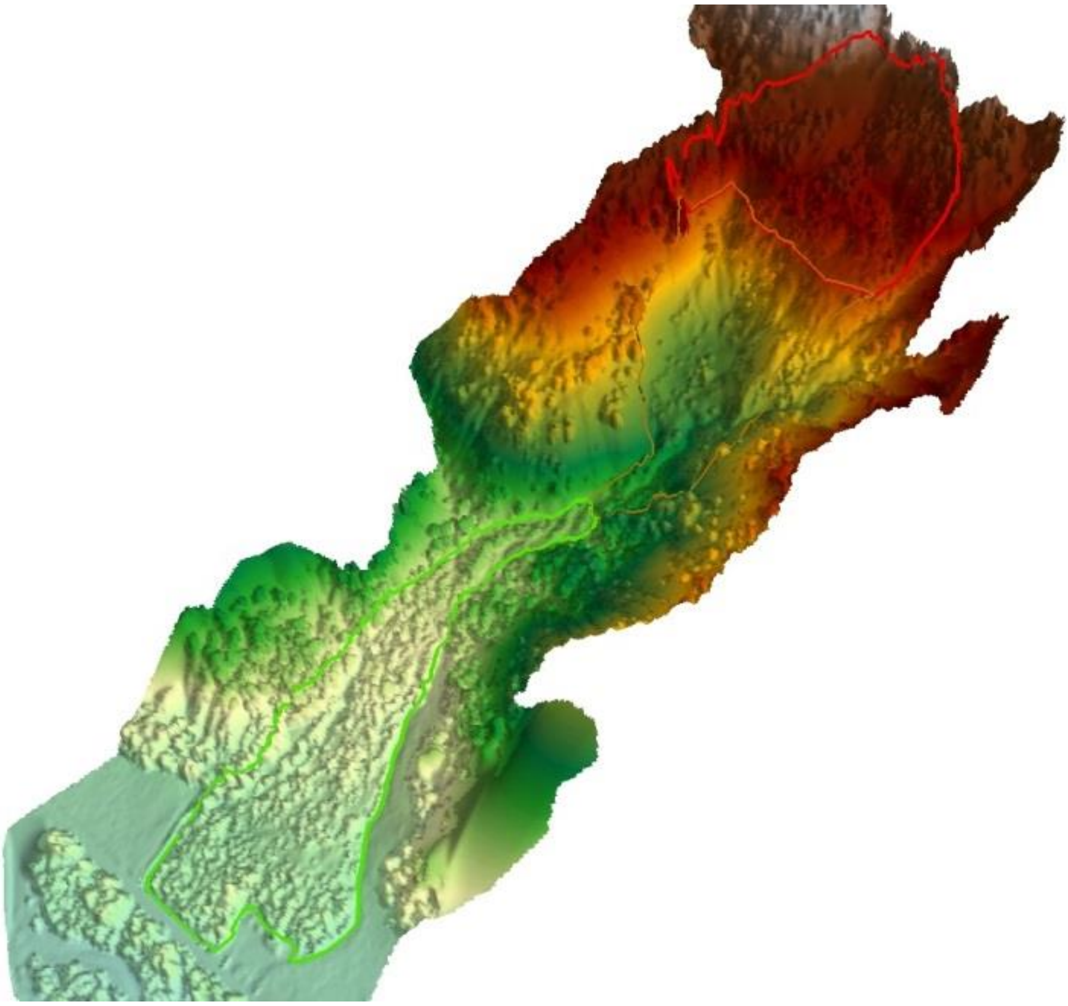

Landslide stability analysis using UAV remote sensing and in situ observations

Job de Vries
Utrecht University